COMPUTATIONAL MODELING OF THROMBUS FORMATION IN ANEURYSMS TREATED WITH SHAPE MEMORY POLYMER FOAM OR BARE METAL COILS

A Dissertation

by

JOHN DAVID HORN

Submitted to the Office of Graduate and Professional Studies of
Texas A&M University
in partial fulfillment of the requirements for the degree of

DOCTOR OF PHILOSOPHY

Chair of Committee,	Duncan J. Maitland
Committee Members,	John C. Criscione
	Roland Kaunas
	Michael Moreno
Head of Department,	Michael McShane

May 2018

Major Subject: Biomedical Engineering

ABSTRACT

To mitigate the risk of intracranial aneurysm rupture, which can lead to severe debilitation or death, embolic devices (e.g., bare metal coils or polymeric open-celled foams) are often delivered via catheter to the aneurysm sac. Hemodynamic perturbations imposed by the device's geometry and biochemical interactions between blood in the aneurysm and the biomaterial surfaces can lead to a clotting response which marks the initial phase of healing. The ideal outcome of this response to treatment is complete aneurysm occlusion and isolation from the parent artery to reduce or eliminate the risk of aneurysm rupture.

To compliment *in vitro* and *in vivo* device testing, which typically reveals limited information related to thrombus formation, a computational model which couples biofluid dynamics and biochemistry has been developed to simulate the transient thrombus formation within treated aneurysms. The model consists of 28 advection-diffusion-reaction partial differential equations to track blood proteins involved in clotting. Boundary flux terms are used to model the initiation of the intrinsic clotting pathway at thrombogenic device surfaces. This "medium-fidelity" approach is applied to an idealized 2D aneurysm geometry and the results are compared to predictions produced by a lower-fidelity model representative of modeling approaches common in the literature for evaluation of device-induced thrombosis. The latter method uses time-averaged flow features to estimate locations of clot formation while disregarding physiological and biochemical phenomena. In contrast, the medium-fidelity model developed in this work is able to represent the biochemical interactions between blood and biomaterial surfaces and produce transient predictions of clot growth within the treated aneurysm.

The medium-fidelity model is applied to compare two different aneurysm treat-

ment methods. First, treatment with embolic bare metal coils is simulated. While coils are the most commonly used devices for aneurysm treatment, their use can often lead to sub-optimal clinical outcomes that can result in aneurysm regrowth. An alternative treatment method, which is also simulated in this work, is the use of porous shape memory foams. These foams are delivered though a catheter and can fully expand to fill the aneurysm sac, providing a scaffold for thrombus growth. The medium-fidelity model is used to predict the clotting response within aneurysms treated with either method. Overall, the results of the coil treatments are highly dependent on the random arrangement of coils within the aneurysm sac and, in many cases, incomplete filling is likely. In contrast, shape memory polymer foams produce a more uniform and predictable result, independent of the foam geometry or orientation.

The computational thrombus model, as presented in this dissertation, should be viewed as an initial iteration of a more complete model. Future work is needed to address several model limitations, and model validation with experimental data is necessary to reduce model uncertainty. Nonetheless, the simulations in this work demonstrate the advantages of the medium-fidelity model approach over low-fidelity models, and they show the model's potential as an engineering tool to aid in device design and improve clinical outcomes.

ACKNOWLEDGMENTS

I would like to acknowledge Dr. Duncan Maitland for the significant impact he has had on my educational and professional development. I am grateful for the opportunity Dr. Maitland gave to me as an undergrad to work in his lab and I am grateful that he wanted me to stay with his lab as a graduate student. As my committee chair, Dr. Maitland always knew when to push me towards opportunities I wouldn't normally pursue and, while he has typically been very patient with me, he always had a knack for lighting fires under me at just the right times. I will always appreciate all the guidance and support he has given me over the last 7 or 8 years. I would like to thank the other members of my committee, Dr. John C. Criscione, Dr. Roland Kaunas, Dr. Michael Moreno for their support and guidance as well.

I would also like to thank Dr. Jason Ortega for serving as an unofficial member of my committee. I have had the opportunity to work closely with Dr. Ortega for the last few years as a Livermore Graduate Scholar at Lawrence Livermore National Lab. I have so much gratitude for Dr. Ortega and I feel like it would take several pages to properly thank him for all that he has done for me. During my time at Lawrence Livermore National Laboratory, he has been an amazing mentor who has given me way more time than I deserve providing technical guidance as well as endless encouragement.

I would also like to thank the many members of the Biomedical Device Laboratory that I have had the pleasure to work with. During my time as an undergrad and my first couple of years as a graduate student, Casey McCurrin, was a great mentor who taught me a lot about fluid flow experiments, including the many ways to make giant messes if you aren't careful with your tubing. Dr. Wonjun Hwang was an amazing source of technical

knowledge and I will always remember his very wise advice: “Rust is the enemy.” Dr. Jennifer Rodriguez was also a great mentor and a friend in my early years as a grad student. Of the students that started around the same time I did, I must thank Dr. Todd Landsman for being an amazing partner in our joint adventures. From designing and manufacturing cases for pig accelerometers to conducting blood flow experiments, I always enjoyed working with you. I also want to express my gratitude to Dr. Tony Boyle who was a great roommate and friend, was always supportive of my research, and who also got a B. Additionally, Dr. Landon Nash and Dr. Mark Wierzbicki were also great colleagues and friends who often provided advice and support throughout my time as a graduate student.

Finally, I would like to thank my parents, David and Joyce, and my sister, Samantha, for their love and support throughout my life and journey towards earning a PhD. I also cannot express enough appreciation and admiration for Dr. Staci Jessen. She has endlessly loved and supported me since we were both undergrads, even while I spent a lot of that time over 2000 miles and 2 time zones away. She has never stopped encouraging me and has always been there to provide any help she could, from proofreading papers and emails to working her photoshop magic to make many of the figures in my papers and in this dissertation. Staci, I hope one day to live up to all the expectations you have of me.

CONTRIBUTORS AND FUNDING SOURCES

Contributors

This work was supported by a dissertation committee consisting of Dr. Duncan Maitland, Dr. John Criscione, and Dr. Roland Kaunas of the Biomedical Engineering Department, Dr. Michael Moreno of the Mechanical Engineering Department, and Dr. Jason Ortega of Lawrence Livermore National Laboratory.

Dr. Ortega provided technical guidance and mentorship throughout this work. The shape memory polymer foam geometries in this work are adapted from digital files provided by Dr. Ortega from μ-CT imaging data of foam samples that he collected and processed for a separate publication (2013). Technical guidance was also provided by our clinical collaborator, Dr. Jonathan Hartman, from the Kaiser Permanente Sacramento Medical Center. All other work conducted for this dissertation was completed by the student independently.

Funding Sources

This work was supported in part by the National Institutes of Health/National Institute of Biomedical Imaging and Bioengineering Grant R01EB000462 and by funding provided by the Livermore Graduate Scholars Program at Lawrence Livermore National Laboratory. This work was performed in part under the auspices of the U.S. Department of Energy by Lawrence Livermore National Laboratory under Contract DE-AC52-07NA27344.

NOMENCLATURE

$\dot{\gamma}$	Fluid Shear Rate
ρ	Fluid Density
μ	Dynamic Viscosity
$\vec{v}$	Velocity
CFD	Computational Fluid Dynamics
GDCs	Guglielmi Detachable Coils
μ-CT	Micro-Computed Tomography
SMP	Shape Memory Polymer

TABLE OF CONTENTS

Page

LIST OF FIGURES

FIGURE Page

LIST OF TABLES

TABLE Page

1. INTRODUCTION AND LITERATURE REVIEW*

1.1 Intracranial Aneurysms

An aneurysm is a localized bulging of a weakened arterial wall. These abnormalities may manifest as saccular structures near artery bifurcations[25,49] and are common in the intracranial vasculature where a lack of an external elastic lamina makes arteries more susceptible to aneurysm formation.[59,118] It is estimated that one in fifty adults in the United States live with one or more unruptured intracranial aneurysms. These aneurysms rupture in approximately 30,000 people per year in the United States[74] resulting in subarachnoid hemorrhage which is severely debilitating or fatal in the majority of cases.[11]

1.2 Bare Metal Coil Aneurysm Treatments

Given the frequently poor outcomes following aneurysm rupture, clinical interventions are carried out to address the risk of rupture. The overall goal of aneurysm treatment is to reduce or eliminate blood flow into the aneurysm sac, thereby reducing pressures and/or shear stresses on the weakened aneurysm wall, and promoting flow stagnation and thrombosis within the aneurysm sac and subsequent healing. In recent decades, the preferred method for achieving this goal has become the endovascular transcatheter placement of bare metal coils to fill and occlude the aneurysm sac. The minimally invasive nature of these procedures is a major advantage over surgical clipping, which requires a full craniotomy to gain access to the affected artery for clip placement, with the associated risk and morbidity of open surgery.

*Select components reprinted with permission from "Comparison of shape memory polymer foam versus bare metal coil treatments in an in vivo porcine sidewall aneurysm model" by John Horn, Wonjun Hwang, Staci L. Jessen, Brandis K. Keller, Matthew W. Miller, Egemen Tuzun, Jonathan Hartman, Fred J. Clubb, Jr., Duncan Maitland, *Journal of Biomedical Materials Research B: Applied Biomaterials*. Copyright (2016) Wiley Periodicals, Inc.

The earliest developed and most extensively studied bare metal coils used clinically are Guglielmi Detachable Coils (GDCs).[43] These soft platinum alloy coils are pushed through a catheter that has been guided from a vascular access point, such as the femoral artery, through the vasculature to the aneurysm location. Once the catheter is placed, a coil is pushed out of the catheter into the aneurysm sac and an electrical current is applied to dissolve, via electrolysis, a link connecting the coil to the pusher, thereby releasing it into the aneurysm. The number of coils placed inside the aneurysm is dependent on the aneurysm diameter (approximately one coil per millimeter of aneurysm diameter[126]), and varies based upon the length and diameter of the coils, as well as operator preference. After placement, the coils reduce the amount of flow entering the aneurysm sac and stimulate thrombus production. Ideally, a stable clot is formed inside the aneurysm around the coils which, via the body's healing processes, is converted to a collagen-based, scar-like structure permanently occluding the aneurysm and isolating it from the flow of the parent artery. Further, it is optimal for re-endothelialization to occur across the neck, or ostium, of the aneurysm completely excluding it from the parent artery flow and returning a normal patent shape to the lumen of the artery.

Coiling treatments quickly gained favor over clipping, accounting for approximately half of all first-choice treatment options by the year 2000,[94] largely in part because of the minimally invasive nature, quick procedural time, and lower cost; however, this technique is not without its limitations. The bioinert nature of bare metal coils elicits limited tissue response which can lead to unorganized thrombus formation and poor aneurysm healing.[79,120] Szikora et al. reported a number of coil-treated aneurysms that failed to form neointimal layers across their necks at time points as late as three years post-treatment.[120] Further, low volume occlusions in coil-treated aneurysms can result in coil compaction over time, due to a water hammering effect from the pulsing arterial flow,[60] resulting in recanalization rates of 21-34%.[37,96,111,112,128] These aneurysms are susceptible to aneurysm

growth, rupture or rerupture, and the growth of adjacent daughter aneurysms. In 10.3% of coil-treated aneurysms, recanalization necessitates retreatment.[30] Other issues include possible coil migration from the aneurysm sac into the parent artery,[8,91,129] and a risk of intraprocedural aneurysmal rupture,[28] which can have devastating consequences. Given this potential for procedural complication and suboptimal long-term healing, it is desirable to develop new technologies to enhance aneurysm treatment outcomes.

1.3 Shape Memory Polymer Foam Aneurysm Treatments

As an alternative to bare metal coil treatments, the use of shape memory polymer (SMP) foams as embolic fillers has been proposed.[44,68,73] SMP foams are porous polymeric materials that are capable of actuating from a set shape to a second "memorized" shape upon an increase in bulk temperature. This allows for the foam to be compressed to a size compatible with catheter delivery and then actively actuated within an aneurysm, achieving up to a 70-fold volume expansion[110] to fill the entire intra-aneurysmal space without imposing significant stress on the aneurysm wall.[50] In addition to large volume expansions, the porous architectures of ultralow-density SMP foams provide large blood-contacting surface areas (up to 1000 cm^2 per 1 cm^3 of bulk foam[46]) and restrict blood flow to highly tortuous pathways that greatly reduce flow magnitude within an aneurysm.[86,113] Furthermore, SMP foams have exhibited good biocompatibility *in vivo*.[17,73,102,110]

Evidence of polyurethane-based SMP foam's biocompatibility and efficacy as an aneurysm treatment was reported by Rodriguez et al.[100] The authors surgically implanted SMP foam samples within constructed *in vivo* porcine vein pouch aneurysm models following the technique described by Guglielmi et al.[42] Histology after 30 and 90 days post-implantation revealed progressive healing within the foam filled aneurysms marked by the presence of predominately loose to dense connective tissue within the aneurysm. After 90 days, complete formation of neointimal layers were observed across each aneurysm

neck excluding the aneurysms from arterial flow. Additionally, the foam elicited a reduced inflammatory response when compared to the FDA-approved sutures used to construct the aneurysm model, suggesting that the SMP foam is at least as biocompatible as clinically used biomaterials. A later longer-term *in vivo* study examined similar porcine aneurysm models treated with SMP foam devices.[48] In that study, foam was delivered to the aneurysm via catheter and actuated using a resistive heater core. Histologic analysis was performed on the aneurysms explanted after 90 and 180 days post-treatment. The results of the study further demonstrated the foam's biocompatibility, and at 90 days post-treatment, the histologic observations were similar to the previous study by Rodriguez et al. Additionally, the healing response elicited by the SMP foam were shown to be at an advanced stage of healing at 180 days wherein the central cores of the aneurysms were predominantly filled with mature connective tissue. Further, the presence of hemosiderin-laden macrophages throughout the aneurysm at 90 days and their presence only in the outer edges of the aneurysm by 180 days indicated that the macrophages had nearly completed the process of clearing cellular and clot debris. Aneurysms treated with bare metal coils were also evaluated at the same time points. While these aneurysms showed evidence of a slower healing response than the foam-treated aneurysms, the sample sizes did not provide sufficient statistical power to make definitive comparisons between the two treatment methods.

1.4 Clotting Response to Embolic Aneurysm Fillers

A large body of literature exists describing studies, like the ones mentioned above, that evaluate the long-term outcomes of various aneurysm treatments. These studies mostly present data on gross or histologic indictors of healing and typically do not capture the initial response that occurs within the first ten to fifteen minutes following treatment. This response involves biochemical and hemodynamic interactions between the blood and

the implanted device that stimulate clot formation, which leads to partial or complete aneurysm occlusion. This response is of interest as thrombus occlusion could correlate to long-term treatment outcomes. For example, aneurysms treated with bare metal coils that exhibit incomplete thrombus occlusion, particularly in the aneurysm neck, have been shown to be susceptible to adverse outcomes (e.g., aneurysm recanalization, growth, and rupture) that often require retreatment.[55,120] Conversely, it is possible that, through device design, the clotting response can be optimized (e.g., to improve clotting speed or to achieve favorable thrombus growth patterns within the aneurysm) to promote improved clinical outcomes.

Clot formation is a complex process involving the aggregation of activated platelets and a concomitant series of biochemical reactions that takes place among the many proteins in the blood.[2,40,59] During homeostasis, negative feedback loops prevent the system of reactions from driving towards thrombosis. However, when the system is perturbed by vessel injury, non-ideal hemodynamics, or blood contact with negatively charged surfaces, a cascade of reactions is initiated – through either the extrinsic or intrinsic pathway – that ends in the conversion of fibrinogen in the blood to fibrin monomers. These monomers later polymerize and form a cross-linked matrix that enmeshes platelets and other cellular matter in the blood, thus forming a blood clot.

Early in the clot formation process, platelet activation can be induced by collagen on injured endothelial cells or by prolonged exposure to abnormally high shear.[6,104] Later, chemical agonists such as thrombin (product of clotting cascade) and ADP (released by activated platelets) further accelerate platelet activation. Activating platelets undergo a morphological change that promotes aggregation and results in the expression of phospholipid binding sites – critical for the progression of the clotting cascade – on their membranes. Activated platelets also release factor XIII, which crosslinks the strands of the fibrin mesh, thereby mechanically stabilizing the clot.

The extrinsic pathway of the biochemical clotting cascade is initiated upon vessel injury, when membrane-bound tissue factor (TF) on the endothelium becomes exposed to blood and binds with factor VIIa (VIIa). The resulting TF-VIIa complex catalyzes the activation of factors IX and X to factors IXa and Xa, respectively. The clotting cascade can also be initiated, via the intrinsic pathway, as a response to blood contact with negatively charged surfaces, such as collagen, glass, or biomaterial surfaces. At the thrombogenic surface, factor XII is activated and XIIa activates prekallikrein to kallikrein, which in turn activates more XII, thereby accelerating intrinsic pathway initiation. The clotting cascade continues as XIIa activates factor XI to XIa, which in turn activates factor IX. Thrombin-activated factor VIII (VIIIa) assembles with IXa at phospholipid binding sites on platelet membranes to form the tenase complex, which activates factor X.

The extrinsic and intrinsic pathways converge at the production of Xa, and the remaining portion of the clotting cascade is referred to as the common pathway.[59] At this stage, Xa complexes with thrombin-activated factor V (Va) to form the prothrombinase complex at phospholipid binding sites on activated platelet membranes. Prothrombinase then catalyzes the activation of prothrombin (II) to thrombin (IIa), which in turn catalyzes the conversion of fibrinogen (I) to fibrin monomers (Ia) resulting in the formation of thrombus.

Throughout the clotting cascade, positive and negative feedback loops act to either amplify or inhibit the progression of clot formation. Thrombin has an amplifying effect on the clotting cascade as it activates V and VIII and is the predominate activator for XI. Some proteins inhibit certain enzymes in the clotting cascade to regulate clotting and prevent clot formation distant from the thrombogenic stimulus. Antithrombin-III (ATIII) neutralizes XIIa, XIa, Xa, IXa, and thrombin. This effect is amplified in the presence of heparin or heparin-like molecules located on the endothelium.[92,115,130] Tissue factor pathway inhibitor (TFPI) inhibits Xa and the TF-VIIa complex, thrombin-activated protein

C (APC) inhibits the production of Va and VIIIa, and C1-Inhibitor competitively binds with XIIa and XIa.

The fibrinolytic pathway is initiated alongside the clotting cascade to regulate clot size and extent. In this pathway, plasmin (PLA) degrades fibrin monomers and prevents fibrin polymerization. PLA is produced by the activation of circulating plasminogen (PLS) by either XIIa or fibrin-bound tissue plasminogen activator (tPA), which is produced by endothelial cells stimulated by fibrin or thrombin. The fibrinolytic pathway is regulated by α_2-anitplasmin (α_2AP) which inhibits PLA.

1.5 Computational Modeling of Clot Formation

The study of device-induced thrombosis through experimental means is challenging. *In vitro* studies of blood clotting cannot completely and accurately represent the physiological environment within the vasculature and are difficult to apply to large scale geometries such as treated aneurysms. Depending on the animal model chosen, *in vivo* studies can be more physiologically representative; however, monitoring clot growth with sufficient temporal and spatial resolution is not possible given current techniques for non-destructive imaging of the vasculature. Even the method used clinically to determine sufficient aneurysm occlusion (i.e., contrast-based angiography) only yields 2D projections of the intra-aneurysmal space. Also, the implanted material is often more radio-opaque than the contrast dye and can obscure the presence or absence thrombus. Computational modeling can be an alternative to experimental studies to obtain spatially and time-resolved estimates of thrombus development within aneurysms treated with embolic materials. Therefore, a computational thrombus formation model can be used as an engineering tool to inform device design to improve short-term and possibly long-term treatment outcomes, all while reducing the need for costly and time-consuming long-term *in vivo* studies.

Much of the computational work to date to model clotting in relation to biomed-

ical devices has ignored the biochemical processes involved, opting instead to employ "low-fidelity" models that correlate hemodynamic features to likely locations of clot formation. Experimental work has shown that small time-averaged shear rates and prolonged fluid residence times are indicators of potential clot formation,[12,21,33,97] and many computational studies have used one or both criteria to predict clotting.[45,80,86,87] While these models tend to show good agreement with experimental results, they typically only give indications of the initial thrombus location, cannot resolve transient clot growth, and do not couple the flow field to the thrombus distribution to reflect how thrombus growth alters flow patterns. Further, these models neglect all physiological phenomena that influence thrombosis.

Several models have attempted to represent the biochemical processes governing clot formation and growth. A major feature of these "medium-fidelity" models is the use of advection-diffusion-reaction differential equations to track the mass transport and reactive generation or depletion of a select number of biochemicals to capture the series of enzymatic reactions involved in the coagulation cascade.[2,3,5,15,58,65,82,89,135] Other models, such as the recent work of Wu et al., use this medium-fidelity approach to track resting and activated platelets and their deposition along injured tissue or biomaterial surfaces.[132] Review articles by Anand et al.[2] and Cito et al.[20] detail many of the medium-fidelity models available in the literature. While these models are more physiologically relevant than the low-fidelity correlative methods, few have been extended to predict the response to blood-contacting devices, with those that have limited to non-complex geometries and neglecting the biochemical interactions between blood (i.e. factor XII) and the biomaterial surface.

The objective of this work is to use computational modeling to evaluate the short-term clotting performance of embolic devices used to treat intracranial aneurysms. Knowledge of the clotting response within treated aneurysms could be valuable in understanding

the long-term performance of the treatment methods. Such information could be used to optimize device design to induce favorable clotting behaviors. Low-fidelity models do not elucidate transient clotting behavior and ignore most of the physiological phenomena that are responsible for the clotting response. Therefore, while commonly used to study device-induced clotting, those models are insufficient for this work. Instead, medium-fidelity models are more physiologically relevant and can be used to track the progression of clot growth over time. However, current embodiments of such models are typically designed for injury-related thrombosis and not device-related thrombosis as they do not capture the interactions between blood and biomaterial surfaces. Thus, a medium-fidelity model with novel features is developed in this work to enable the study of the clotting response to aneurysm treatments (Chapter 2). This model is demonstrated and compared to a low-fidelity model via simulations of an SMP foam-treated aneurysm (Chapter 3). In the interest of device optimization, the medium-fidelity model is used to study the impact of SMP foam parameters on clotting performance in an idealized aneurysm geometry and the overall performance of the foams is compared to that of the bare metal coils which represent the most commonly used clinical treatment (Chapter 4). This dissertation is concluded with a discussion of the limitations associated with the computational thrombus formation model and the simulations presented herein, and suggestions for future model development and future modeling efforts are offered (Chapter 5).

2. A MEDIUM-FIDELITY COMPUTATIONAL THROMBUS FORMATION MODEL

The clinical success of many cardiovascular implantable devices is impacted by blood's clotting response. Many devices (e.g. stents,[23] heart valves,[18] and ventricular assist devices[117]) are negatively affected by thrombosis. Other devices, such as foam-based[16,48,100] or coil-based[43,124] aneurysm treatments, peripheral embolization devices,[62] and treatments for certain congenital heart defects,[131] are designed to elicit a controlled thrombotic response. While computational fluid dynamics (CFD) studies are often used to evaluate device-related hemodynamics, few have modeled device-induced thrombosis. Such clot growth simulations could serve as an engineering tool during the device design process and thereby reduce the need for costly and time consuming *in vivo* testing.

The overall goal of this work is to use computational modeling to study the clotting response to aneurysm treatments. Most modeling approaches used to evaluate device-related thrombosis ignore physiological and biochemical phenomena. Furthermore, transient clot growth is typically not resolved, nor are the alterations in the flow field imposed by the changing clot geometry. To produce a more physiologically-relevant representation of post-treatment clotting in aneurysms, a medium-fidelity thrombus formation model has been developed by adapting the work of LaCroix and Anand.[61] The model, which is described in this chapter, couples biochemical phenomena (e.g., clotting cascades) and biofluid phenomena (i.e., blood flow), and incorporates a mechanism for directly modeling the interactions between blood and biomaterial surfaces.

2.1 Modeling Blood Flow

Blood is assumed to be a continuum and is treated as a homogenous shear-thinning fluid with a density, ρ, of 1060 kg/m^3. The non-Newtonian behavior of blood is described

as a function of local shear rate magnitude ($\dot{\gamma}$) using a generalized power law model:[7]

$$\mu(\dot{\gamma}) = \lambda|\dot{\gamma}|^{n-1} \tag{2.1}$$

where the power law consistency (λ) and index (n) are also functions of local shear rate:

$$\lambda(\dot{\gamma}) = \mu_\infty + \Delta\mu \exp\left[-\left(1+\frac{|\dot{\gamma}|}{a}\right)\exp\left(-\frac{b}{|\dot{\gamma}|}\right)\right] \tag{2.2}$$

$$n(\dot{\gamma}) = n_\infty + \Delta n \exp\left[-\left(1+\frac{|\dot{\gamma}|}{c}\right)\exp\left(-\frac{d}{|\dot{\gamma}|}\right)\right] \tag{2.3}$$

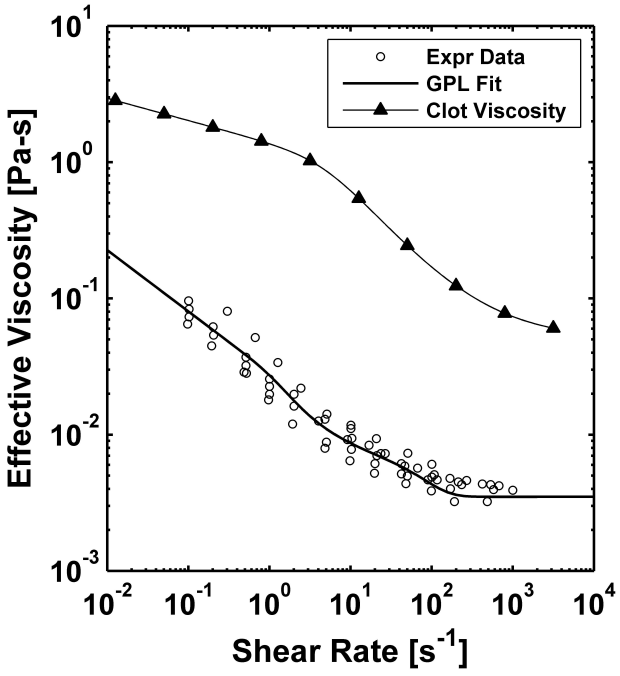

Figure 2.1: Non-Newtonian models for the shear-dependent viscosity of blood and blood clots. The generalized power law (GPL) fit is used for blood viscosity and is fit to experimental data presented by Ballyk et al. who measured viscosity as a function of shear rate for human blood.[7] Clot viscosity is calculated using an Oldroyd-B type model (see section 2.3).

In equations 2.2 and 2.3, $\Delta\mu$, Δn, a, b, c, and d are parameters that Ballyk et al.[7] obtained by fitting several experimental data sets of human blood viscosity as a function of shear rate. Their resulting values are 0.025 Pa-s, 0.45, 50, 3, 50, and 4, respectively. Values of 0.0035 Pa-s and 1.0 were chosen for μ_∞ and n_∞, respectively, to approximate blood as a Newtonian fluid at high shear rates. The viscosity model is plotted in Figure 2.1 along with the corresponding experimental data. The flow field for blood is predicted by solving the equations for mass and momentum balance,

$$\frac{\partial \rho}{\partial t} + \rho\,(\nabla \cdot \vec{v}) = 0 \tag{2.4}$$

$$\rho \frac{\partial \vec{v}}{\partial t} + \nabla \cdot (\rho \vec{v}\vec{v}) = -\nabla p + \nabla \cdot (2\mu(\dot{\gamma})D) \tag{2.5}$$

for an incompressible fluid using a commercially available finite volume CFD package (STAR-CCM+ v. 9.04.009, CD-Adapco), where $\vec{v}$ is the velocity vector, p is the pressure, $\mu(\dot{\gamma})$ is the viscosity as a function of the shear rate, $\dot{\gamma}$, and $D = \frac{1}{2}\left[\nabla\vec{v} + (\nabla\vec{v})^T\right]$ is the symmetric part of the velocity gradient tensor. The balance equations are solved using a SIMPLE-type algorithm with Rhie-and-Chow-type pressure-velocity coupling and a collocated grid variable arrangement. A second-order upwind scheme is used to determine convective fluxes and time is discretized using a second-order implicit scheme.[26,71]

2.2 Modeling Biochemistry of Clot Formation

A model developed by Anand et al.[2,5] and described by LaCroix and Anand[61] is adapted here to simulate the biochemical processes leading to clot formation, and a novel set of boundary conditions is added to model the interactions between blood and biomaterial surfaces, as well as the regulatory function of heparin-like molecules lining

healthy tissue. The model consists of a set of advection-diffusion-reaction equations,

$$\frac{\partial [Y_i]}{\partial t} + div\left([Y_i]\,\vec{v}\right) = div\left(D_i \nabla [Y_i]\right) + R_i \tag{2.6}$$

governing the concentrations ($[Y_i]$), mass transport by advection and diffusion, and the generation or depletion via biochemical reaction of several blood proteins involved in thrombus formation and regulation. It is assumed that the concentrations of the blood constituents considered here are small enough to be treated as passive quantities that do not impact local fluid properties such as density or viscosity. However, a fibrin concentration threshold is used to identify computational elements filled with clotted blood, which are given an elevated viscosity (see section 2.3).

The computational model developed in this work adopts the set of proteins modeled by LaCroix and Anand,[61] which includes 28 clotting factors and regulatory proteins involved in the clotting process. These include: inactive zymogens fibrinogen (I), prothrombin (II), V, VIII, IX, X, XI, XII, and prekallikrein (prek); their respective activated enzymatic forms fibrin (Ia), thrombin (IIa), Va, VIIIa, IXa, Xa, XIa, XIIa, and kallikrein (kalli); and regulatory proteins plasminogen (PLS) and its active form plasmin (PLA), protein C (PC) and activated protein C (APC), antithrombin III (ATIII), tissue factor pathway inhibitor (TFPI), tissue plasminogen activator (tPA), C1-Inhibitor (C1INH), α_1-antitrypsin (α_1AT), and α_2-antiplasmin (α_2AP). Additionally, the concentrations of two membrane bound complexes are computed directly from the local concentrations of their component proteins: tenase (IXa-VIIIa, denoted "Z") and prothrombinase (Xa-Va, denoted "W"). Diffusion coefficients (D_i) for each protein (Table 2.1) are determined using the procedure described by Anand et al.[2] While many more proteins exist in the blood that contribute to clot formation and regulation, the selected proteins are assumed to be the most significant.

Species	Diffusion Coefficients (m^2/s)	Initial/Inlet Concentrations (nM)
I	$D_I = 3.10$ x 10^{-11}	7000
Ia	$D_{Ia} = 2.47$ x 10^{-11}	0
II	$D_{II} = 5.21$ x 10^{-11}	1400
IIa	$D_{IIa} = 6.47$ x 10^{-11}	0
V	$D_V = 3.12$ x 10^{-11}	20
Va	$D_{Va} = 3.82$ x 10^{-11}	0
VIII	$D_{VIII} = 3.12$ x 10^{-11}	0.7
VIIIa	$D_{VIIIa} = 3.92$ x 10^{-11}	0
IX	$D_{IX} = 5.63$ x 10^{-11}	90
IXa	$D_{IXa} = 6.25$ x 10^{-11}	0
X	$D_X = 5.63$ x 10^{-11}	170
Xa	$D_{Xa} = 7.37$ x 10^{-11}	0
XI	$D_{XI} = 3.97$ x 10^{-11}	30
XIa	$D_{XIa} = 5.00$ x 10^{-11}	0
XII	$D_{XII} = 5.00$ x 10^{-11}	500
XIIa	$D_{XIIa} = 2.93$ x 10^{-11}	0.5
prek	$D_{prek} = 4.92$ x 10^{-11}	485
kalli	$D_{kalli} = 4.92$ x 10^{-11}	0
PLS	$D_{PLS} = 4.81$ x 10^{-11}	2180
PLA	$D_{PLA} = 4.93$ x 10^{-11}	0
PC	$D_{PC} = 5.44$ x 10^{-11}	60
APC	$D_{APC} = 5.50$ x 10^{-11}	0
C1INH	$D_{C1INH} = 4.61$ x 10^{-11}	1625
ATIII	$D_{ATIII} = 5.57$ x 10^{-11}	2410
TFPI	$D_{TFPI} = 6.30$ x 10^{-11}	2.5
α_1AT	$D_{\alpha_1 AT} = 5.82$ x 10^{-11}	45000
α_2AP	$D_{\alpha_2 AP} = 5.25$ x 10^{-11}	105
tPA	$D_{tPA} = 5.28$ x 10^{-11}	0.08

Table 2.1: Diffusion coefficients and initial and inlet concentrations for each biochemical constituent included in the model. Initial/inlet concentration for XIIa set to 0.1% of the initial concentration of XII. All other non-zero concentrations are taken from LaCroix and Anand.[61]

A schematic describing the modeled reactions is shown in Figure 2.2 and the reactions and rate constants involved in zymogen activation and enzyme inactivation are listed in Table 2.2 and Table 2.3. The reaction kinetics and rate constant values – taken from experiments using human blood and plasma proteins – describing each reaction are listed in Table 2.4. The net change in concentration for a protein due to those reactions is incorporated via a reactive source term (R_i in equation 2.6). These terms are listed for each modeled protein in equations 2.7-2.36 where $R_{Y_i} = \dfrac{\partial [Y_i]}{\partial t}$. Descriptions of the reactive source terms and the implied assumptions have been detailed by Anand et al. and LaCroix and Anand.[5,61] To model the specific response of blood to blood-contacting devices, the present model deviates from those prior model formulations in the treatment of surface-

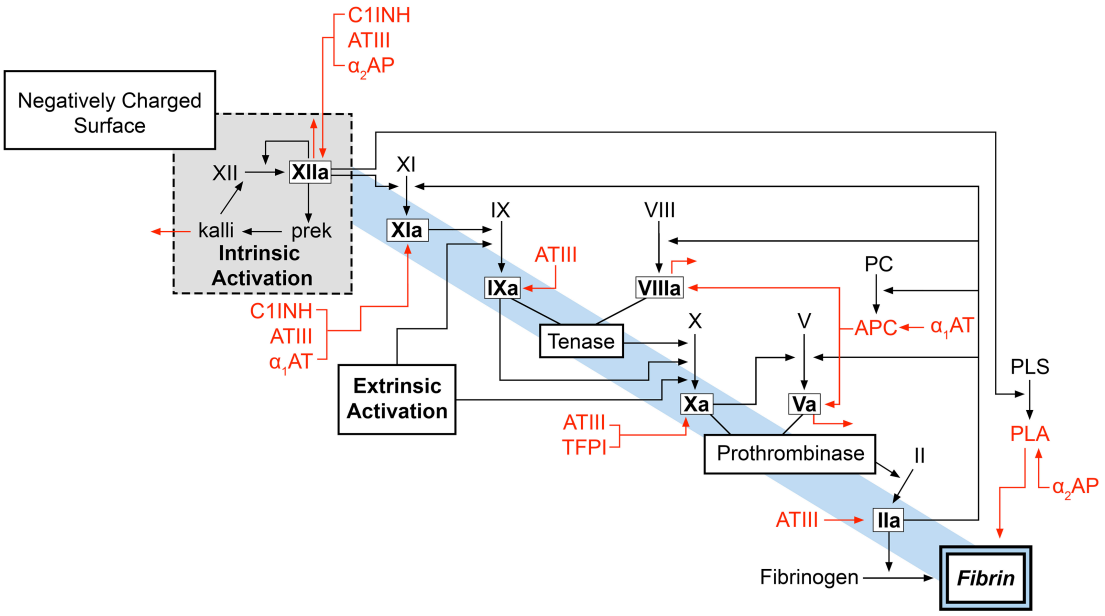

Figure 2.2: Schematic of reactions included in the biochemical clotting model. Black arrows indicate zymogen activation. Enzyme inhibition is denoted by red arrows and inhibitors are listed in red for each enzyme. Red arrows from kalli, XIIa, VIIIa, and Va indicate spontaneous enzyme degradation.

dependent factor XII activation. Tankersley et al.,[122] and others,[38,136] have shown that XII activation is accelerated at negatively charged surfaces such as those of biomedical devices. While LaCroix and Anand effectively assumed all factor XII activation in the domain is enhanced by the presence of negatively charged surfaces (by using rate constants measured in the presence of dextran sulfate[122]), the present model differentiates between surface-accelerated activation – applied via boundary flux terms along device surfaces –

Zymogen	Rate Constants	Reaction
XII	k_{12}, K_{12M}	$XII \xrightarrow{XIIa} XIIa$
	k_{kalli}, K_{kalliM}	$XII \xrightarrow{kalli} XIIa$
prek	k_{prekA}, K_{prekAM}	$prek \xrightarrow{XIIa} kalli$
	k_{prekB}, K_{prekBM}	$prek \xrightarrow{XIIa} kalli$
XI	k_{11}, K_{11M}	$XI \xrightarrow{IIa} XIa$
	k_{12a}, K_{12aM}	$XI \xrightarrow{XIIa} XIa$
IX	k_9, K_{9M}	$IX \xrightarrow{XIa} IXa$
Z	K_{dZ}	$VIIIa + IXa \overset{PL\text{-}}{\rightleftharpoons} Z$
X	k_{10}, K_{10M}	$X \xrightarrow{Z} Xa$
	k_{9a10}, K_{9a10M}	$X \xrightarrow{IXa} Xa$
W	K_{dW}	$Va + Xa \overset{PL\text{-}}{\rightleftharpoons} W$
II	k_2, K_{2M}	$II \xrightarrow{W} IIa$
I	k_1, K_{1M}	$I \xrightarrow{IIa} Ia$
VIII	k_8, K_{8M}	$VIII \xrightarrow{IIa} VIIIa$
V	k_5, K_{5M}	$V \xrightarrow{IIa} Va$
	k_{xa5}, K_{xa5M}	$V \xrightarrow{Xa} Va$
PLS	$k_{PLA\text{-}12a}, K_{PLA\text{-}12aM}$	$PLS \xrightarrow{XIIa} PLA$
	k_{PLA}, K_{PLAM}	$PLS \xrightarrow{tPA\text{-}Ia} PLA$
PC	k_{PC}, K_{PCM}	$PC \xrightarrow{IIa} APC$

Table 2.2: Biochemical reactions (zymogen activation). "W" and "Z" refer to the prothrombinase and tenase complexes, and "PL-" denotes phospholipid binding sites on platelet membranes.

Enzyme	Rate Constants	Reaction
XIIa	h_{12}	$XIIa \rightarrow XII_i$
	h_{12}^{C1}	$XIIa + C1INH \rightarrow XIIa\text{-}C1INH$
	h_{12}^{A3}	$XIIa + ATIII \rightarrow XIIa\text{-}ATIII$
	h_{12}^{L2}	$XIIa + \alpha_2AP \rightarrow XIIa\text{-}\alpha_2AP$
kalli	h_{kalli}	$kalli \rightarrow kalli_i$
XIa	h_{11}^{C1}	$XIa + C1INH \rightarrow XIa\text{-}C1INH$
	h_{11}^{A3}	$XIa + ATIII \rightarrow XIa\text{-}ATIII$
	h_{11}^{L1}	$XIa + \alpha_1AT \rightarrow XIa\text{-}\alpha_1AT$
IXa	h_9	$IXa + ATIII \rightarrow IXa\text{-}ATIII$
Xa	h_{10}	$Xa + ATIII \rightarrow Xa\text{-}ATIII$
	h_{TFPI}	$Xa + TFPI \rightarrow Xa\text{-}TFPI$
IIa	h_2	$IIa + PLA \rightarrow I_i$
VIIIa	h_8	$VIIIa \rightarrow VIIIa_i$
	h_{C8}, H_{C8M}	$VIIIa \xrightarrow{APC} VIIIa_i$
Va	h_5	$Va \rightarrow Va_i$
	h_{C5}, H_{C5M}	$Va \xrightarrow{APC} Va_i$
PLA	h_{PLA}	$PLA + \alpha_2AP \rightarrow PLA\text{-}\alpha_2AP$
APC	h_{PC}	$APC + \alpha_1AT \rightarrow APC\text{-}\alpha_1AT$

Table 2.3: Biochemical reactions (enzyme inactivation).

and slower activation in the domain away from device surfaces where rate constants measured in the absence of negatively charged surfaces are applied.

$$\begin{aligned} R_{XIIa} =& \frac{k_{12}[XII][XIIa]}{K_{12M} + [XII]} + \frac{k_{kalli}[kalli][XII]}{K_{kalliM} + [XII]} \\ & - [XIIa]\left(h_{12} + h_{12}^{C1}[C1INH] + h_{12}^{A3}[ATIII] + h_{12}^{L2}[\alpha_2AP]\right) \end{aligned} \tag{2.7}$$

$$R_{XII} = -\frac{k_{12}[XII][XIIa]}{K_{12M} + [XII]} - \frac{k_{kalli}[kalli][XII]}{K_{kalliM} + [XII]} \tag{2.8}$$

$$R_{kalli} = \frac{k_{prekA}[XIIa][prek]}{K_{prekAM} + [prek]} + \frac{k_{prekB}[XIIa][prek]}{K_{prekBM} + [prek]} - h_{kalli}[kalli] \tag{2.9}$$

$$R_{prek} = -\frac{k_{prekA}[XIIa][prek]}{K_{prekAM} + [prek]} - \frac{k_{prekB}[XIIa][prek]}{K_{prekBM} + [prek]} \tag{2.10}$$

Species	Kinetics	Rate Constants	Source
XII	M	$k_{12} = 3.3$ x 10^{-4} s^{-1}, $K_{12M} = 7500$ nM	[122]
	M	$k_{kalli} = 0.01$ s^{-1}, $K_{kalliM} = 11000$ nM	[122]
prek	M	$k_{prekA} = 3.6$ s^{-1}, $K_{prekAM} = 91$ nM	[122]
	M	$k_{prekB} = 40$ s^{-1}, $K_{prekBM} = 37000$ nM	[122]
XI	M	$k_{11} = 1.3$ x 10^{-4} s^{-1}, $K_{11M} = 50$ nM	[35]
	M	$k_{12a} = 5.667$ x 10^{-4} s^{-1}, $K_{12aM} = 2000$ nM	[35]
IX	M	$k_9 = 0.1833$ s^{-1}, $K_{9M} = 160$ nM	[119]
Z	S	$K_{dZ} = 0.56$ nM	[1]
X	M	$k_{10} = 39.85$ s^{-1}, $K_{10M} = 160$ nM	[95]
	M	$k_{9a10} = 1.533$ x 10^{-3} s^{-1}, $K_{9a10M} = 45000$ nM	[95]
W	S	$K_{dW} = 0.1$ nM	[70]
II	M	$k_2 = 22.4$ s^{-1}, $K_{2M} = 1060$ nM	[57]
I	M	$k_1 = 59$ s^{-1}, $K_{1M} = 3160$ nM	[123]
VIII	M	$k_8 = 3.24$ s^{-1}, $K_{8M} = 112000$ nM	[24]
V	M	$k_5 = 0.2333$ s^{-1}, $K_{5M} = 71.7$ nM	[76]
	M	$k_{xa5} = 4.333$ x 10^{-2} s^{-1}, $K_{xa5M} = 10.4$ nM	[76]
PLS	M	$k_{PLA-12a} = 0.0013$ s^{-1}, $K_{PLA-12aM} = 270$ nM	[105]
PC	M	$k_{PC} = 0.65$ s^{-1}, $K_{PCM} = 3190$ nM	[123]
	M	$k_{PLA} = 0.2$ s^{-1}, $K_{PLAM} = 18$ nM	[67]
XIIa	F	$h_{12} = 1.416$ x 10^{-2} s^{-1}	[109]
	S	$h_{12}^{C1} = 3.7$ x 10^{-6} nM^{-1} s^{-1}	[93]
	S	$h_{12}^{A3} = 3.645$ x 10^{-8} nM^{-1} s^{-1}	[92]
	S	$h_{12}^{L2} = 1.833$ x 10^{-7} nM^{-1} s^{-1}	[93]
kalli	F	$h_{kalli} = 1.133$ x 10^{-2} s^{-1}	[125]
XIa	S	$h_{11}^{C1} = 2.3$ x 10^{-6} nM^{-1} s^{-1}	[72]
	S	$h_{11}^{A3} = 1.0$ x 10^{-6} nM^{-1} s^{-1}	[115]
	S	$h_{11}^{L1} = 2.167$ x 10^{-7} nM^{-1} s^{-1}	[107]
IXa	S	$h_9 = 2.233$ x 10^{-7} nM^{-1} s^{-1}	[130]
Xa	S	$h_{10} = 3.05$ x 10^{-6} nM^{-1} s^{-1}	[130]
	S	$h_{TFPI} = 0.008$ nM^{-1} s^{-1}	[5]
IIa	S	$h_2 = 4.816$ x 10^{-6} nM^{-1} s^{-1}	[130]
Ia	M	$h_1 = 25$ s^{-1}, $H_{1M} = 250000$ nM	[27]
VIIIa	F	$h_8 = 0.0037$ s^{-1}	[84]
	M	$h_{C8} = 7.055$ x 10^{-2} s^{-1}, $H_{C8M} = 179$ nM	[121]
Va	F	$h_5 = 2.75$ x 10^{-3} s^{-1}	[32]
	M	$h_{C5} = 0.17$ s^{-1}, $H_{C5M} = 14.6$ nM	[114]
PLA	S	$h_{PLA} = 4.3$ x 10^{-3} nM^{-1} s^{-1}	[56]
APC	S	$h_{PC} = 1.1$ x 10^{-8} nM^{-1} s^{-1}	[47]

Table 2.4: Reaction kinetics and rate constants. "M" denotes Michaelis-Menten rate kinetics, and "F" and "S" denote first- and second-order rate kinetics, respectively.

$$R_{XIa} = \frac{k_{11}[IIa][XI]}{K_{11M} + [XI]} + \frac{k_{12a}[XIIa][XI]}{K_{12aM} + [XI]} - [XIa]\left(h_{11}^{C1}[C1INH] + h_{11}^{A3}[ATIII] + h_{11}^{L1}[\alpha_1 AT]\right) \tag{2.11}$$

$$R_{XI} = -\frac{k_{11}[IIa][XI]}{K_{11M} + [XI]} - \frac{k_{12a}[XIIa][XI]}{K_{12aM} + [XI]} \tag{2.12}$$

$$R_{C1INH} = -\left(h_{12}^{C1}[XIIa] + h_{11}^{C1}[XIa]\right)[C1INH] \tag{2.13}$$

$$R_{IXa} = \frac{k_9[XIa][IX]}{K_{9M} + [IX]} - h_9[IXa][ATIII] \tag{2.14}$$

$$R_{IX} = -\frac{k_9[XIa][IX]}{K_{9M} + [IX]} \tag{2.15}$$

$$[Z] = \frac{[VIIIa][IXa]}{K_{dZ}} \tag{2.16}$$

$$R_{Xa} = \frac{k_{10}[Z][X]}{K_{10M} + [X]} + \frac{k_{9a10}[IXa][X]}{K_{9a10M} + [X]} - h_{10}[Xa][ATIII] - h_{TFPI}[TFPI][Xa] \tag{2.17}$$

$$R_X = -\frac{k_{10}[Z][X]}{K_{10M} + [X]} - \frac{k_{9a10}[IXa][X]}{K_{9a10M} + [X]} \tag{2.18}$$

$$[W] = \frac{[Va][Xa]}{K_{dW}} \tag{2.19}$$

$$R_{IIa} = \frac{k_2[W][II]}{K_{2M} + [II]} - h_2[IIa][ATIII] \tag{2.20}$$

$$R_{II} = -\frac{k_2[W][II]}{K_{2M} + [II]} \tag{2.21}$$

$$R_{Ia} = \frac{k_1[IIa][I]}{K_{1M} + [I]} - \frac{h_1[PLA][Ia]}{H_{1M} + [Ia]} \tag{2.22}$$

$$R_I = -\frac{k_1[IIa][I]}{K_{1M} + [I]} \tag{2.23}$$

$$R_{tPA} = 0 \tag{2.24}$$

$$R_{VIIIa} = \frac{k_8[IIa][VIII]}{K_{8M} + [VIII]} - h_8[VIIIa] - \frac{h_{C8}[APC][VIIIa]}{H_{C8M} + [VIIIa]} \tag{2.25}$$

$$R_{VIII} = -\frac{k_8[IIa][VIII]}{K_{8M} + [VIII]} \tag{2.26}$$

$$R_{Va} = \frac{k_5[IIa][V]}{K_{5M} + [V]} + \frac{k_{xa5}[Xa][V]}{K_{xa5M} + [V]} - h_5[Va] - \frac{h_{C5}[APC][Va]}{H_{C5M} + [Va]} \tag{2.27}$$

$$R_V = -\frac{k_5[IIa][V]}{K_{5M} + [V]} - \frac{k_{xa5}[Xa][V]}{K_{xa5M} + [V]} \tag{2.28}$$

$$R_{PLA} = \frac{k_{PLA-12a}[XIIa][PLS]}{K_{PLA-12aM} + [PLS]} + \frac{k_{PLA}[tPA][PLS]}{K_{PLAM} + [PLS]} - h_{PLA}[PLA][\alpha_2 AP] \tag{2.29}$$

$$R_{PLS} = -\frac{k_{PLA-12a}[XIIa][PLS]}{K_{PLA-12aM} + [PLS]} - \frac{k_{PLA}[tPA][PLS]}{K_{PLAM} + [PLS]} \tag{2.30}$$

$$R_{APC} = \frac{k_{PC}[IIa][PC]}{K_{PCM} + [PC]} - h_{PC}[APC][\alpha_1 AT] \tag{2.31}$$

$$R_{PC} = -\frac{k_{PC}[IIa][PC]}{K_{PCM} + [PC]} \tag{2.32}$$

$$R_{TFPI} = -h_{TFPI}[TFPI][Xa] \tag{2.33}$$

$$R_{ATIII} = -\left(\begin{array}{c} h_9[IXa] + h_{10}[Xa] + h_2[IIa] \\ + h_{11}^{A3}[XIa] + h_{12}^{A3}[XIIa] \end{array} \right)[ATIII] \tag{2.34}$$

$$R_{\alpha_1 AT} = -h_{PC}[APC][\alpha_1 AT] - h_{11}^{L1}[XIa][\alpha_1 AT] \tag{2.35}$$

$$R_{\alpha_2 AP} = -h_{PLA}[PLA][\alpha_2 AP] - h_{12}^{L2}[XIIa][\alpha_2 AP] \tag{2.36}$$

2.3 Modeling Clotted Blood

Fibrin monomers are the ultimate product of the biochemical model, and the fluid within computational elements exceeding a fibrin concentration threshold of 350 nM is treated as clotted blood. The threshold was employed by LaCroix and Anand[61] based on experimental measurements reported by Ovanesov et al.[88] Clots are typically complex structures composed of fibrin, red blood cells, white blood cells, and platelets, and have complex composition-dependent and shear-dependent mechanical properties. How-

ever, for simplicity, thrombus is simulated using the viscoelastic fluid model developed by Anand et al.[2,4] to describe the fluid properties of the clotted blood. The authors proposed a thermodynamically rigorous formulation using an Oldroyd-B type rate model to treat clotted blood as a highly viscous viscoelastic fluid. They corroborated this framework via comparison with experimental data. The apparent viscosity (μ_{app}) for fluid in computational elements where [Ia] $\geq$ 350 nM is defined, as a function of local shear rate magnitude, by the following expressions:

$$\mu_{app} = \frac{\frac{\mu\lambda}{\chi} + \eta_1}{2} \tag{2.37}$$

$$\lambda = \frac{1}{\left[1 + \frac{1}{4\chi^2}|\dot{\gamma}|^2\right]^{\frac{1}{3}}} \tag{2.38}$$

$$\chi = K\left[\frac{2\dot{\gamma}^2}{4\chi^2}\frac{1}{\left[1 + \frac{1}{4\chi^2}|\dot{\gamma}|^2\right]^{\frac{1}{3}}}\right]^n \tag{2.39}$$

For coarse ligated blood clots, Anand et al.[2] used curve fitting to obtain the following parameter values: K = 2.2 s^{-1}, μ = 4.9 Pa, η_1 = 0.1 Pa-s and n = 0.1. A minimization function is used to solve for the value of χ. This model results in clotted blood having a shear-dependent viscosity 10-80 times greater than that of unclotted blood (see Figure 2.1). To improve simulation speed, the viscosity within each computational element determined to be clotted blood is interpolated from a table of μ_{app} values precomputed over a range of expected shear rates.

2.4 Boundary and Initial Conditions for Biochemical Model

To simulate an unperturbed biochemical state, and fresh blood entering the simulated domain, normal physiologic protein concentrations (listed in Table 2.1) are applied at

t=0 s and at the flow inlets. All activated enzymes are given initial and inlet concentrations of zero, except for XIIa which is set to 0.1% of XII's initial/inlet concentration. All vessel and device boundaries are impermeable to all proteins except as noted here. Surface dependent activation of XII (i.e., intrinsic pathway initiation) is simulated via boundary flux terms applied to device surfaces. The flux for XII and XIIa is defined by the following gradients where the spatial coordinate, x, refers to the normal distance from the boundary:

$$\left.\frac{\partial[XII]}{\partial x}\right|_{\substack{\text{Foam}\\\text{Boundary}}} = -\left(\frac{k_{12f}[XII][XIIa]}{K_{12Mf}+[XII]} + \frac{k_{kallif}[kalli][XII]}{K_{kalliMf}+[XII]}\right)\frac{L}{D_{XII}} \tag{2.40}$$

$$\left.\frac{\partial[XIIa]}{\partial x}\right|_{\substack{\text{Foam}\\\text{Boundary}}} = \left(\frac{k_{12f}[XII][XIIa]}{K_{12Mf}+[XII]} + \frac{k_{kallif}[kalli][XII]}{K_{kalliMf}+[XII]}\right)\frac{L}{D_{XIIa}} \tag{2.41}$$

The gradients in equations 2.40 and 2.41 are formulated using reaction rate kinetics for XIIa generation and XII consumption with rate constants (see Table 2.5) measured in the presence of dextran sulfate to approximate negatively charged surfaces.[122] The resulting rates of concentration change are multiplied by L/D_i such that, given diffusion coefficient D_i, the flux results in the desired generation or depletion rate in the area defined

Parameter	Value	Source
k_{12f}	0.033 s^{-1}	[122]
K_{12Mf}	7500 nM	[122]
k_{kallif}	7.2 s^{-1}	[122]
$K_{kalliMf}$	780 nM	[122]
h_{9f}	2.7 x 10^{-4} nM^{-1} s^{-1}	[130]
h_{10f}	5.783 x 10^{-3} nM^{-1} s^{-1}	[130]
h_{2f}	1.19 x 10^{-2} nM^{-1} s^{-1}	[130]
h_{11f}^{A3}	2.67 x 10^{-5} nM^{-1} s^{-1}	[115]
h_{12f}^{A3}	4.167 x 10^{-7} nM^{-1} s^{-1}	[92]
L	1 x 10^{-5}	

Table 2.5: Boundary flux parameters.

by the characteristic length, L. For all simulations in this work, L=1 x 10^{-5} m.

Boundary flux terms are also used to simulate the accelerated inhibition of XIIa, XIa, Xa, IXa, and IIa by ATIII that has been activated by endothelium-bound heparin-like molecules. The flux terms along tissue boundaries for ATIII and each of its targets are defined by the following gradients:

$$\left.\frac{\partial[IXa]}{\partial x}\right|_{\substack{\text{Tissue}\\\text{Boundary}}} = -h_{9f}[IXa][ATIII]\frac{L}{D_{IXa}} \tag{2.42}$$

$$\left.\frac{\partial[Xa]}{\partial x}\right|_{\substack{\text{Tissue}\\\text{Boundary}}} = -h_{10f}[Xa][ATIII]\frac{L}{D_{Xa}} \tag{2.43}$$

$$\left.\frac{\partial[IIa]}{\partial x}\right|_{\substack{\text{Tissue}\\\text{Boundary}}} = -h_{2f}[IIa][ATIII]\frac{L}{D_{IIa}} \tag{2.44}$$

$$\left.\frac{\partial[XIa]}{\partial x}\right|_{\substack{\text{Tissue}\\\text{Boundary}}} = -h^{A3}_{11f}[XIa][ATIII]\frac{L}{D_{XIa}} \tag{2.45}$$

$$\left.\frac{\partial[XIIa]}{\partial x}\right|_{\substack{\text{Tissue}\\\text{Boundary}}} = -h^{A3}_{12f}[XIIa][ATIII]\frac{L}{D_{XIIa}} \tag{2.46}$$

$$\left.\frac{\partial[ATIII]}{\partial x}\right|_{\substack{\text{Tissue}\\\text{Boundary}}} = -\begin{pmatrix} h_{9f}[IXa] + h_{10f}[Xa] + h_{2f}[IIa] \\ + h^{A3}_{11f}[XIa] + h^{A3}_{12f}[XIIa] \end{pmatrix}[ATIII]\frac{L}{D_{ATIII}} \tag{2.47}$$

These are formulated in the same fashion as equations 2.40 and 2.41. Rate constants used here are listed in Table 2.5 and are from experiments using saturating concentrations of heparin.

2.5 Discussion

2.5.1 Model Development

To study blood's response to cardiovascular implantable devices, a medium-fidelity computational thrombus model has been developed based on the work of LaCroix and Anand.[61] Their biochemical model (referred to henceforth as "LaCroix's model") was developed to study the clotting response of quiescent blood to tissue injury via the extrinsic clotting pathway. While clotting factors and reactions involved in the intrinsic pathway were included, no mechanism modeled the direct biochemical response of blood to a thrombogenic biomaterial surface. Therefore, LaCroix's model has been adapted to include boundary flux terms for factor XII activation (i.e., intrinsic pathway initiation) along device surfaces and other suitable modifications to produce the computational thrombus model described in this chapter. The resulting biochemical framework is deployed within a commercially available CFD package (STAR-CCM+), which enables the simulation of complex geometries under periodic inlet flow conditions.

To verify the correct implementation of the biochemical framework within STAR-CCM prior to making modifications to the published model, simulations were conducted in an attempt to reproduce results generated by Anand et al. using a precursor version of LaCroix's model that omits the intrinsic pathway terms.[5] The simulations were of quiescent blood plasma in a 0.002 m deep well, modeled by a 1D domain, with the bottom surface representing injured tissue which stimulates clot growth via extrinsic pathway activation. Anand et al. reported the clot size (i.e., the furthest distance from the bottom surface containing fibrin concentrations above the clot threshold) as a function of time. They presented results showing clot growth in the first 25 minutes to an extent of approximately 2 x 10^{-4} m followed by a period of clot dissolution wherein the entire clot had disappeared within 45 minutes following the start of the simulated experiment. This sim-

ulation was replicated in STAR-CCM using an identical biochemical formulation with the same model equations, rate constants, and boundary flux terms. The results from STAR-CCM (blue line) are plotted against the results published by Anand et al. (red line) in Figure 2.3. The clot size over time predicted by the STAR-CCM simulation differed significantly from the published results. It was hypothesized that the differences were due to the use of a finer mesh in STAR-CCM than the one employed by Anand et al. They used a mesh with uniform spacing of 1 x 10^{-5} m. In contrast, the STAR-CCM mesh had spacing near the thrombogenic plane as small as 5 x 10^{-7} m with the spacing gradually

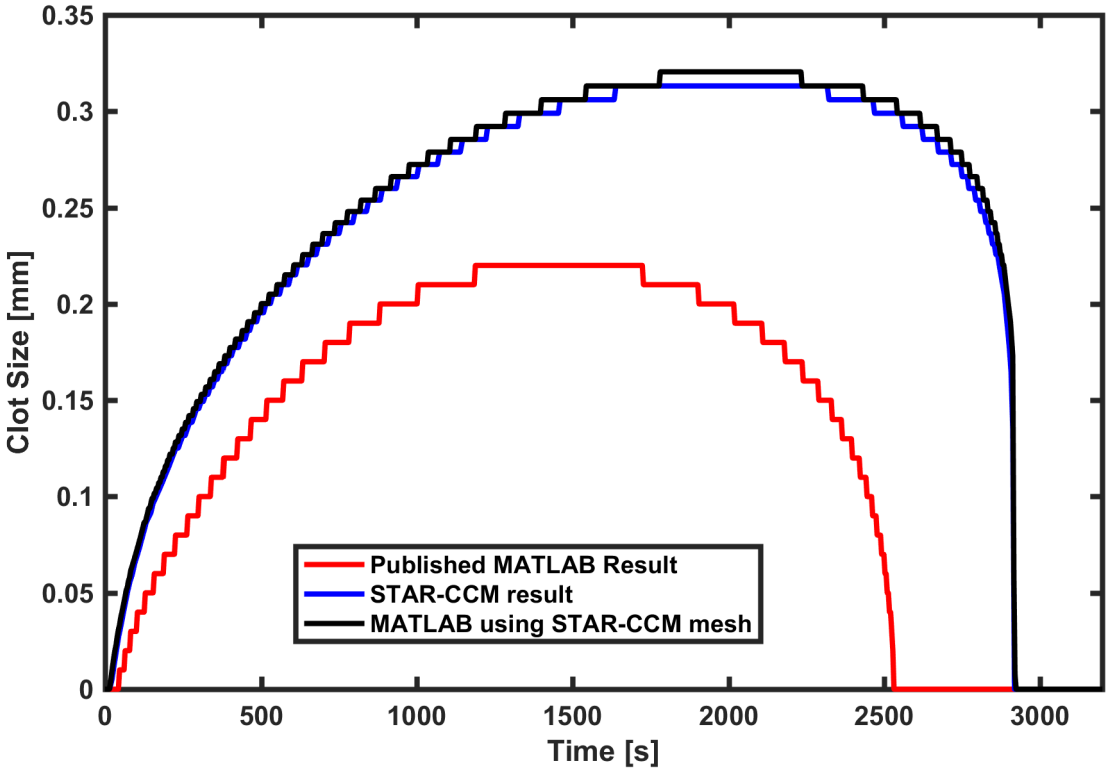

Figure 2.3: Clot size as a function of time in 1D simulations of quiescent blood plasma exposed to an injured tissue surface as predicted by the biochemical model detailed by Anand et al.[5] The original results published by Anand et al. and computed using MATLAB are shown in red. Results of the biochemical model implemented in STAR-CCM+ are shown in blue. The black curve shows the results predicted by the MATLAB code used by Anand et al. evaluated on the mesh used for the STAR-CCM+ simulation.

increasing to 1.25 x 10^{-5} m as the distance from the surface increased. The mesh contained approximately 145 computational grid locations within the 2.5 x 10^{-4} m closest to the injured tissue surface, while the mesh used by Anand et al. only had 25 grid locations in the same span. To test if the meshes accounted for the disparity in the clot size versus time results, the STAR-CCM mesh was evaluated using the MATLAB code that Anand et al. used to generate their published results. The code was generously provided by Dr. Daniel LaCroix. The black line in Figure 2.3 shows the clot size over time predicted by the MATLAB code using the STAR-CCM mesh. This result closely matches the result from the STAR-CCM simulation indicating that the STAR-CCM implementation of the biochemical framework can replicate the original model given identical mesh and model parameters. With this knowledge, further model development and testing proceeded with the goal of simulating device-induced clotting under dynamic blood flow conditions. This included the inclusion of boundary flux terms for intrinsic pathway initiation as well as the modifications discussed below to produce the model described earlier in this chapter.

In initial model testing using simple device geometries exposed to flow, the boundary flux terms prescribed by LaCroix's model to simulate extrinsic pathway activation (i.e., IX and X activation) caused very rapid clot growth (within 10 seconds) along injured tissue boundaries. The resulting spread of clot covered all biomaterial surfaces and dwarfed any effects of intrinsic pathway initiation. Therefore, these flux terms are omitted from the model to make possible the evaluation of blood's direct response to a biomaterial surface. This requires the assumption that no injured tissue is present in the domain. Further model developments should aim to restore simulation of the extrinsic pathway to more accurately represent endovascular treatments, as injury to the endothelium is likely to occur at the device-vessel interface.

In the first simulations of blood contact with a device surface, the flux terms representing contact activation of the intrinsic pathway resulted in insufficient fibrin generation

for clot formation (maximum fibrin concentrations plateaued around 10 nM). In these simulations, thrombin as well as XIIa, XIa, IXa, and Xa were greatly inhibited by ATIII. In LaCroix's model, ATIII's inhibitory activity is accelerated by saturating concentrations of heparin assumed to be present in the domain. Clinically, heparin is used during endovascular procedures to prevent clotting on catheters, guidewires, and other blood-contacting devices. Thus, it is not surprising that the assumed saturating concentrations of heparin – those concentrations that yield the most efficient ATIII activity – prevented fibrin generation in the simulations. However, these heparin concentrations vary for each reaction and exceed pharmacologically relevant concentrations in some cases. Further, ATIII acceleration by heparin is dose dependent and can even be reduced if heparin concentrations are too great.[92,115,130] To accurately reflect heparin's effect on ATIII, the rate constants involved in enzyme inhibition by ATIII (i.e., h_2, h_2, h_{10}, h_{11}^{A3}, and h_{12}^{A3}) would need to be defined as functions of local heparin concentration and an additional advection-diffusion-reaction equation would be required to track heparin concentrations in the domain. Limited kinetic data for these reactions would make this framework difficult to implement. For simplicity, the heparin assumption is removed and the rate constants are replaced with values that represent a case where no heparin is present in the blood. While heparin is assumed to be absent within the domain, heparin-like molecules are assumed to exist along vessel walls in sufficient numbers to produce a localized saturating effect on ATIII. *In vivo*, these molecules line the endothelium and enhance ATIII activity to prevent clot growth away from thrombogenic stimuli.[59] This effect is modeled using boundary flux terms on vessel boundaries where heparin-enhanced ATIII activity is prescribed. The result is a boundary layer along vessel walls free of fibrin generation and the ability for the clotting cascade to progress elsewhere, especially at surfaces stimulating the intrinsic pathway. This implementation for ATIII activity ignores the effects of clinically administered heparin during endovascular procedure. However, only clotting rates, and not the patterns of clot growth,

are expected to be impacted.

With heparin no longer assumed to be present in the domain, ATIII's inhibitory ability is reduced making it less effective at preventing unstimulated thrombus formation. Consequently, the model predicted clotting where it was not expected. This effect was evaluated in simulations representing blood flow in a healthy vessel which was modeled as a long straight tube. No flux terms for extrinsic or intrinsic pathway initiation were applied to the vessel wall to model a case where no tissue injury or negatively charged surfaces were present.

This healthy vessel simulation was expected to result in negligible fibrin generation and no thrombus formation. In contrast to LaCroix's model, which implies the presence of negatively charged particles in the domain that accelerate XII activation and intrinsic pathway initiation, the version of the model tested here is defined such that XII activation is only accelerated at a boundary defined as a negatively charged surface. Where LaCroix's model defines XII activation using rate constants measured in the presence of dextran sulfate, the model tested here uses slower rate constants measured in the absence of negatively charged particles and surfaces. Thus, XII activation in the domain should be negligible and intrinsic pathway initiation should not be possible where no thrombogenic surface is defined.

Despite these expectations, the model predicted clot growth along the wall near the distal end of the healthy vessel. Fibrin generation was possible in this case because all active enzymes were given non-zero initial and inlet conditions as defined in LaCroix's model. Thus, the simulation is initiated with the clotting cascades in an active state that is reinforced by active enzymes entering the domain at the inlet. Thrombin has the largest impact here. In addition to converting fibrinogen to fibrin, thrombin provides positive feedback to the clotting cascades as it is an additional activator for several clotting factors. Given that thrombin is a more efficient activator of XI – the second factor activated in the

intrinsic pathway – than XIIa is,[35] the clotting cascades can progress despite little to no XII activation. LaCroix's model avoids this issue because ATIII, enhanced by assumed saturating concentrations of heparin, aggressively inhibits most of the activated factors, including thrombin, preventing the progression of the clotting cascades.

To accommodate the removal of the heparin assumption as discussed earlier, the unwanted fibrin generation seen in the healthy vessel simulation is mitigated by assigning inlet and initial concentrations of zero to all active enzymes (i.e., XIa, Xa, IXa, VIIIa, Va, IIa, etc.), with the exception of XIIa. Autoactivation (XII activation by XIIa) and reciprocal activation (XIIa activates kallikrein which activates XII) of XII would not be possible if XIIa was completely absent. Therefore, a small non-zero initial concentration is applied to XIIa to act as the initial trigger for contact activation of the intrinsic pathway. While unperturbed blood *in vivo* may contain such trace amounts of XIIa that facilitate further XII activation, other mechanisms are more likely responsible for the initial XIIa generation.[19,53] However, details regarding the reaction kinetics associated with these mechanisms are not yet available in the literature. Thus, the simpler case is represented in the final thrombus formation model.

This new set of initial conditions prohibited fibrin generation due to a reliance of thrombin as the predominate or only activator of certain clotting factors such as V and VIII. With no thrombin at t=0 s, VIII and V activation is impossible and tenase and prothrombinase cannot form, preventing thrombin generation. To circumvent this dependence, two reactions were added to the biochemical framework. First, the direct activation of X by IXa bypasses the need for the tenase complex and VIIIa.[95] The second reaction allows the resulting Xa to activate factor V, enabling prothrombinase generation, and ultimately thrombin production. These reactions are minor compared to the positive feedback effect of thrombin, but it has been proposed that they are vital in the initial stages of the clotting process.[76]

2.5.2 Model Limitations

The result of the above adaptations to LaCroix's model is a framework that is capable of simulating device-induced thrombosis in a reasonable manner, as demonstrated in the following chapters; however, the model formulation detailed in this chapter is subject to several limitations that should be addressed in future model iterations. For instance, the biochemistry involved in thrombus formation, and the environment in which it occurs, is highly complex. Twenty-eight biochemicals, assumed to be the most important to clot formation, are considered in the present model. However, the biochemical formulation could be made more physiologically relevant by incorporating more proteins and biochemical reactions as done by Kuharsky et al. and Luan et al. whose computational models included 59 and 92 constituents, respectively.[58,65] Further, the current model does not track individual red blood cells or platelets, which contribute to the blood's rheology, and the structure and mechanical properties of blood clots. Some models have included tracking of individual red blood cells or platelets; however, these are typically applied to very small and non-complex domains.[133,134] Adapting such techniques to larger and more complex geometries, such as foam-filled aneurysms of interest in this work, would be too computationally demanding given current capabilities.

The interactions between blood and biomaterial surfaces, responsible for intrinsic pathway initiation, are modeled using rate constants experimentally obtained using dextran sulfate.[122] While dextran sulfate is commonly used as an analog for negatively charged surfaces, it is unknown how closely this represents the rate-enhancing effect on XII activation specific to the foam strut surface. Furthermore, the rate of contact activation of XII has been shown to vary based on the surface's hydrophobicity.[38,39,136] The current model cannot distinguish between different biomaterials as it only incorporates a single set of rate constants to describe a surface's effect on XII activation. Thus, limiting the model's

ability to compare different devices of interest, such as polymeric foam and platinum coils as aneurysm treatments. It would be ideal to define the rate constants included in the flux terms for XII and XIIa at device surfaces (k_{12f} and K_{12Mf} in equations 2.40 and 2.41) as functions of surface hydrophobicity; however, experimental data to do so are not currently available.

The boundary flux terms for factor XII contact activation and the inhibitory action of heparin-enhanced ATIII (equations 2.40–2.47) are formulated such that an expected net concentration change for a species, as experimentally measured, is reduced as if it were the result of diffusion.[2] The characteristic length defines the volume over which the total concentration change occurs due to the defined gradient. Thus, larger characteristic lengths produce greater flux across the boundary. This could have implications on how fast initial clot formation occurs and how difficult it is for clot to form on vessel walls. Physically, these reactions take place close to the boundary, suggesting a small characteristic length is appropriate; however, small characteristic lengths could render the flux terms' effect negligible. In the current model, the characteristic length is chosen, somewhat arbitrarily, to coincide with the foam strut diameter. Model stability also factored into the choice of characteristic length. Larger values (e.g., those consistent with foam pore diameters) produced instability in the near-boundary gradients of the constituents subjected to boundary flux that prevented sufficient convergence within each time step.

An undesirable and likely non-physiological result observed in model testing is the spreading of large amounts of clot downstream from a thrombogenic stimulus as a result of mass transport of fibrin out of already clotted blood. This is largely the result of omitting fibrinoligase (factor XIIIa) from the biochemical model, which crosslinks fibrin monomers within a clot, thereby fixing them in place.[34,106] Without XIIIa activity, fibrin is freely advected from the clot and accumulates downstream in concentrations exceeding the clot threshold. This could be mitigated by incorporating factors XIII and XIIIa into the

biochemical model, and incorporating the conversion, catalyzed by XIIIa, of free fibrin monomers (Ia) to an additional crosslinked fibrin form. This would reduce the large fibrin concentration gradient across clot boundaries, and limit fibrin advection from the clot.

3. MODELING CLOT FORMATION IN A SHAPE MEMORY POLYMER FOAM-TREATED ANEURYSM

3.1 Introduction

The aim of this chapter is to model the transient clot growth within intracranial aneurysms treated with shape memory polymer foam. After endovascular placement within the aneurysm sac, the foam serves as a scaffold for clot growth, resulting in aneurysm occlusion and, ideally, isolation of the aneurysm from parent artery flow.[48, 100, 102] The hemodynamics of this treatment have been previously examined computationally by Ortega et al.[86] The foams were found to greatly reduce the flow within the aneurysms, resulting in areas of flow stagnation and reduced fluid shear. Ortega et al. used the flow field solution and a low-fidelity thrombus model to predict initial locations of clot formation within the foam-treated aneurysms, producing estimates of thrombus filling of up to 5.1% of the aneurysm's post-treatment volume. To further elucidate the clotting dynamics within foam-treated aneurysms, a custom medium-fidelity model – adapted from the work of LaCroix and Anand[61] and described in Chapter 2 – is applied to a 2D simulation of a foam-treated aneurysm at the basilar artery bifurcation under periodic blood flow conditions. The clotting model employed by Ortega et al. is also applied to the foam-filled aneurysm geometry under identical flow conditions. This low-fidelity model uses parameters derived from the time-averaged flow field to identify locations of likely clot formation. Those results provide a comparison for the medium-fidelity model to a low-fidelity approach representative of the methods commonly used to predict device-induced clot formation.

3.2 Methods

3.2.1 Foam-Filled Aneurysm Geometry

The medium-fidelity computational thrombus model described in Chapter 2 has been applied to estimate the transient clot formation within a foam-treated intracranial aneurysm. The foam is a low density porous material with an intricate network of pores, struts, and membranes. Length scales ranging from 1 x 10^{-6} m (required to resolve boundary concentration gradients) to 0.001 m (foam pore diameter) necessitate large meshes to model clot formation within foam geometries. Also, hundreds of thousands of time steps (dt=0.002 s) are required to resolve transient clot growth throughout the hundreds of seconds it takes to achieve full aneurysm occlusion. These factors, and the large number of model equations, result in simulations that are computationally prohibitive for 3D geometries; therefore, all simulations are conducted using a 2D geometry to reduce computational cost. This reduces mesh sizes from several hundred million elements down to a few hundred thousand. Simulations using the 2D mesh take about 250 hours to complete using 288 parallel 2.8 GHz Intel processors.

While patient-specific aneurysm geometries are readily obtainable, for simplification, an idealized geometry is adapted from measurements of aneurysms located at the basilar artery bifurcation (see Figures 3.1a-3.1b). The basilar artery is modeled as a straight channel with width of 3.2 x 10^{-3} m and length of 0.1 m – sufficiently long for fully developed inlet flow. The branching arteries are modeled as straight channels 0.002 m in width and 0.06 m in length. These channel widths correspond with measured diameters for basilar arteries and their branching vessels.[51] The modeled aneurysm has dome and neck diameters of 5.73 x 10^{-3} m and 0.003 m, respectively. These dimensions were chosen based on the measurements of human aneurysms located at the basilar artery bifurcation.[90] The selected values fit within the lower end of the observed range for each

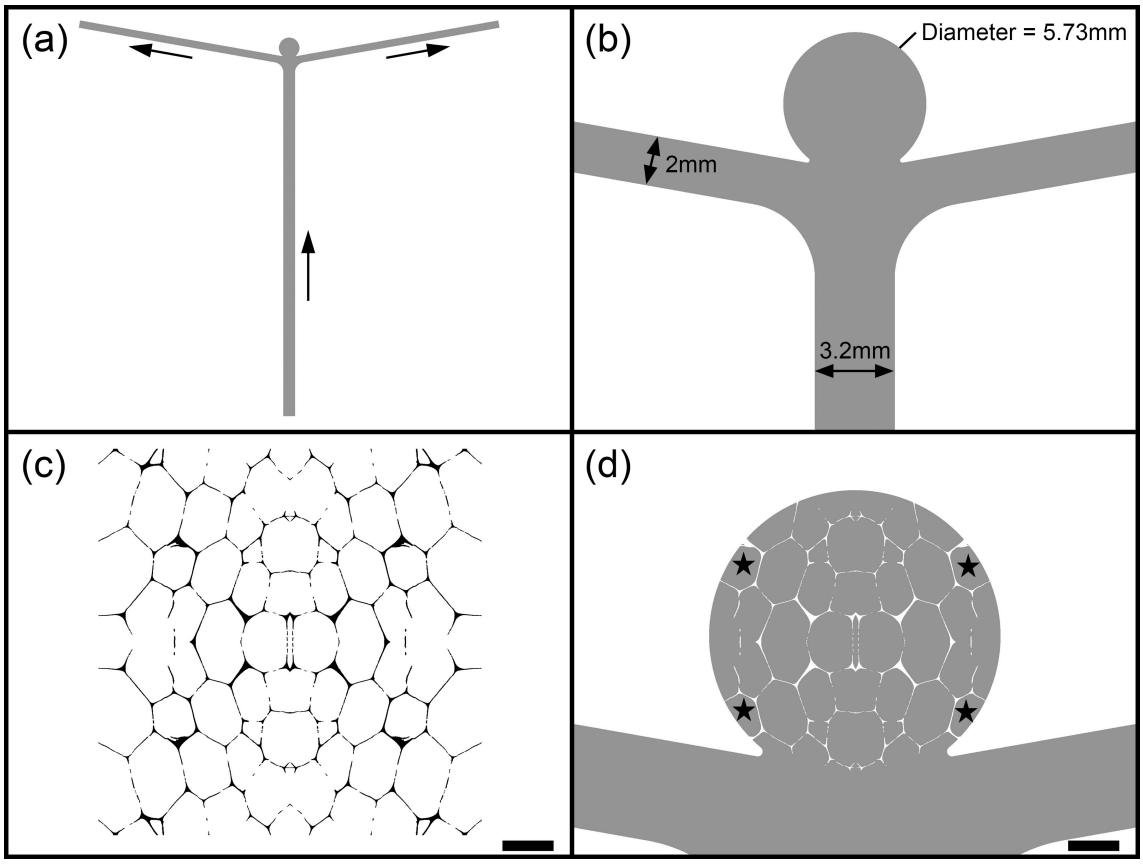

Figure 3.1: Simulation geometry. (a) Idealized bifurcation aneurysm (prior to filling with foam). Black arrows indicate the direction of flow. (b) Close view of aneurysm. (c) Isolated slice of foam from μ-CT imaging. The black features represent the individual foam struts. (d). Foam-filled aneurysm. Black stars indicate noncontiguous foam pores that are removed from the computational domain prior to simulation. The scale bar in panels (c) and (d) is 1 mm.

dimension and conform to the reported average dome to neck ratio of 1.91. The idealized aneurysm was virtually treated with foam as described by Ortega et al.[86] using foam geometry obtained from μ-CT imaging. A 2D slice of foam was isolated and placed within the aneurysm via a Boolean subtraction operation (see Figures 3.1c-3.1d).

3.2.2 Computational Meshes

The computational mesh is composed of an unstructured core mesh, with element size of 80 x 10^{-6} m outside the aneurysm and 20 x 10^{-6} m within the aneurysm, that transitions to prismatic layers that line the vessel walls (minimum thickness of 8 x 10^{-6} m), aneurysm wall (minimum thickness of 2 x 10^{-6} m), and the foam strut surfaces (minimum thickness of 1 x 10^{-6} m). The prismatic layer thickness decreases closer to the boundaries to improve resolution where velocity and concentration gradients are expected to be larger. Simulations were conducted with additional fine and coarse meshes with mesh parameters halved and doubled, respectively. No significant variations were observed between simulation outputs using the different meshes, thus confirming mesh independence (see Appendix A).

3.2.3 Low-Fidelity Model

Clot growth predictions within the foam foam-filled aneurysm geometry were generated using the medium-fidelity model detailed in Chapter 2. As a comparison to more typical device-related clotting simulations in the literature, a low-fidelity simulation was also conducted in the foam-filled aneurysm using an approach employed by Ortega et al. that correlates flow field features to likely locations of thrombus formation.[86] Areas where time-averaged shear rates are less than 54 s^{-1} (for non-Newtonian viscosity models)[21] and where residence times are greater than 240 s – the experimentally determined time required for incipient clotting of whole blood[29] – are considered locations of clot formation.

For this low-fidelity simulation, the solution for blood flow within the foam-filled aneurysm geometry was computed. Blood is treated as a non-Newtonian fluid with viscosity defined by the generalized power law model described in Chapter 2. The fluid's local residence time is modeled as the concentration of a passive scalar quantity in the domain subjected to advection only. Prohibiting diffusion ensures that the passive scalar remains

closely associated with a single packet of fluid. The concentration, C, of this quantity is governed by the equation,

$$\frac{\partial C}{\partial t} = -div\,(C\vec{v}) + S \tag{3.1}$$

where S is a local source term given a value of 1 at all points in the domain such that C increases by one unit for each unit of simulated time. Therefore, the value of C in each computational element represents the amount of time a fluid packet within that element has existed in the domain and is analogous to the residence time of that fluid.

3.2.4 Simulation Procedures and Outputs

The low- and medium-fidelity model simulations both utilize identical flow boundary conditions. All vessel and foam surfaces are made rigid, and no-slip velocity conditions are applied to each. Flow though the parent artery is assumed to be evenly split between the two branching arteries for simplicity, and the outlets are defined such that 50% of the inlet flow passes through each. However, for future simulations, the ratio of the flow rates in the two branches could be adjusted based on physiological flow rate data. To simulate the cardiac cycle, the average inlet velocity varies with time to correspond with patient-specific basilar artery velocity measurements collected at several timepoints over a single cardiac cycle.[54] The average velocity applied to the inlet at each time step is interpolated from the velocity waveform using a heartrate of 70 beats per minute (see Figure 3.2). At t=0 s, velocity in the domain is set to 0 m/s.

The biochemical boundary conditions and initial conditions described in Chapter 2 are utilized for the medium-fidelity model simulations. Flux terms for intrinsic pathway activation are applied to the foam strut boundaries and the flux terms describing ATIII's heparin-accelerated activity are applied to the vessel walls. The concentrations for each modeled constituent are set to physiological levels at the inlet and the same values are used for the initial condition. For the low-fidelity model, the value of the passive quantity

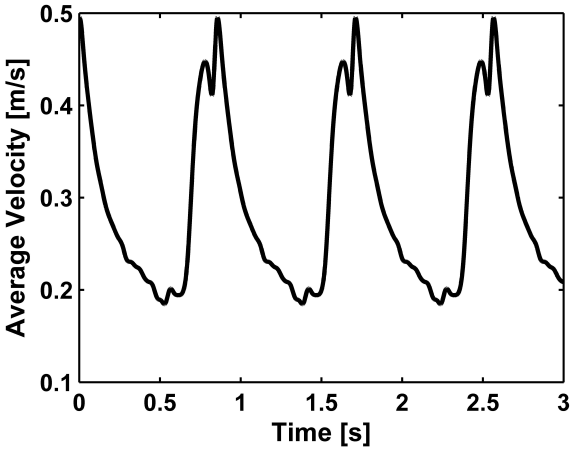

Figure 3.2: Average inlet velocity for the first 3 seconds of simulation. The waveform is periodic with frequency 1.17 Hz for a heartrate of approximately 70 beats per minute and continues unchanged for the remainder of the simulation. Data are adapted from measurements taken by Kato et al.[54]

tracking residence time (C) is set to 0 at all boundaries including the inlet and it is also set to 0 at t=0 s such that all points in the domain initially have a residence time of 0.

To initialize the medium-fidelity simulation, five thousand iterations were solved under steady state conditions with the biochemistry model disabled using the average inlet velocity for t=0 s. This generates an initial flow field estimate that is used as an initial condition for the unsteady flow solver. Then under unsteady conditions, 6 seconds of flow-only time steps were solved using a time step of 0.002 s to achieve a quasi-steady state solution wherein any start-up transients in the flow field are reduced or eliminated. Finally, for the medium-fidelity model, the biochemical model was activated and, using a time step of 0.002 s, 330 seconds of time steps were solved using 288 parallel CPUs. For each time step, enough iterations were computed to allow the residuals to decrease by at least 4 orders of magnitude. Separate simulations were conducted using time steps of 0.001 s and 0.004 s. No significant variations in simulation outputs were observed for each time step, confirming time step independence (see Appendix A). Simulations of the foam-

filled aneurysm geometry were not attempted with time steps larger than 0.004 s; however, in other test simulations, the boundary flux terms were found to be unstable when larger time steps were applied.

To assess clotting performance, aneurysm occlusion as a function of time was monitored. Occlusion was expressed as the ratio of the volume of clotted blood in the aneurysm to the volume of free space within the foam-filled aneurysm prior to thrombus formation. For these calculations, the aneurysm is bounded using an ellipsoid centered at the aneurysm center (see the first image in Figure 3.3).

For the low-fidelity simulation, the flow field is solved as described for the medium-fidelity simulations. The simulation is initialized with the same startup procedure used for the medium-fidelity simulation wherein residence time tracking is activated after a quasi-steady state solution is achieved for the flow field. Residence time tracking is activated by changing the value for the source term, S, from 0 to 1 allowing the residence time to increase with time. The residence time distribution after 2000 s – computed using a time step of 0.002 s – and the local time-averaged shear rate magnitude are used to predict the initial clotting locations.

3.3 Results

The medium-fidelity computational thrombus model described in Chapter 2 was applied to an idealized bifurcation aneurysm filled with shape memory polymer foam under pulsatile flow conditions. As a response to blood contact with thrombogenic foam surfaces, where boundary flux terms for XII activation are applied, the model predicts initiation of the intrinsic pathway, progression of the clotting cascade, and fibrin generation which leads to clot growth and ultimately aneurysm occlusion. Local fibrin concentrations begin to exceed the clot threshold of 350 nM after approximately 172 seconds.

The progression of clot growth is shown in Figure 3.3. Early in the clotting process,

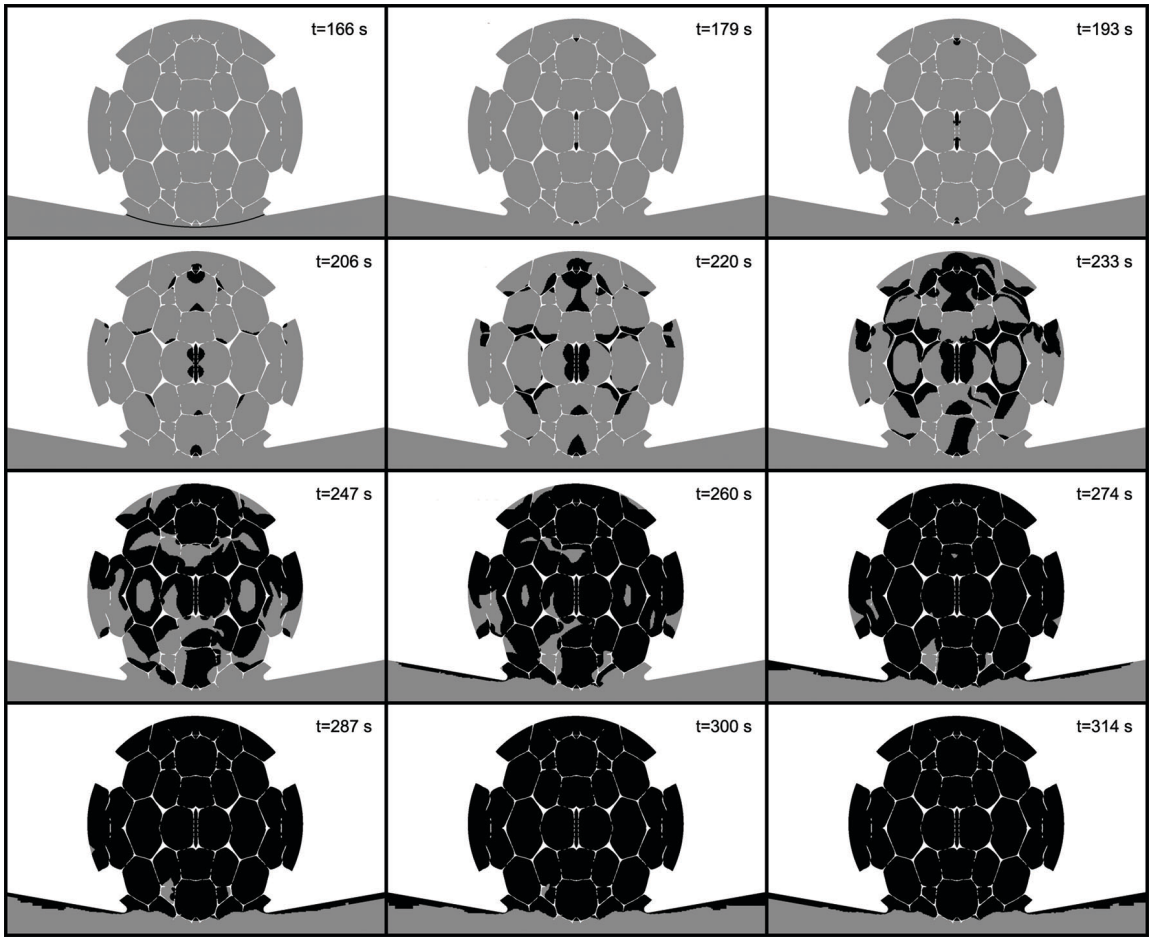

Figure 3.3: Evolution of clot distribution predicted by the medium-fidelity model. Unclotted blood in the aneurysm and the parent arteries is shown in gray. The black line in the first image (t=166 s) indicates the boundary line between blood considered inside the aneurysm and outside the aneurysm. In the remaining images, black indicates clotted blood.

thrombus is mostly localized to foam strut surfaces. Between t=200 s and t=280 s, the clot rapidly grows and spreads along the remaining struts and deep into the foam pores, filling most of the aneurysm. During this time, fibrin in the aneurysm neck spills out into the branching arteries, causing the unwanted spread of thrombus along the artery wall downstream of the aneurysm. After 280 seconds, clot growth slows as fibrin spreads to the remaining unclotted areas. The extent at which thrombus fills the aneurysm is assessed

by tracking the occlusion percentage as a function of time (Figure 3.4). This parameter measures how much available space in aneurysm (i.e., the space not occupied by foam struts) is filled with thrombus. A maximum occlusion of approximately 97.5% is achieved at t=315 s.

The relative local age of clot within the aneurysm is shown in Figure 3.5, which shows a clot age parameter, CA, defined as:

$$CA(x,y) = \frac{1}{t_2 - t_1} \int_{t_1}^{t_2} CT(x,y,t)dt \tag{3.2}$$

where t_1 is the initial clotting time, t_2 is the end of the simulation (330 s), and CT is a threshold function describing which computational elements exceed the fibrin concentration clot threshold:

$$CT(x,y,t) = \begin{cases} 1, & \text{for } [Ia](x,y,t) \geq 350 \text{ nM} \\ 0, & \text{for } [Ia](x,y,t) < 350 \text{ nM} \end{cases} \tag{3.3}$$

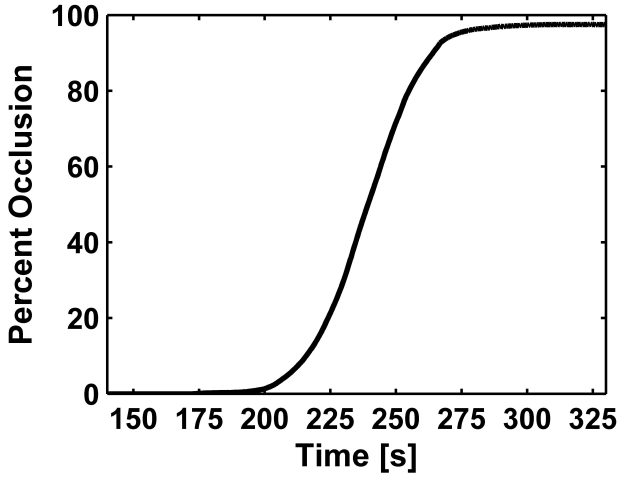

Figure 3.4: Occlusion in the foam-filled aneurysm over time as predicted by the medium-fidelity model.

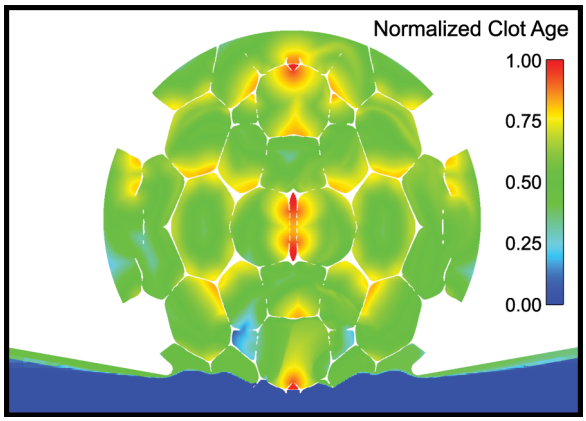

Figure 3.5: Normalized clot age throughout the occluded aneurysm at t=330 s (predicted by the medium-fidelity model). Values near 1 indicate the earliest areas to begin clotting and a value of 0 indicates that the location never contained clot.

The clot age is normalized such that the oldest clot (i.e., the location where clot first appeared) is given a value of 1 and computational elements that never exceed the fibrin threshold have a value of 0. This parameter shows that the initial clot locations are typically on the foam struts. Also, the locations with the oldest clot are typically exposed to the lowest shear rates, as can be seen in Figure 3.6a which shows the time averaged shear rate magnitude throughout the aneurysm, measured prior to clot formation.

In addition to the medium-fidelity thrombus model, a low-fidelity approach was used to predict locations of potential clot formation within the foam-filled aneurysm. Clot locations are defined as those with mean shear rate less than 54 s^{-1} and fluid residence times greater than 240 s. As shown in Figure 3.6a, most of the aneurysm meets the first criterion. The most notable exception is that flow impingement at the aneurysm neck results in shear rates 1 to 2 orders of magnitude greater than the threshold for clot formation. The residence times in the aneurysm, measured after 2000 seconds of simulated pulsatile flow, are shown in Figure 3.6b, and the low-fidelity approach predicts the clot distribution shown in Figure 3.6c. The resulting distribution corresponds to approximately 43%

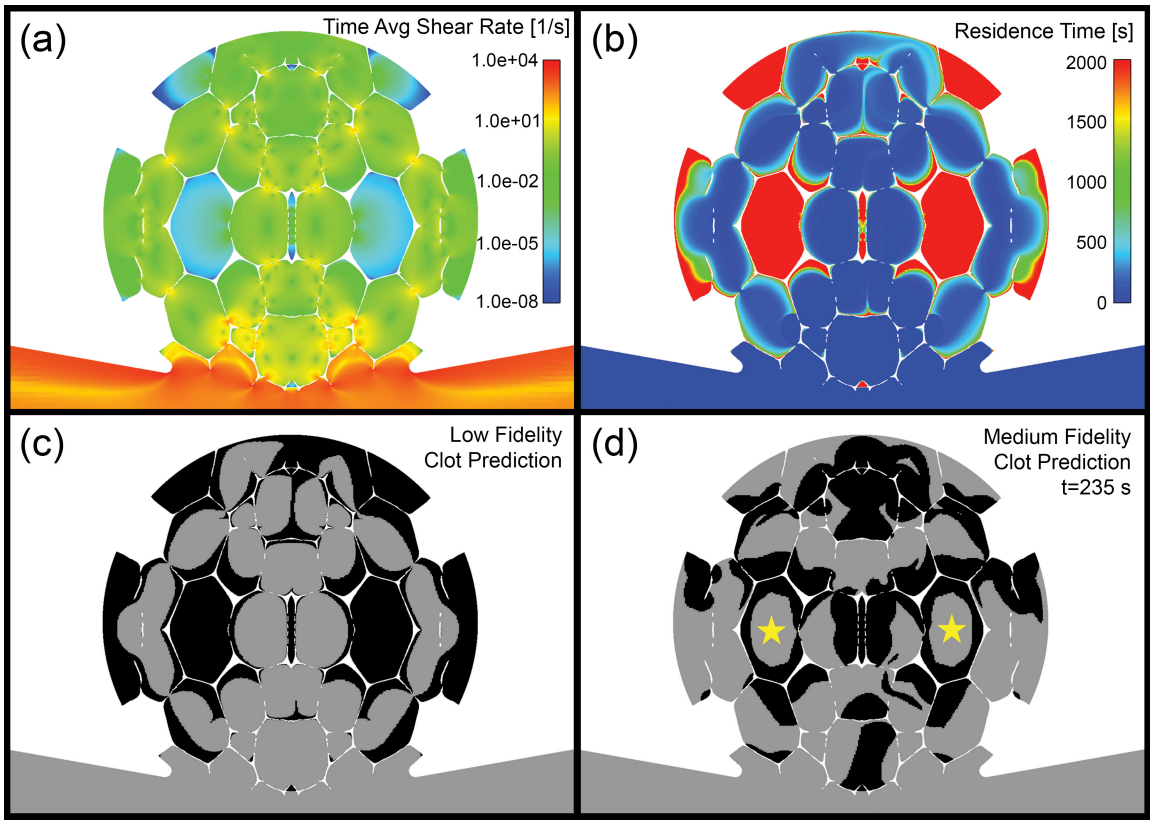

Figure 3.6: (a) Time-averaged shear rates in the foam-filled aneurysm prior to clot formation. (b) Residence time measured after 2000 seconds of non-clotting flow within the aneurysm. (c) Locations of initial clot formation predicted by the low-fidelity clotting model. The areas of clot (shown in black) have mean shear rates < 54 s^{-1} and residence times > 240 s. (d) Clot distribution predicted by the medium-fidelity model, at t=235 s, when the percent occlusion (~43%) is approximately equal to filling predicted by the low-fidelity model. Yellow stars highlight pores with high residence time where the two models differ significantly in their predictions.

aneurysm occlusion. The medium-fidelity model predicts this amount of occlusion to occur around t=235 s. The clot distribution predicted by the medium-fidelity model at this time (see Figure 3.6d) is comparable to the low-fidelity prediction at many locations (e.g., both models predict little to no clotting in the aneurysm neck). However, the low-fidelity approach predicts more clot formation in the dome and outer edges of the aneurysm as well as complete occlusion of two foam pores (denoted with yellow stars in Figure 3.6d)

that have very minimal flow. In the medium-fidelity model, these areas are slow to fill as they contain large volumes of blood that have minimal contact with the foam surface.

3.4 Discussion and Conclusion

The medium-fidelity thrombus formation model discussed in Chapter 2 was demonstrated by simulating the clotting response within an aneurysm treated with shape memory polymer foam. The predicted clotting response leads to maximum occlusion of the foam-treated aneurysm within 315 seconds, with clot filling approximately 97.5% of the post-treatment void volume. This timescale for complete occlusion is comparable to experimental occlusion times within similar foams. Rodriguez et al. found that it takes 128 ± 77 seconds for foam to embolize porcine arteries;[101] however, it was unclear if the foam was fully filled with thrombus prior to causing a pressure gradient large enough to force blood to parallel arteries. Landsman et al. tested the occlusion times of foams *in vitro* with bovine blood and found that after 270 seconds, thrombus formation in the foam produced pressure gradients 3-4 times greater than pressures expected *in vivo*.[62] Through histological sectioning, those foams were confirmed to be fully occluded.

The current medium-fidelity model predicts the unlikely spread of clot out of the aneurysm and downstream. While it would be a serious clinical event if the implanted foam resulted in instances of thromboembolism, *in vivo* testing of foams in porcine aneurysm models suggests that this is unlikely to occur.[48, 100, 102] Simulation results indicate that, outside a limited area near thrombogenic surfaces, mass transport is the major source of fibrin accumulation. This is driven by large concentration gradients at the interface between clotted blood ([Ia] > 7000 nM) and unclotted blood ([Ia] < 350 nM), suggesting that the spread of thrombus from the aneurysm may be a result of neglected biochemistry.

Many of the computational efforts presented in the literature have utilized low-fidelity methods to predict how clotting occurs when blood interacts with biomedical de-

vices. The low-fidelity model examined in this study is in partial agreement with the medium-fidelity model. Many of the clotted areas predicted by the low-fidelity model correspond to areas of early clotting predicted by the medium-fidelity model. However, the low-fidelity model is unable to capture how the advection of activating clotting factors affects clot formation within areas not near the foam strut surface. As a result, some of the areas predicted to clot by the low-fidelity model are slow to fill with thrombus in the medium-fidelity simulation.

As discussed in Chapter 2, simplifications required to formulate the medium-fidelity thrombus model limit these simulations. The represented biochemistry neglects many blood proteins that may significantly contribute to the clotting cascades. The absence of one protein, factor XIIIa, is likely responsible for the non-physiologic spread of clot away from the aneurysm. The model also generalizes the contact activation of XII using rate constants derived from experiments using dextran sulfate as an analog for the negatively charged surface. It is possible that these rate constants differ from XII activation by the foam surfaces modeled in these simulations. Further, the 2D geometry modeled here may be a poor representation of actual foam-filled aneurysms. The flow dynamics in the 2D geometry are likely very different than in the 3D geometry and the impact of the blood/surface interactions may be over or under stated given that the surface area to blood volume ratios are very different for the modeled 2D geometry and the real 3D geometry. Also, the lack of model validation with experimental data leaves uncertainty in the predicted results given the large number of model equations and experimentally-derived model parameters (i.e., about 50 rate constants).

A major goal of this work was to develop a physiologically-relevant model capable of predicting clot growth initiated by devices implanted in the vasculature. A model is described in Chapter 2 that accomplishes this goal as demonstrated in the current chapter by simulation of an aneurysm treated with an embolic foam device, elucidating the transient

progression of clot growth as a direct response to blood contact with the device surface. Such information is not attainable through low-fidelity clot modeling, which is typically employed for this type of problem. While further model development and validation is needed, the proposed framework shows promise as a tool for evaluating the relative clotting performance of cardiovascular devices to guide future device design and ultimately improve clinical outcomes.

4. MODELING CLOT FORMATION IN ANEURYSMS TREATED WITH SHAPE MEMORY POLYMER FOAM OR BARE METAL COILS

4.1 Introduction

Intracranial aneurysms, which rupture in approximately 30,000 patients per year in the United States[74] and lead to severe debilitation or death, are often treated with endovascularly delivered bare metal coils.[22,94] The coils, typically made of a platinum alloy, fill the aneurysm sac and elicit a clotting response. In optimal cases, the combination of the coils and the resulting thrombus occludes the aneurysm, thereby excluding the aneurysm from arterial flow and reducing the risk of aneurysm rupture. However, in some cases, poor filling can occur, especially in the aneurysm neck which is exposed to high velocity impinging flow.[103] The unfilled neck remnant, or residual neck, leaves the aneurysm susceptible to recanalization, growth, and rupture.[55,120] Therefore, such aneurysms often require retreatment.

To address the suboptimal outcomes associated with bare metal coil treatments, shape memory polymer foam has been proposed as an alternative embolic material for aneurysm occlusion.[68,73] Once placed in the aneurysm, the internal structure of the ultralow density foam – consisting of a complex network of pores, struts, and membranes – significantly reduces blood flow in the aneurysm[86] and provides a scaffold for thrombus formation. *In vivo* studies using porcine aneurysm models have shown foam-treated aneurysms to exhibit positive long-term healing outcomes that may improve upon outcomes associated with coil treatment.[48,100]

While *in vivo* animal studies are useful for assessing long-term treatment outcomes, these studies offer little to no information regarding the short-term clotting response which occurs in the first several minutes following treatment. Knowledge of how

this initial phase of healing occurs, and how it may be affected by device design, may be useful in predicting long-term healing outcomes. Thus, in this chapter, the medium-fidelity computational thrombus model described in Chapter 2 is used to predict the immediate clotting response within aneurysms treated with bare metal coils and shape memory polymer foams. The model uses a set of advection-diffusion-reaction equations to couple the biochemistry involved in clot formation and the hemodynamics of blood flow within the treated aneurysms to predict the transient clot growth and progression in response to blood-contacting devices. Multiple foam configurations are simulated to assess how foam pore size and orientation impact the progression of clot growth, and multiple coil configurations are simulated to represent the random nature of coil placement during treatment. The transient clotting responses are predicted for each case and the performance of the two treatment options are compared.

4.2 Methods

4.2.1 Geometries

All simulations in this chapter represent the treatment of an aneurysm located at the basilar artery bifurcation. Because 3D geometries would require very large computational meshes (more than 100 million mesh elements) and result in computationally prohibitive simulations, only 2D geometries are considered. For simplicity, an idealized geometry is modeled with dimensions based on measurements of basilar arteries, their branching vessels, and aneurysms located at the basilar artery bifurcation (see Figure 4.1). Straight channels are used to represent the basilar artery (domain inlet) and the two branching vessels (domain outlets). Channel widths of 3.2 x 10^{-3} m and 2.0 x 10^{-3} m, respectively, correspond to measured artery diameters.[51] The basilar artery channel length (0.1 m) is sufficient to provide fully developed inlet flow. Aneurysm neck and dome diameters of

3.0 x 10^{-3} m and 5.73 x 10^{-3} m are selected to conform to an average measured dome diameter to neck diameter ratio of 1.91.[90]

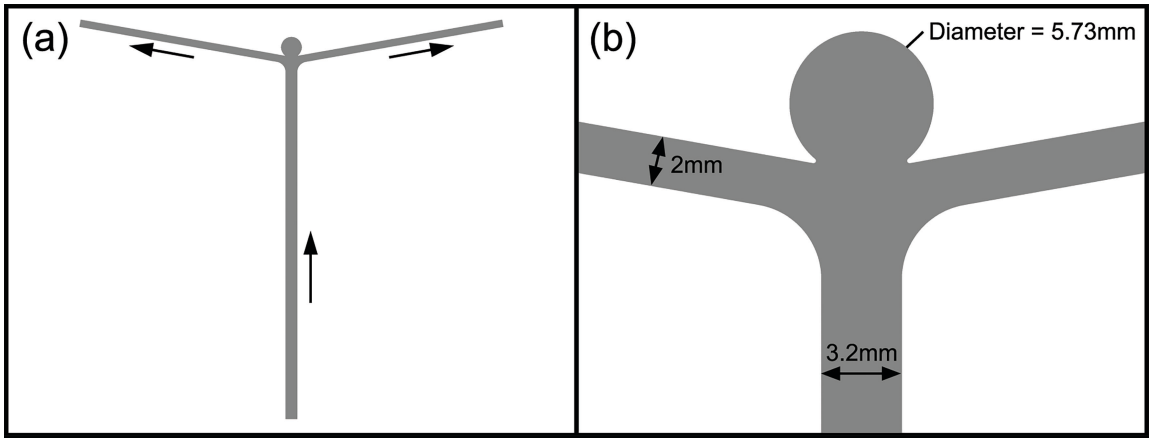

Figure 4.1: Idealized bifurcation aneurysm geometry prior to filling with foam or coils. (a) View of entire domain. Black arrows indicate flow direction. (b) Close view of aneurysm.

To virtually treat the aneurysm with foam, a digital 3D representation of the foam's internal geometry was derived from μ-CT imaging data (see Ortega et al. for more information[86]). A 2D slice, shown in Figure 4.2a, was isolated from the 3D data set and was used to create a cross section large enough to encompass the entire aneurysm. Boolean subtraction was used to fill the aneurysm with the resulting foam slice (see Figure 4.2b). To assess the effect of foam orientation on clotting, the 2D foam cross section was rotated by 45 and 90 degrees to create two additional foam-filled aneurysms. Similarly, the foam cross sections in each orientation were scaled by 1/2x prior to creating three more geometries to represent foams with a smaller pore size.

The idealized aneurysm geometry was also virtually treated with coils. A microscopy image of a micro-ground section of a coil-treated aneurysm, published by Murayama et al. (see Figure 5B of that paper),[78] was used to generate the cross-sectional coil

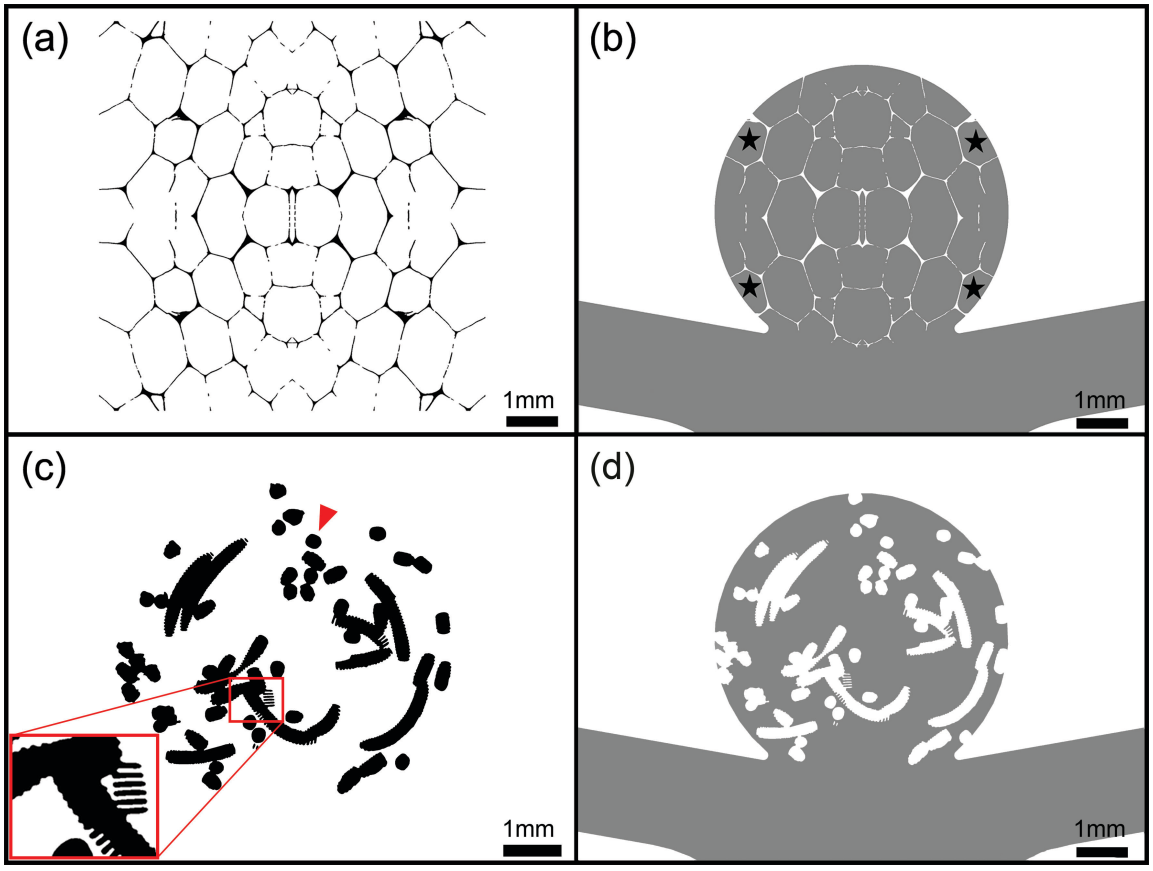

Figure 4.2: (a) 2D slice of foam (unscaled and unrotated). Black features represent individual foam struts. (b) Example foam-treated aneurysm (foam unscaled and unrotated). Black stars indicate noncontiguous foam pores that are removed from the computational domain prior to simulation. (c) Cross-sectional coil geometry. The inset shows the detail along the coil boundaries. Coils are scaled such that the coil indicated by the red arrowhead has a diameter of 0.01 in. (d) Example coil-filled aneurysm (coil case #1).

shapes. This image was selected because the aneurysm's mostly circular shape is a suitable match for the idealized aneurysm used in our simulations. CAD software was used to trace the outlines of each individual coil cross section. The empty inner core of each coil is ignored as these empty spaces would be isolated from flow in the simulations. The coil shapes, shown in Figure 4.2c, were scaled relative to the to the idealized aneurysm geometry to achieve a coil diameter of 0.01 in (0.254 x 10^{-3} m), which corresponds to

a commonly available size for coils used clinically. The coil shapes were then arranged within the idealized aneurysm to achieve a realistic distribution (see Figure 4.2d). Additional pseudo-random coil distributions were generated by randomly shifting the radial and angular position (relative to the aneurysm's center) of each coil shape. Several hundred distributions were generated and a total of six were selected with varying features of interest (e.g., packed or empty neck, high or low packing density in the aneurysm core, etc.). The aneurysm is filled with each selected coil distribution via Boolean subtraction.

The degree of filling for each aneurysm treated by foam or coils was assessed by calculating the packing density (i.e., area of coils or foam in the aneurysm divided by area of the untreated aneurysm). The total foam or coil area in the aneurysm is measured via image processing wherein the area of the unoccupied space in the aneurysm is obtained and subtracted from the total unfilled aneurysm area. Additionally, as an analog to the foam or coil surface area in contact with blood, the total length of the coil or foam boundaries in the 2D geometry is measured for each treated aneurysm.

The computational mesh for each geometry is composed of an unstructured core mesh, with element size of 80 x 10^{-6} m outside the aneurysm and 20 x 10^{-6} m within the aneurysm, that transitions to prismatic layers that line the vessel walls (minimum thickness of 8 x 10^{-6} m), aneurysm wall (minimum thickness of 2 x 10^{-6} m), and the foam strut and coil surfaces (minimum thickness of 1 x 10^{-6} m). The prismatic layer thickness decreases closer to the boundaries to improve resolution where velocity and concentration gradients are expected to be larger. These mesh parameters match the ones used for the simulations in Chapter 3. Those simulations were conducted in a similar foam-filled aneurysm and the mesh parameters were shown to produce mesh-independent results (see Appendix A). The geometries under consideration here are generally similar to the one in Chapter 3, which is identical to the unscaled and unrotated foam case, and the flow magnitudes within the aneurysms are expected to be similar since the simulations in this chapter will have

identical inlet velocity conditions as the previous simulations. Therefore, the previous mesh parameters are assumed to be adequate for mesh-converged simulations within these new geometries. The resulting meshes for the coil and unscaled foam geometries have between 200,000 and 400,000 elements and the 1/2x-scaled foam geometries have between 800,000 and 1,000,000 mesh elements.

4.2.2 Modeling Blood Flow

Blood flow is modeled by treating blood as a homogenous, shear-thinning fluid. The flow field is obtained using a commercially available finite volume CFD package (STAR-CCM+, version 9.04.009) to solve the equations for mass and momentum balance for an incompressible fluid,

$$\frac{\partial \rho}{\partial t} + \rho \left(\nabla \cdot \vec{v} \right) = 0 \tag{4.1}$$

$$\rho \frac{\partial \vec{v}}{\partial t} + \nabla \cdot (\rho \vec{v} \vec{v}) = -\nabla p + \nabla \cdot (2\mu(\dot{\gamma}) D) \tag{4.2}$$

where $\vec{v}$ and p are the velocity vector and pressure, the density, ρ, is 1060 kg/m^3, and $D = \frac{1}{2}\left[\nabla \vec{v} + (\nabla \vec{v})^T\right]$ is the symmetric part of the velocity gradient tensor. A generalized power law model is used to model blood's non-Newtonian behavior. The apparent viscosity, μ, as a function of local shear rate magnitude, $\dot{\gamma}$, is given by

$$\mu(\dot{\gamma}) = \lambda |\dot{\gamma}|^{n-1} \tag{4.3}$$

where the power law consistency (λ) and index (n) are also functions of local shear rate:

$$\lambda(\dot{\gamma}) = \mu_\infty + \Delta\mu \exp\left[-\left(1 + \frac{|\dot{\gamma}|}{a}\right) \exp\left(-\frac{b}{|\dot{\gamma}|}\right)\right] \tag{4.4}$$

$$n(\dot{\gamma}) = n_\infty + \Delta n \exp\left[-\left(1 + \frac{|\dot{\gamma}|}{c}\right) \exp\left(-\frac{d}{|\dot{\gamma}|}\right)\right] \tag{4.5}$$

The parameters in equations 4.4 and 4.5 are taken from Ballyk et al. who fit the model to experimentally obtained measurements of blood viscosity at various shear rates: $\Delta\mu$=0.025 Pa-s, Δn=0.45, a=50, b=3, c=50, and d=4.[7] To approximate blood as a Newtonian fluid at high shear rates, μ_∞ and n_∞ are set to 0.0035 Pa-s and 1.0, respectively.

4.2.3 Modeling Biochemistry of Clot Formation

Clot formation occurs through a series of biochemical reactions, comprising the coagulation or clotting cascades, which are initiated via blood exposure to tissue injury (extrinsic pathway) or a negatively charged surface such as that of a biomedical device (intrinsic pathway). These biochemical processes are simulated using the medium-fidelity model described in Chapter 2. The concentrations of 28 proteins present in blood – subjected to mass transport via advection and diffusion, but assumed to be small enough to not affect the bulk fluid properties of blood – are tracked over time using a set of advection-diffusion-reaction equations,

$$\frac{\partial [Y_i]}{\partial t} + div\left([Y_i]\,\vec{v}\right) = div\left(D_i \nabla [Y_i]\right) + R_i \tag{4.6}$$

where $[Y_i]$ and D_i are the concentration and diffusion coefficient for each. The generation or depletion of each protein, via biochemical reaction with other modeled proteins, is incorporated via the reactive source term, R_i. The 28 biochemicals included in the model are assumed to be the most important for clot formation. These include factor XII, which is activated upon contact with a negatively charged surface; intermediate clotting factors such as factor X and thrombin; several regulatory proteins such as antithrombin III (ATIII), which competitively binds with key factors in the clotting cascade to significantly inhibit clot generation; and the ultimate product of the clotting cascade, fibrin, which polymerizes into long, sticky fibers that form a mesh that catches blood cells and platelets to form a

blood clot. A complete list of biochemicals and model parameters, as well as definitions of the reactive source terms, can be found in the Chapter 2.

4.2.4 Modeling Clotted Blood

Fibrin concentrations are tracked at all points over time and computational elements exceeding a set concentration threshold are treated as clotted blood. The fluid in these elements is treated as a homogenous fluid with shear-dependent viscosity modeled using an Oldroyd-B type rate equation developed by Anand et al. that approximates the shear-thinning behavior of blood clots.[2,4] This results in viscosities 10-80 times greater than unclotted blood. Refer to Chapter 2 for further information.

4.2.5 Boundary Conditions and Initial Conditions

All artery, aneurysm, foam, and coil surfaces are assumed to be rigid, and no-slip velocity conditions are applied to each. The average inlet velocity is defined for each time step to correspond to the average velocity waveform measured by Kato et al. in a human basilar artery.[54] A heart rate of 70 beats per minute is assumed (see Figure 3.2). Initial conditions for the biochemical model (i.e., biochemical concentrations in the domain at t=0 s) are set to represent an unperturbed physiological state. Similar conditions are applied at the inlet to model fresh blood entering the domain throughout the simulation. The interactions between blood and the foam and coil surfaces that lead to intrinsic pathway activation are incorporated via boundary flux terms that produce a net change in concentration for each of the biochemicals involved in surface-mediated biochemical reaction (i.e., factor XII and its activated form, factor XIIa). Similarly, the regulatory activity of ATIII, which is enhanced along artery walls, is also simulated via boundary flux terms applied to vessel and aneurysm wall boundaries. Refer to the Chapter 2 for a list of flux terms definitions and initial/inlet biochemical concentrations.

4.2.6 Simulation

For each simulation, an initial steady-state flow field solution is obtained by computing 5000 iterations with the inlet velocity for t=0 s applied. This solution is used as the initial condition for 6 seconds of unsteady, flow-only simulation (dt=0.002 s) ensuring that start up transients are reduced or eliminated prior to simulating clot formation. Finally, the biochemical model is enabled and, using a time step of dt=0.002 s, several hundred seconds are simulated until clot formation in the aneurysm is complete.

During each simulation, the distribution of clotted blood in the aneurysm is tracked. Clotting performance is quantified by monitoring aneurysm occlusion represented over time as the ratio of the area of clotted blood within the aneurysm to the area of free space in the treated aneurysm prior to clot formation. In addition to tracking the total occlusion in the whole aneurysm, variations in clot progression in different regions of the aneurysm are assessed. Occlusion is monitored in six annular regions defined with radial thickness of R/6, where R is the aneurysm radius (R=2.865 x 10^{-3} m), and with ten horizontal slices with thickness in the vertical direction of D/10, where D is the aneurysm diameter (D=5.73 x 10^{-3} m).

4.3 Results

A total of twelve geometries are simulated in this study – six foam-filled aneurysms and six coil-filled aneurysms. The overall packing densities for the foam-filled aneurysms are approximately 4.5% and 3.8% for the unscaled and 1/2x-scaled foam cases, respectively. The coil-filled aneurysms have packing densities ranging from 23% to 25%. The total length – within the simulated 2D aneurysm slice – of the blood/biomaterial interfaces for the foam-treated aneurysms are approximately 0.085 m and 0.15 m for the unscaled and 1/2x-scaled foam cases. This length ranges from 0.065 m to 0.072 m for the coil-treated cases.

Simulation Geometry	Clot Initiation Time [s]	Clot Growth Rate [%/s]	Ultimate Occlusion [%]
Unscaled Foam:			
0-degree rotation	173.3	2.07	97.5
45-degree rotation	171.6	1.70	96.6
90-degree rotation	171.6	2.90	97.7
1/2x-scaled Foam:			
0-degree rotation	169.7	2.05	99.5
45-degree rotation	169.7	1.97	98.7
90-degree rotation	169.8	1.19	99.0
Coil-filled Aneurysms:			
Case #1	162.9	0.64	92.1
Case #2	163.9	0.68	84.7
Case #3	163.9	1.10	82.8
Case #4	163.9	1.13	88.7
Case #5	163.9	1.14	90.7
Case #6	163.9	0.71	94.4

Table 4.1: Clot growth results. Clot growth rate taken at 50% aneurysm occlusion and expressed as change in percent occlusion per second.

The medium-fidelity computational thrombus model predicts that in all aneurysms, clot first appears along foam strut or coil surfaces in areas of minimal flow. Clot formation in the foam-filled cases begins 169 to 173 seconds after the biochemical model is enabled and after 162 to 164 seconds in the coil-treated aneurysms (see Table 4.1). The clot progressions within each foam-treated and coil-treated aneurysm are shown in the figures in Appendix B which show the clot distribution at various time points for each case. Aneurysm occlusion – measured as the percentage of available post-treatment area filled with clot – is plotted as a function of time in Figures 4.3 and 4.4 for the foam-filled and coil-filled aneurysm simulations. After an initial phase where 5 to 10 percent occlusion is achieved in each aneurysm, rapid clot growth occurs marked by a nearly linear increase in occlusion over time which accounts for approximately 60 to 80 percent of clot growth.

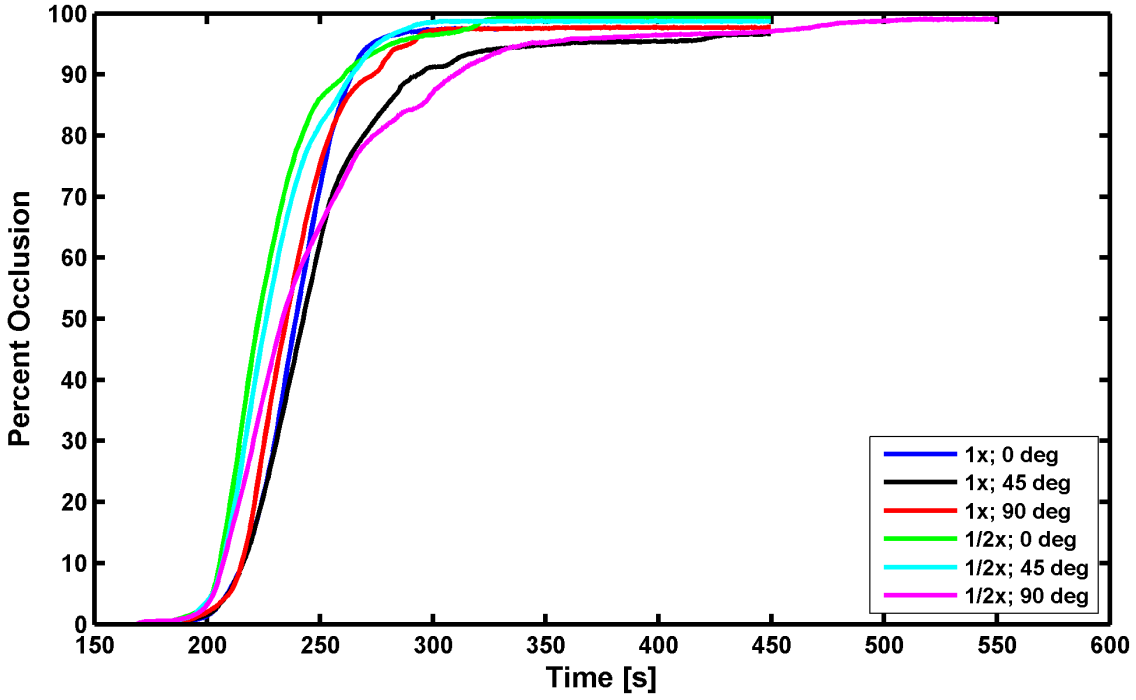

Figure 4.3: Occlusion as a function of time in the foam-filled aneurysms. Legend entries indicate foam scale (1x or 1/2x) and orientation (i.e., rotations of 0, 45, or 90 degrees).

To assess the speed of clot formation in this period of rapid clot generation, a linear least-squares regression fit is applied to the portion of the occlusion versus time curve that falls between 40 and 60 percent occlusion. The resulting slope is the clot growth rate which is listed for each aneurysm in Table 4.1. During this phase of linear clot generation, the occlusion within the foam-filled aneurysms increases by 1.19 to 2.07 percentage points per second (clot area increases by 2.9 x 10^{-7} to 5.0 x 10^{-7} m^2 per second), and occlusion within the coil-filled aneurysms increases at a rate of 0.64 to 1.14 percentage points per second (1.2 x 10^{-7} to 2.2 x 10^{-7} m^2 per second). The ultimate occlusion in each aneurysm is listed in Table 4.1 and the final clot distributions in each aneurysm are shown in Figure 4.5 (foam-treated aneurysms) and Figure 4.6 (coil-treated aneurysms). For the foam-treated aneurysms, the unscaled foam results in ultimate occlusions of 96.5% to 97.7%,

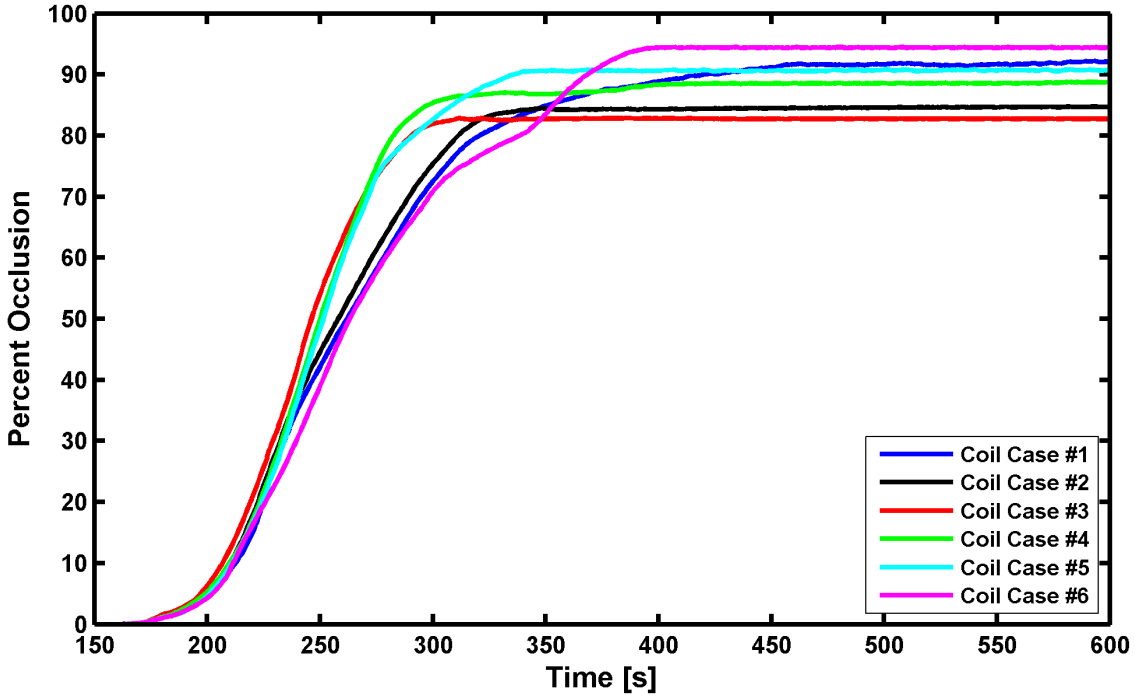

Figure 4.4: Occlusion as a function of time in the coil-filled aneurysms.

and the 1/2x-scaled foams result in ultimate occlusions between 98.7% and 99.5%. The ultimate occlusions range from 82.8% to 94.4% in the coil-filled aneurysms with large portions of the aneurysm neck remaining unclotted in five of the six cases.

Ultimate occlusions in six annular regions and ten horizontal slices within each aneurysm are also measured. Figures 4.7 and 4.8 summarize these values by showing the range of ultimate occlusions achieved by either the foam-treated or coil-treated aneurysms within each region. In the annular regions, all foam-filled aneurysms achieve 100% occlusion in all but the two outer-most rings (labeled R5 and R6 in Figure 4.7). In the first of those rings (R5), the foam-filled aneurysms reach at least 99.6% occlusion and the ultimate occlusions in the outer ring (R6) range between 87% and 98%. The two inner-most annular regions (R1 and R2) completely occlude in all coil-filled aneurysms. In the third ring (R3), two coil cases do not reach 100% occlusion – coil case #2 (95.5% occlusion) and coil case

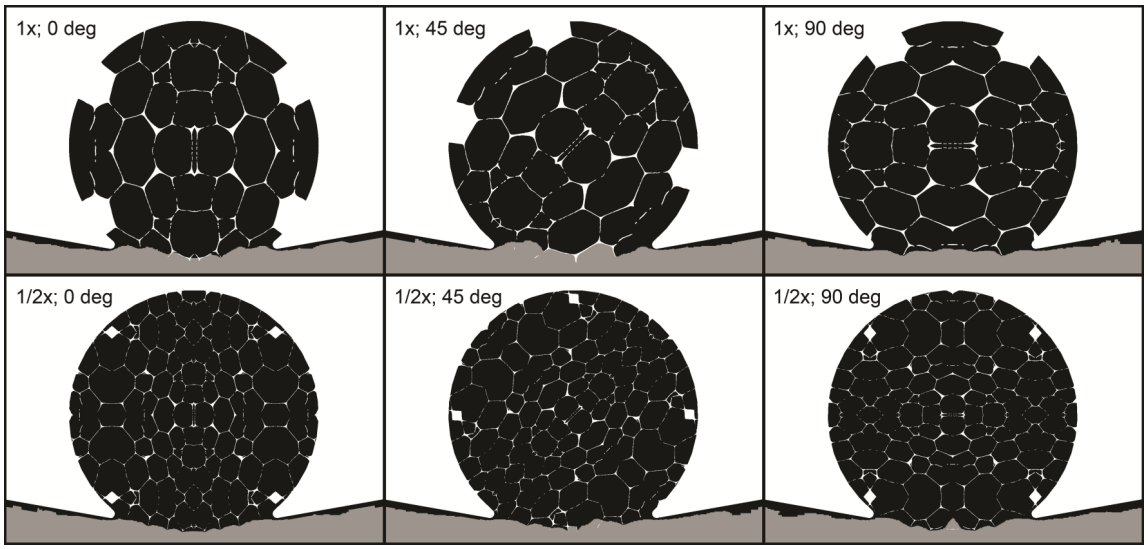

Figure 4.5: Final clot distributions in the aneurysms filled with foam. Labels in each image indicate foam scale (1x or 1/2x) and orientation (i.e., rotations of 0, 45, or 90 degrees). Black represents clotted blood.

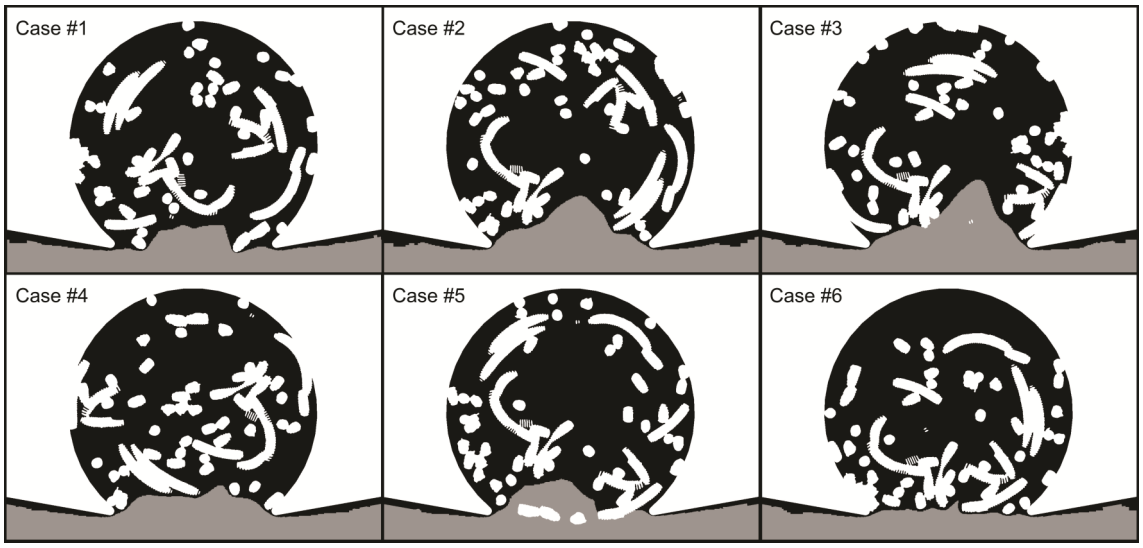

Figure 4.6: Final clot distributions in each of the six coil-filled aneurysm cases. Black represents clotted blood.

#3 (88.5%). In the last three rings, the ranges for the ultimate occlusions in the coil-filled aneurysms are 81.5% to 100% (only coil case #6 reaches 100%), 76% to 96.5%, and 77%

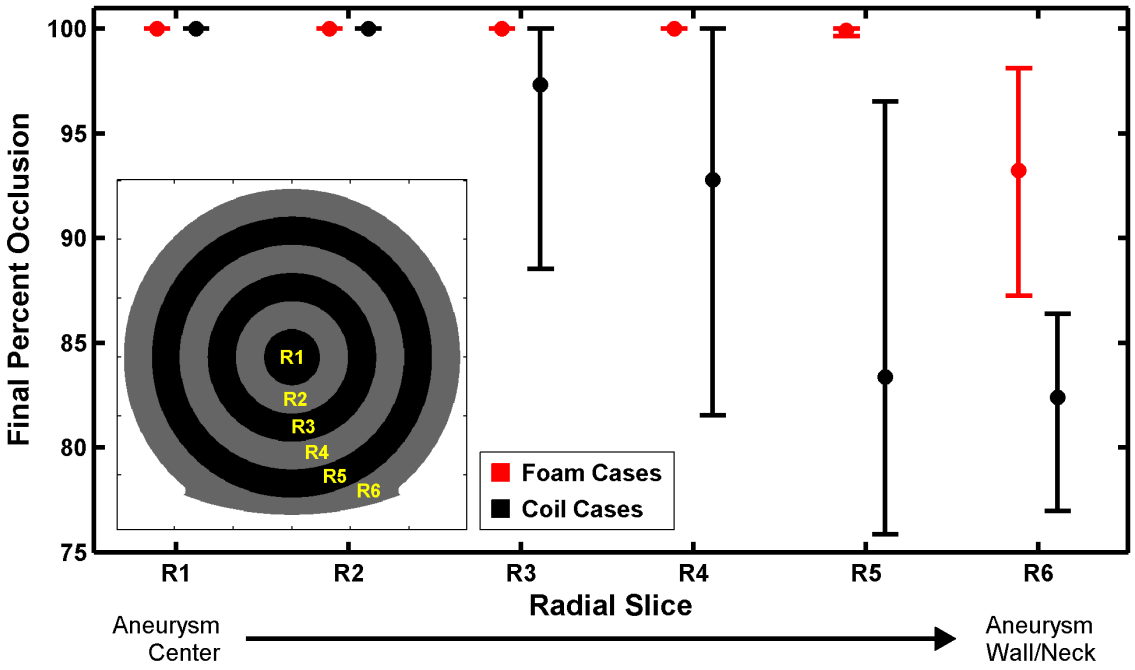

Figure 4.7: Occlusion achieved in each of the radial regions for the foam-filled (red) and coil-filled (black) aneurysms. The dots represent the average final occlusion achieved among the cases for a given region, and the bars represent the range between the least occluded and most occluded case for that region. The inset shows the empty aneurysm geometry with radial regions labeled.

to 86%. In the horizontal slices, the upper 80% of all foam-filled aneurysms and the upper 60% of all coil-filled aneurysms reach complete occlusion. In the lowest horizontal slice in the aneurysm neck (H1 in Figure 4.8), the final achieved occlusions are between 26% and 87% in the foam-filled aneurysms and less than 12% in all coil-filled aneurysms. The range of times required to reach 50% occlusion in each radial region for each aneurysm is shown in Figure 4.9. A similar summary is not given for the horizontal slices because some aneurysms fail to reach 50% occlusions in some of the horizontal regions.

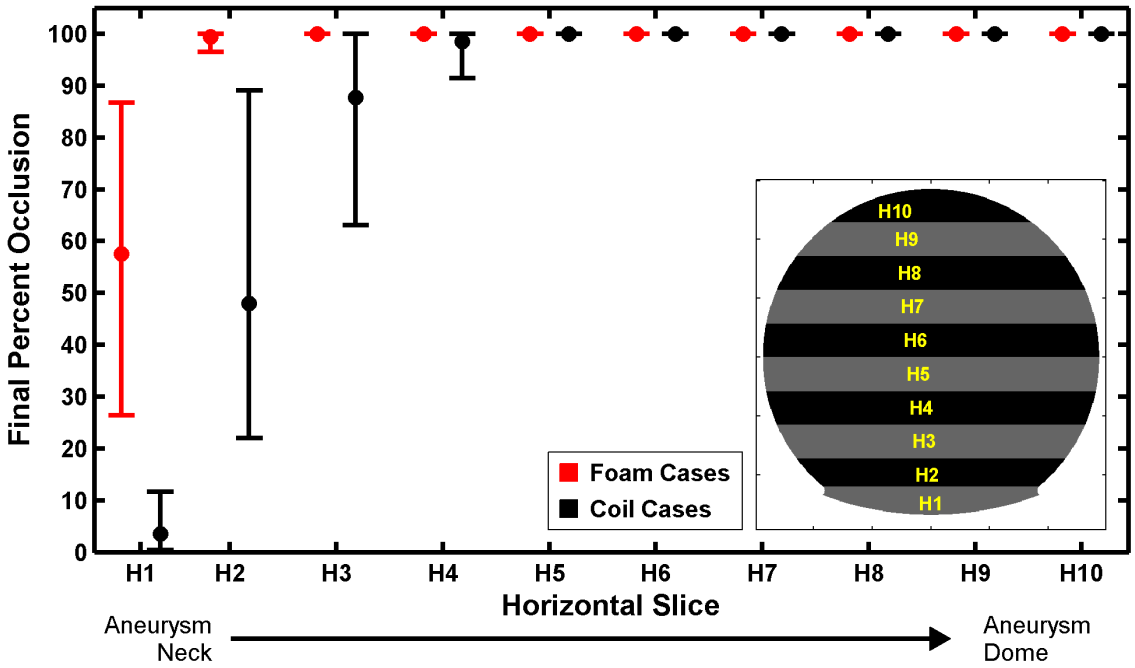

Figure 4.8: Occlusion achieved in each of the horizontal regions for the foam-filled (red) and coil-filled (black) aneurysms. The dots represent the average final occlusion achieved among the cases for a given region, and the bars represent the range between the least occluded and most occluded case for that region. The inset shows the empty aneurysm geometry with horizontal slices labeled.

4.4 Discussion

In this chapter, computational modeling is used to evaluate the clotting response of blood within aneurysms treated with shape memory polymer foams. The porous internal structure of these foams provides a scaffold for clot growth that leads to aneurysm occlusion and isolation from the parent artery.[48,68,100] A goal of the simulations conducted here is to evaluate if the clotting response varies with pore size, a foam parameter that can be tuned during the fabrication process.[62] By scaling the original foam geometry adapted from μ-CT imaging data, which has pores diameters of approximately 1 x 10^{-3} m, a smaller pore foam is generated with pore diameters of approximately 0.5 x 10^{-3} m.

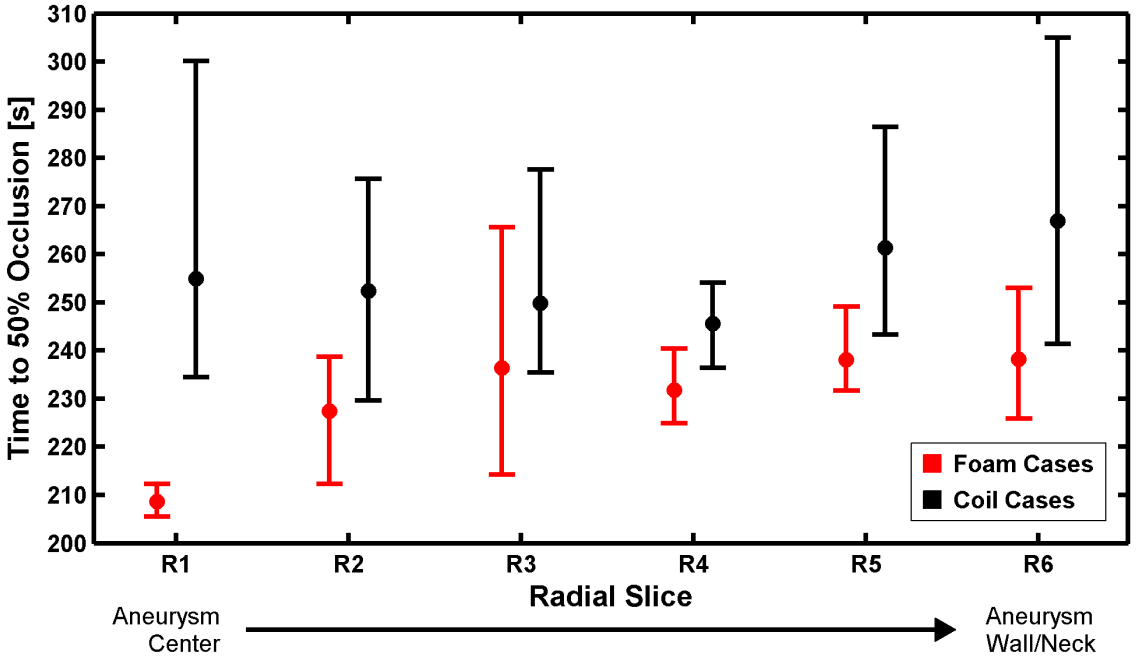

Figure 4.9: Summary of the time it takes to reach 50% occlusion in each radial region for the foam-filled (red) and coil-filled (black) aneurysms. The dots represent the average time to 50% occlusion among the cases for a given region, and the bars represent the range between the slowest and fastest cases to reach 50% occlusion for that region.

Further, both unscaled and scaled geometries are simulated in three orientations (rotations about the aneurysm center of 0, 45, and 90 degrees) to assess how the foam's anisotropic geometry and properties (e.g., permeability[85,101]) can impact the clot response when, clinically, foam orientation within the aneurysm cannot be controlled. To compare the performance of the shape memory polymer foam to commonly used aneurysm treatments, the clotting response in aneurysms filled with bare metal coils is also simulated. The simulated geometries have packing densities (23-25%) comparable to a reported average for rabbit-elastase aneurysms packed as densely as possible with platinum coils (22.0%),[77] and the coil distribution in each geometry is randomized to represent the random nature of coil placement during treatment.

In the foam-filled aneurysms, pore size did not have a significant effect on the rate of aneurysm occlusion; however, this rate did vary with foam orientation. Similarly, the different coil distributions produced varied occlusion rates in the coil-filled aneurysms, and in each, clot growth was slower than observed in the foam-filled aneurysms. In particular, most annular regions reached 50% occlusion earlier in the foam-filled aneurysms than in the coiled aneurysms, especially in the aneurysm core. The ultimate occlusion achieved within the foam-filled aneurysms showed little variation among the three orientations and only slightly greater occlusion in the smaller pore foams. In contrast, the coil-treated aneurysms showed a wide variation in the final achieved occlusion depending on the configuration of coils. In all foam and coil cases, incomplete filling in the aneurysm neck accounted for the failure to achieve 100% occlusion. Clinically, these residual necks or neck remnants may necessitate additional treatment or retreatment depending on size.[55] Potential neck remnants in the foam-treated aneurysms were small, extending at most a distance into the aneurysm equal to one tenth of the aneurysm diameter. However, the neck remnants present in most of the coil-filled aneurysms were larger, extending as deep as 40% of the aneurysm diameter, especially in aneurysms lacking dense coil packing in the aneurysm neck.

The presence of thrombus in the majority of the aneurysm sac with a residual unfilled neck remnant, as predicted for most of the simulated coil-filled aneurysms, is only supported by limited evidence in the literature. Gross and histological analysis of human intracranial aneurysms[10,41,69,120] and experimental bifurcation aneurysm models in animals[9,14,66,98,99,108,116] commonly reveal areas between coil loops throughout the aneurysm sac that contain no thrombus. These findings suggest that the amount of thrombus occlusion is potentially over-estimated for the simulated coil-filled aneurysms.

Several limitations are present in the computational approach used to predict clot formation in this study. These include a limited representation of the biochemistry in-

volved in clot formation that may neglect proteins and reactions key to the clotting process, such as factor XIII which crosslinks fibrin monomers to stabilize the clot and, if incorporated into the model, could prevent the predicted unwanted spread of clot out of the aneurysm. Also, the expressions and parameters defining the flux terms that simulate initiation of the clotting cascade, via factor XII activation along biomaterial surfaces, treat all materials equally. Golas et al. demonstrated that the rate of factor XII activation along a biomaterial surface varies based on that surface's hydrophobicity.[38] Thus, it is likely that the polymer foam surfaces and the metal coil surfaces would elicit different clot initiating effects *in vivo* that may impact the overall clotting response. Further, it is assumed that the simulated post-treatment environment is absent of heparin which would inhibit the clotting cascades to some degree. Thus, the model does not accurately represent the clinical environment wherein heparin is administered to prevent clotting on guidewires, catheters, and other blood contacting instruments during the treatment procedure. However, only absolute clotting rates are assumed to be affected and not the relative results among the various cases. To reduce computational demand, 2D geometries were modeled as opposed to simulations of 3D aneurysms which would have required several months each to complete. Simulating only a cross-section of the treated aneurysm creates different flow patterns within the aneurysm that may be unrealistic. Further, the ratio of the thrombogenic boundary size to the amount of blood in the aneurysm is very different for the 2D geometry and the predicted impact of surface-mediated XII activation may not be accurate. Therefore, the predicted clot growth patterns within the 2D aneurysm geometries may differ from the clotting response in actual treated aneurysms. Finally, the model complexity, with over 50 experimentally-obtained model parameters, leads to many sources of uncertainty in the simulation results. Unfortunately, suitable experimental data for model validation is not readily available and is not easy to generate given challenges in replicating the *in vivo* environment and limitations in non-destructive imaging techniques. As

capabilities improve, future efforts should aim to collect such data to aid in model tuning and validation.

4.5 Conclusion

Overall, each foam-filled aneurysm had similar clotting responses irrespective of pore size or foam orientation. The coil-filled aneurysms exhibited clotting responses highly dependent on coil distribution, both in occlusion rate and final occlusion. Furthermore, occlusion was faster and more complete in all foam-filled aneurysms as compared to the coil-filled aneurysms which often exhibited potentially vulnerable residual necks. These favorable results were achieved in the foam-filled aneurysms despite the coil-filled aneurysms having 5-6 times greater packing densities. While shortcomings in the modeling approach and the small number of cases tested limit the strength of the results of this work, these simulations suggest that foams may provide more predictable outcomes (i.e., complete and rapid filling), regardless of pore size or orientation, compared to the coils which can produce vastly different, unpredictable, and potentially clinically unstable outcomes depending on the random configuration of coils within the aneurysm sac.

5. SUMMARY AND CONCLUSIONS

5.1 Summary

A medium-fidelity thrombus generation model was developed and described in this dissertation which is based on the model presented by LaCriox and Anand. New boundary flux terms were added to model the biochemical interactions between blood and biomaterial surfaces enabling simulation of device-induced thrombosis. This biochemical framework defining the clotting cascades was incorporated into a commercial-grade CFD package, STAR-CCM+, enabling the simulation of clot formation in complex geometries under physiological blood flow conditions. The model developed in this work is an advancement of current models described in the literature. No other models, at the time of writing this dissertation, that couple biochemical and hemodynamic phenomena and provide transient predictions of thrombus development are suitable for large-scale simulations of device-induced thrombosis in complex geometries exposed to physiological flow regimes.

The medium-fidelity model was demonstrated within a 2D idealized aneurysm filled with shape memory polymer (SMP) foam. The predicted clotting within the foam-treated aneurysm resulted in near-complete aneurysm occlusion within 5-6 minutes. Low-fidelity modeling of the same foam-filled aneurysm geometry highlighted the advantages of the medium-fidelity model over common simulation methods that offer predictions based solely on time-averaged flow features. A major shortcoming of low-fidelity approaches, which is overcome by the model developed in this work, is that the predicted clot distributions do not represent actual time points in the clot generation histories. The predictions do not show initial clot locations, nor do they represent long term or final clot

distributions, despite being based on long term residence time measurements. This confusion is avoided by the medium-fidelity model which elucidates the transient clot growth.

Using the medium-fidelity model, the clotting response within aneurysms treated with either bare metal coils or SMP foam was evaluated. Bare metal coils are the most commonly used embolic material for endovascular aneurysm treatment; however, their use often leads to suboptimal clinical outcomes. SMP foam is an alternative embolic material designed to improve treatment results.[68,100] Simulations of various coil-filled and foam-filled aneurysms suggest that SMP foam may elicit more predictable and clinically favorable clotting responses than the bare metal coils. The coil-filled aneurysms had clotting responses that were highly dependent on the distribution of coils within the aneurysm sac and many of the predicted thrombus distributions included large unfilled neck remnants which could lead to clinical complications such as aneurysm regrowth. In contrast, all foam-filled aneurysms, regardless of foam orientation or pore size, had near-complete (>97%) occlusion and minimal neck remnants that would likely be clinically insignificant.

In this dissertation work, a computational thrombus generation model was developed to simulate device-induced thrombosis. The model was shown to provide valuable information that commonly used low-fidelity models cannot. Finally, the model was used to evaluate two aneurysm treatment methods. This study demonstrates the model's potential as an engineering tool that can aid in device optimization.

5.2 Model Challenges and Future Work

The model described in this dissertation, while an improvement over current models, should be considered a precursor to a more complete and more accurate model of the complex processes that contribute to thrombus formation. The present model tracks only 28 biochemicals along with some of the interactions that take place among them. The chosen set of proteins and reactions are assumed to represent the most salient features of

the clotting cascades. However, many more proteins and reactions are involved in clot formation and could be included in the computational model. In fact, models described by Kuharsky et al.[58] and Luan et al.[65] include 56 and 92 constituents, respectively. Future model iterations should aim to test which of the many proteins in the blood and which biochemical reactions have a significant impact on clot generation and which can be neglected to give the most physiologically relevant representation of the biochemistry of clot formation without creating unnecessary computational demand.

One specific blood protein, neglected in the current model, that likely has a significant impact on clot growth and development is fibrinoligase (factor XIIIa). As fibrin monomers are produced as a result of the clotting cascades, XIIIa crosslinks those monomers, thereby fixing them in place and increasing the structural integrity of the formed clot.[64] The lack of XIIIa (and its precursor, factor XIII) in the model is likely partially responsible for the predicted spread of thrombus outside of the aneurysms in all simulations. A lack of significant fibrin production in the branching vessels suggests that clot growth does not occur outside the aneurysm sac. Rather, due to very large concentration gradients across the thrombus/blood interface, fibrin is advected in large amounts from existing clot in the aneurysm, leading to the appearance of thrombus accumulation along the artery walls. *In vivo*, XIIIa would crosslink these fibrin monomers and prevent them from freely leaving the clot. This function could be incorporated into the model by tracking the concentrations of XIII and XIIIa along with an additional crosslinked form of fibrin. Given the appropriate reaction kinetics and rate constants, XIIIa would convert fibrin into the crosslinked form, which would not be subjected to mass transport. The sum of the concentrations of both forms of fibrin would be compared to the fibrin concentration threshold (350 nM) to determine which computation elements contain thrombus. The result would be that fibrin generation, not fibrin mass transport, would be the major driver of thrombus growth predicted by the model.

Heparin, while not naturally present in the blood, is another chemical that can significantly impact blood biochemistry. It is clinically administered during endovascular procedures to inhibit unwanted clotting. Once administered, the heparin molecules interact with ATIII, thereby accelerating, in a dose-dependent manner, ATIII's inhibition of several key factors of the clotting cascade.[92,115,130] For simplicity, the current model assumes heparin is not present in the blood. This produces a simulated environment, where ATIII activity is minimal, that is not representative of the *in vivo* environment present during treatment. Future models could track the concentrations of heparin in the domain resulting from a simulated infusion at the domain inlet. Heparin concentrations could then be incorporated into the reaction kinetics (i.e., the reactive source terms) for ATIII's inhibition of its various targets. This would likely result in slower thrombus generation and would partially restrict clotting to locations near thrombogenic stimuli (e.g., biomaterial surfaces).

The main thrombogenic stimuli for device-induced thrombosis is the negatively charged biomaterial surface of the implanted device. When blood contacts such surfaces, factor XII is activated, thereby initiating the clotting cascade.[127] The rate of XII activation is dependent on the surface chemistry of the material in contact with the blood.[38,39,136] However, in its current form, the thrombus model does not account for the surface properties of specific devices or materials. Rather, all surfaces stimulate equivalent XII activation based on reaction kinetics derived for XII activation in a solution of dextran sulfate.[122] While the dextran sulfate molecules approximate negatively charged surfaces to model surface-dependent XII activation, these kinetics do not necessarily apply to the foam or coil surfaces examined in this work. Further, the polymeric foam and bare metal coils likely stimulate XII activation at different rates. The current model ignores these differences caused by differing material properties. Therefore, efforts should be made to characterize the response to various materials so that the rate constants governing surface-

mediated XII activation can be appropriately scaled. This would allow for more accurate device comparisons as surface chemistry may have a significant impact on the clotting response.

In addition to biomaterial surfaces, the other major stimulus for clot formation is injured endothelium which can initiate the extrinsic clotting pathway. This phenomenon may have a significant effect on the clot formation during endovascular treatments given that endothelial cells can easily be injured if an implanted device or the delivery catheter contacts the vessel wall. Implanting metal coils or SMP foams within the aneurysm sac may create several areas of thrombogenic tissue injury along the aneurysm wall. This potential mode of clot initiation is neglected by the current model. The model proposed by LaCroix and Anand – which forms the foundation for the model described in this dissertation – does address tissue-induced clotting using boundary flux terms to model factor IX and factor X activation that occurs when blood interacts with exposed tissue factor on injured endothelial cells. However, these flux terms were removed during early stages of model development because clotting via the extrinsic pathway was very rapid and overwhelmed any clotting resulting from intrinsic pathway activation. Given that several aspects of the model have since been modified, and the potential significance of treatment-induced tissue injury, the flux terms defining extrinsic pathway activation should be reevaluated. If this functionality can be restored, the predicted patterns of clot growth may be significantly different. In particular, clot growth near the aneurysm wall may occur simultaneously with clot growth along the implanted device's surface.

Along with the biochemicals that participate in clot generation, platelets are also an integral part of the clotting process. First, as clots develop, platelets get enmeshed in the fibrin network and contribute to the clot's overall structure and mechanical properties. Platelets also regulate portions of the clotting cascades as the tenase and prothrombinase complexes must form on the phospholipid membranes of activated platelets.[75,83,95] The

current model does not track individual platelets and their contributions to thrombus morphology because the computational demand would exceed the available computational resources. Further, the model simplifies the biochemical effects of platelets by assuming that activated platelets are present throughout the domain in sufficient numbers as to not rate-limit the creation of tenase or prothrombinase. A more rigorous model would differentiate between active and resting platelets and account for how platelet activation is necessary for the progression of the clotting cascades. Platelet activation would be catalyzed by thrombin and ADP released by already activated platelets. Early in the clotting response, when little thrombin is present, activation would occur via hemodynamic phenomena such as abnormally high shear rates. An early model description by Anand et al. proposed tracking the concentrations of resting and activated platelets.[2] The latter of which was factored into the rates of tenase and prothrombinase production. Conversion from resting to activated states was achieved using a quantity that tracks the amount of time a platelet is exposed to excess shear. Once this quantity reaches a certain threshold, resting platelets become activated. If a similar approach could be implemented within the current model framework, the predicted clotting response would likely be affected. Flow perturbations created by device geometry would play a greater role in clot initiation as areas of high shears, in addition to biochemical thrombogenic stimuli, would be required.

Another limitation of the current model is in the handling of the mechanical properties of thrombus. The proposed model treats clotted regions as a homogenous fluid exhibiting a shear thinning viscosity. However, blood clots exhibit complex time-dependent and shear-dependent mechanical behaviors, including creep[36,81] and stress relaxation.[52] Furthermore, a clot's mechanical properties are greatly influenced by the composition of the fibrin matrix even though fibrin accounts for less than 1% by volume of a clot's structure.[13,31] While a complete constitutive model describing the mechanical properties of thrombus would greatly increase the accuracy of this work, coupling a solid mechanics

model to the fluid mechanics model employed herein would only add to the already high level of complexity and computational demand.

In its current form, the biochemical thrombus model is composed of 28 governing equations that include approximately 50 experimentally-derived parameters that require numerous assumptions to be made. Thus, whether in its current form or in an adapted state, model uncertainty is high. This highlights the need for model validation to help assess model accuracy and to help determine which modifications improve or degrade the model's predications of *in vivo* clotting dynamics. Unfortunately, generating sufficient experimental data for comparison is a difficult task. Ideal data sets would include thrombus distribution measurements taken at several time points over the course of clot development. Most imaging modalities to non-destructively observe *in vivo* blood flow, such as MRI, CT-angiography, and doppler ultrasound, do not have adequate 3D spatial resolution or temporal resolution to be useful for validation. *In vitro* testing is an alternative, but these experiments also pose challenges and limitations. As with *in vivo* testing, monitoring clot geometry over time is difficult. Also, *in vitro* experiments do not completely represent the physiological *in vivo* environment. Nonetheless, given the model's complexity, obtaining experimental validation data should be a priority for future work.

The simulations in this dissertation were limited by the available computational resources. Because of the large number of model equations, required spatial and temporal resolutions, and the larges regions of interest and long timescales of interest, clotting simulations have the potential to be extremely computationally extensive. To reduce computational cost, simulations in this work were conducted in 2D. This forces unrealistic assumptions that likely impact the accuracy and relevance of the predicted results. Specifically, simulating in 2D forces the assumption that the velocity gradients are all zero in the out-of-plane direction. Restricting flow to a single plane, artificially creates more areas of flow stagnation. Furthermore, the size of the boundaries that interact with blood in the 2D

simulations (i.e., coil and foam strut surfaces), relative to the domain, is likely very different than the relationship between the surface areas of those boundaries and the volume of blood in the 3D aneurysm. Thus, 2D simulations may over or under estimate the impact of intrinsic pathway activation on device-induced thrombosis. Simulations in the future, when computational capabilities are improved, should move to 3D representations of the treated aneurysm geometry. Also, it would be of interest to run simulations out to longer end timepoints to capture potential fibrinolysis. As a long-term goal for clot modeling, the inclusion of particle tracking for red blood cells – which influence blood rheology – and platelets – which influence the clotting cascades and structural properties of the clot – could be incorporated into the computational model to make it more physiologically representative and potentially more accurate.

As demonstrated in this work, the computational thrombus model can be applied to evaluate aneurysm treatments. In the future, the model could to be applied to further study foam-based embolic devices for aneurysm treatment. This would include a more comprehensive study of the effects of foam pore size on the clotting response. Also, foam reticulation – a process of removing the membranes separating individual foam pores – could be evaluated to determine if removing membranes, and thereby reducing foam surface area, significantly alters the clotting properties of the foam. Improved comparisons with bare metal coils could also be made with more rigorous simulations of coil-treated aneurysms. For instance, more realistic coil geometries should be considered along with distributions with varied packing densities. Additionally, other foam-based devices treatment devices can be evaluated such as foam-over-wire designs,[16] which are a more likely embodiment for clinical use considering that bulk foams are too large and stiff to be delivered through catheters small enough to reach the neurovasculature. Also, foam-based embolic devices for treatment beyond intracranial aneurysms can be studied. These included peripheral embolic devices,[62] devices for treating congenital heart defects,[131] as

well as hemostatic sponge applications.[63] In addition to applications where thrombosis is desired, cardiovascular applications wherein thrombus formation is considered detrimental (e.g., heart valves, stents, and ventricular assist devices) can also be simulated. Whether future embodiments of the computational clotting model described in this work are used to study applications where clot formation is positive or negative, the results will inform device design and potentially lead to improved clinical outcomes.

REFERENCES

[1] Ahmad, S. S., R. Rawala-Sheikh, and P. N. Walsh. Comparative interactions of factor IX and factor IXa with human platelets. *Journal of Biological Chemistry* 264:3244–3251, 1989.

[2] Anand, M., K. Rajagopal, and K. R. Rajagopal. A model incorporating some of the mechanical and biochemical factors underlying clot formation and dissolution in flowing blood. *Journal of Theoretical Medicine* 5:183–218, 2003.

[3] Anand, M., K. Rajagopal, and K. R. Rajagopal. A model for the formation and lysis of blood clots. *Pathophysiology of Haemostasis and Thrombosis* 34:109–120, 2005.

[4] Anand, M., K. Rajagopal, and K. R. Rajagopal. A viscoelastic fluid model for describing the mechanics of a coarse ligated plasma clot. *Theoretical and Computational Fluid Dynamics* 20:239–250, 2006.

[5] Anand, M., K. Rajagopal, and K. R. Rajagopal. A model for the formation, growth, and lysis of clots in quiescent plasma. A comparison between the effects of antithrombin III deficiency and protein C deficiency. *Journal of Theoretical Biology* 253:725–738, 2008.

[6] Badimon, L., J. J. Badimon, A. Galvez, J. H. Chesebro, and V. Fuster. Influence of arterial damage and wall shear rate on platelet deposition. Ex vivo study in a swine model. *Arteriosclerosis, Thrombosis, and Vascular Biology* 6:312–320, 1986.

[7] Ballyk, P. D., D. A. Steinman, and C. R. Ethier. Simulation of non-Newtonian blood flow in an end-to-side anastomosis. *Biorheology* 31:565–586, 1994.

[8] Banerjee, A. D., L. Guimaraens, and H. Cuellar. Asymptomatic delayed coil migration from an intracranial aneurysm: A case report. *Case Reports in Vascular Medicine*

2011:2, 2011.

[9] Bavinzski, G., B. Richling, B. R. Binder, A. Gruber, V. Talazoglu, W. Dietrich, I. Schwendtenwein, and H. Plenk. Histopathological findings in experimental aneurysms embolized with conventional and thrombogenic/antithrombolytic Guglielmi coils. *Minimally Invasive Neurosurgery* 42:167–174, 1999.

[10] Bavinzski, G., V. Talazoglu, M. Killer, B. Richling, A. Gruber, C. E. Gross, and H. Plenk. Gross and microscopic histopathological findings in aneurysms of the human brain treated with Guglielmi detachable coils. *Journal of Neurosurgery* 91:284–293, 1999.

[11] Bederson, J. B., E. S. Connolly, H. H. Batjer, R. G. Dacey, J. E. Dion, M. N. Diringer, J. E. Duldner, R. E. Harbaugh, A. B. Patel, and R. H. Rosenwasser. Guidelines for the management of aneurysmal subarachnoid hemorrhage. A statement for healthcare professionals from a special writing group of the Stroke Council, American Heart Association. *Stroke* 40:994–1025, 2009.

[12] Bernsdorf, J., S. E. Harrison, S. M. Smith, P. V. Lawford, and D. R. Hose. Applying the lattice Boltzmann technique to biofluids: A novel approach to simulate blood coagulation. *Computers and Mathematics with Applications* 55:1408–1414, 2008.

[13] Blombäck, B. and M. Okada. Fibrin gel structure and clotting time. *Thrombosis Research* 25:51–70, 1982.

[14] Böcher-Schwarz, H. G., K. Ringel, J. Bohl, R. Filippi, O. Kempski, and A. Perneczky. Histological findings in coil-packed experimental aneurysms 3 months after embolization. *Neurosurgery* 50:379–385, 2002.

[15] Bodnár, T. and A. Sequeira. Numerical simulation of the coagulation dynamics of blood. *Computational and Mathematical Methods in Medicine* 9:83–104, 2008.

[16] Boyle, A. J., T. L. Landsman, M. A. Wierzbicki, L. D. Nash, W. Hwang, M. W. Miller, E. Tuzun, S. M. Hasan, and D. J. Maitland. *In vitro* and *in vivo* evaluation of a shape memory polymer foam-over-wire embolization device delivered in saccular aneurysm models. *Journal of Biomedical Materials Research, Part B: Applied Biomaterials* 104B:1407–1415, 2016.

[17] Cabanlit, M., D. Maitland, T. Wilson, S. Simon, T. Wun, M. E. Gershwin, and J. Van de Water. Polyurethane shape-memory polymers demonstrate functional biocompatibility in vitro. *Macromolecular Bioscience* 7:48–55, 2007.

[18] Cáceres-Lóriga, F. M., H. Pérez-López, J. Santos-Gracia, and K. Morlans-Hernandez. Prosthetic heart valve thrombosis: Pathogenesis, diagnosis and management. *International Journal of Cardiology* 110:1–6, 2006.

[19] Citarella, F., W. A. Wuillemin, Y. T. P. Lubbers, and C. E. Hack. Initiation of contact system activation in plasma is dependent on factor XII autoactivation and not on enhanced susceptibility of factor XII for kallikrein cleavage. *British Journal of Haematology* 99:197–205, 1997.

[20] Cito, S., M. D. Mazzeo, and L. Badimon. A review of macroscopic thrombus modeling methods. *Thrombosis Research* 131:116–124, 2013.

[21] Corbett, S. C., A. Ajdari, A. U. Coskun, and H. N-Hashemi. In vitro and computational thrombosis on artificial surfaces with shear stress. *Artificial Organs* 34:561–569, 2010.

[22] Crobeddu, E., G. Lanzino, D. F. Kallmes, and H. J. Cloft. Review of 2 decades of aneurysm-recurrence literature, part 1: reducing recurrence after endovascular coiling. *American Journal of Neuroradiology* 34:266–270, 2013.

[23] Cutlip, D. E., D. S. Baim, K. K. L. Ho, J. J. Popma, A. J. Lansky, D. J. Cohen, J. P. Carrozza, M. S. Chauhan, O. Rodriguez, and R. E. Kuntz. Stent thrombosis in the

modern era. A pooled analysis of multicenter coronary stent clinical trials. *Circulation* 103:1967–1971, 2001.

[24] De Cristofaro, R. and V. De Filippis. Interaction of the 268-282 region of glycoprotein Ibα with the heparin-binding site of thrombin inhibits the enzyme activation of factor VIII. *Biochemical Journal* 373:593–601, 2003.

[25] de la Monte, S. M., G. W. Moore, M. A. Monk, and G. M. Hutchins. Risk factors for the development and rupture of intracranial berry aneurysms. *The American Journal of Medicine* 78:957–964, 1985.

[26] Demirdžić, I., Ž. Lilek, and M. Perić. A collocated finite volume method for predicting flows at all speeds. *International Journal for Numerical Methods in Fluids* 16:1029–1050, 1993.

[27] Diamond, S. L. and S. Anand. Inner clot diffusion and permeation during fibrinolysis. *Biophysical Journal* 65:2622–2643, 1993.

[28] Doerfler, A., I. Wanke, T. Egelhof, U. Dietrich, S. Asgari, D. Stolke, and M. Forsting. Aneurysmal rupture during embolization with Guglielmi detachable coils: Causes, management, and outcome. *American Journal of Neuroradiology* 22:1825–1832, 2001.

[29] Evans, P. A., K. Hawkins, M. Lawrence, R. L. Williams, M. S. Barrow, N. Thirumalai, and P. R. Williams. Rheometry and associated techniques for blood coagulation studies. *Medical Engineering & Physics* 30:671–679, 2008.

[30] Ferns, S. P., M. E. S. Sprengers, W. J. van Rooij, G. J. E. Rinkel, J. C. van Rijn, S. Bipat, M. Sluzewski, and C. B. L. M. Majoie. Coiling of intracranial aneurysms: A systematic review on initial occlusion and reopening and retreatment rates. *Stroke* 40:e523–e529, 2009.

[31] Ferry, J. D. and P. R. Morrison. Preparation and properties of serum and plasma proteins. VIII. The conversion of human fibrinogen to fibrin under various conditions. *Journal of the American Chemical Society* 69:388–400, 1947.

[32] Freyssinet, J. M., F. Toti-Orfanoudakis, C. Ravanat, L. Grunebaum, J. Gauchy, J. P. Cazenave, and M. L. Wiesel. The catalytic role of anionic phospholipids in the activation of protein C by factor Xa and expression of its anticoagulant function in human plasma. *Blood Coagulation & Fibrinolysis* 2:691–698, 1991.

[33] Friedrich, P. and A. J. Reininger. Occlusive thrombus formation on indwelling catheters: in vitro investigation and computational analysis. *Thrombosis and Haemostasis* 73:66–72, 1995.

[34] Gaffney, P. J. and A. N. Whitaker. Fibrin crosslinks and lysis rates. *Thrombosis Research* 14:85–94, 1979.

[35] Gailani, D. and G. J. Broze. Factor XI activation in a revised model of blood coagulation. *Science* 253:909–912, 1991.

[36] Gerth, C., W. W. Roberts, and J. D. Ferry. Rheology of fibrin clots. II. Linear viscoelastic behavior in shear creep. *Biophysical Chemistry* 2:208–217, 1974.

[37] Geyik, S., O. Ertugrul, K. Yavuz, P. Geyik, I. Saatci, and H. S. Cekirge. Comparison of bioactive coils and bare platinum coils for treatment of intracranial aneurysms: a matched-pair analysis: Clinical article. *Journal of Neurosurgery* 112:709–713, 2010.

[38] Golas, A., P. Parhi, Z. O. Dimachkie, C. A. Siedlecki, and E. A. Vogler. Surface-energy dependent contact activation of blood factor XII. *Biomaterials* 31:1068–1079, 2010.

[39] Golas, A., C. H. J. Yeh, H. Pitakjakpipop, C. A. Siedlecki, and E. A. Vogler. A comparison of blood factor XII autoactivation in buffer, protein cocktail, serum, and plasma solutions. *Biomaterials* 34:607–620, 2013.

[40] Gomez, K. and J. H. McVey. Normal Haemostasis. In: *Postgraduate Haematology*, edited by A. V. Hoffbrand, D. R. Higgs, D. M. Keeling, and A. B. Mehta, Oxford: John Wiley & Sons, Ltd, 2016, pp. 676–698.

[41] Groden, C., C. Hagel, G. Delling, and H. Zeumer. Histological findings in ruptured aneurysms treated with GDCs: six examples at varying times after treatment. *American Journal of Neuroradiology* 24:579–584, 2003.

[42] Guglielmi, G., C. Ji, T. F. Massoud, A. Kurata, S. P. Lownie, F. Viñuela, and J. Robert. Experimental saccular aneurysms. II. A new model in swine. *Neuroradiology* 36:547–550, 1994.

[43] Guglielmi, G., F. Viñuela, I. Sepetka, and V. Macellari. Electrothrombosis of saccular aneurysms via endovascular approach. Part 1: Electrochemical basis, technique, and experimental results. *Journal of Neurosurgery* 75:1–7, 1991.

[44] Hampikian, J. M., B. C. Heaton, F. C. Tong, Z. Zhang, and C. P. Wong. Mechanical and radiographic properties of a shape memory polymer composite for intracranial aneurysm coils. *Materials Science and Engineering C* 26:1373–1379, 2006.

[45] Harrison, S. E., S. M. Smith, J. Bernsdorf, D. R. Hose, and P. V. Lawford. Application and validation of the lattice Boltzmann method for modelling flow-related clotting. *Journal of Biomechanics* 40:3023–3028, 2007.

[46] Hearon, K., P. Singhal, J. Horn, W. Small IV, C. Olsovsky, K. C. Maitland, T. S. Wilson, and D. J. Maitland. Porous shape-memory polymers. *Polymer Reviews* 53:41–75, 2013.

[47] Heeb, M. J., R. Bischoff, M. Courtney, and J. H. Griffin. Inhibition of activated protein C by recombinant α_1-antitrypsin variants with substitution of arginine or leucine for methionine[358]. *Journal of Biological Chemistry* 265:2365–2369, 1990.

[48] Horn, J., W. Hwang, S. L. Jessen, B. K. Keller, M. W. Miller, E. Tuzun, J. Hartman, F. J. Clubb, and D. J. Maitland. Comparison of shape memory polymer foam versus bare metal coil treatments in an *in vivo* porcine sidewall aneurysm model. *Journal of Biomedical Materials Research B: Applied Biomaterials* 105:1892–1905, 2017.

[49] Humphrey, J. D. and P. B. Canham. Structure, mechanical properties, and mechanics of intracranial saccular aneurysms. *Journal of Elasticity* 61:49–81, 2000.

[50] Hwang, W., B. L. Volk, F. Akberali, P. Singhal, J. C. Criscione, and D. J. Maitland. Estimation of aneurysm wall stresses created by treatment with a shape memory polymer foam device. *Biomechanics and Modeling in Mechanobiology* 11:715–729, 2012.

[51] Ingebrigtsen, T., M. K. Morgan, K. Faulder, L. Ingebrigtsen, T. Sparr, and H. Schirmer. Bifurcation geometry and the presence of cerebral artery aneurysms. *Journal of Neurosurgery* 101:108–113, 2004.

[52] Janmey, P. A., E. J. Amis, and J. D. Ferry. Rheology of fibrin clots. VI. Stress relaxation, creep, and differential dynamic modulus of fine clots in large shearing deformations. *Journal of Rheology* 27:135–153, 1983.

[53] Kaplan, A. P., M. Silverberg, J. T. Dunn, and G. Miller. Mechanisms for Hageman factor activation and role of HMW kininogen as a coagulation cofactor. *Annals of the New York Academy of Sciences* 370:253–260, 1981.

[54] Kato, T., T. Indo, E. Yoshida, Y. Iwasaki, M. Sone, and G. Sobue. Contrast-enhanced 2D cine phase MR angiography for measurement of basilar artery blood flow in posterior circulation ischemia. *American Journal of Neuroradiology* 23:1346–1351, 2002.

[55] Kole, M. K., D. M. Pelz, P. Kalapos, D. H. Lee, I. B. Gulka, and S. P. Lownie. Endovascular coil embolization of intracranial aneurysms: important factors related to rates and outcomes of incomplete occlusion. *Journal of Neurosurgery* 102:607–615, 2005.

[56] Kolev, K., I. Léránt, K. Tenekejiev, and R. Machovich. Regulation of fibrinolytic activity of neutrophil leukocyte elastase, plasmin, and miniplasmin by plasma protease inhibitors. *Journal of Biological Chemistry* 269:17030–17034, 1994.

[57] Krishnaswamy, S., W. R. Church, M. E. Nesheim, and K. G. Mann. Activation of human prothrombin by human prothrombinase. Influence of factor Va on the reaction mechanism. *Journal of Biological Chemistry* 262:3291–3299, 1987.

[58] Kuharsky, A. L. and A. L. Fogelson. Surface-mediated control of blood coagulation: The role of binding site densities and platelet deposition. *Biophysical Journal* 80:1050–1074, 2001.

[59] Kumar, V., A. K. Abbas, N. Fausto, and R. N. Mitchell. *Robbins Basic Pathology*. Philadelphia: Saunders/Elsevier, 2007.

[60] Kwan, E. S. K., C. B. Heilman, W. A. Shucart, and R. P. Klucznik. Enlargement of basilar artery aneurysms following balloon occlusion water-hammer effect. *Journal of Neurosurgery* 75:963–968, 1991.

[61] LaCroix, D. E. and M. Anand. A model for the formation, growth, and dissolution of clots in vitro. Effect of the intrinsic pathway on antithrombin III deficiency and protein C deficiency. *International Journal of Advances in Engineering Sciences and Applied Mathematics* 3:93–105, 2011.

[62] Landsman, T. L., R. L. Bush, A. Glowczwski, J. Horn, S. L. Jessen, E. Ungchusri, K. Diguette, H. R. Smith, S. M. Hasan, D. Nash, F. J. Clubb, and D. J. Maitland. Design and verification of a shape memory polymer peripheral occlusion device. *Journal of the Mechanical Behavior of Biomedical Materials* 63:195–206, 2016.

[63] Landsman, T. L., T. Touchet, S. M. Hasan, C. Smith, B. Russell, J. Rivera, D. J. Maitland, and E. Cosgriff-Hernandez. A shape memory foam composite with enhanced fluid

uptake and bactericidal properties as a hemostatic agent. *Acta Biomaterialia* 47:91–99, 2017.

[64] Lorand, L. Factor XIII: Structure, activation, and interactions with fibrinogen and fibrin. *Annals of the New York Academy of Sciences* 936:291–311, 2001.

[65] Luan, D., M. Zai, and J. D. Varner. Computationally derived points of fragility of a human cascade are consistent with current therapeutic strategies. *PLoS Computational Biology* 3:e142, 2007.

[66] MacDonald, R. L., S. Mojtahedi, L. Johns, and A. Kowalczuk. Randomized comparison of Guglielmi detachable coils and cellulose acetate polymer for treatment of aneurysms in dogs. *Stroke* 29:478–486, 1998.

[67] Madison, E. L., G. S. Coombs, and D. R. Corey. Substrate specificity of tissue type plasminogen activator: Characterization of the fibrin independent specificity of t-PA for plasminogen. *Journal of Biological Chemistry* 270:7558–7562, 1995.

[68] Maitland, D. J., W. Small IV, J. M. Ortega, P. R. Buckley, J. Rodriguez, J. Hartman, and T. S. Wilson. Prototype laser-activated shape memory polymer foam device for embolic treatment of aneurysms. *Journal of Biomedical Optics* 12:030504, 2007.

[69] Manabe, H., S. Fujita, T. Hatayama, S. Suzuki, and S. Yagihashi. Rerupture of coil-embolized aneurysm during long-term observation. *Journal of Neurosurgery* 88:1096–1098, 1998.

[70] Mann, K. G. The assembly of blood clotting complexes on membranes. *Trends in Biochemical Sciences* 12:229–233, 1987.

[71] Mathur, S. R. and J. Y. Murthy. A pressure-based method for unstructured meshes. *Numerical Heat Transfer, Part B: Fundamentals* 31:195–215, 1997.

[72] Meijers, J. C. M., R. A. A. Vlooswijk, and B. N. Bouma. Inhibition of human blood coagulation factor XIa by C1 inhibitor. *Biochemistry* 27:959–963, 1988.

[73] Metcalfe, A., A.-C. Desfaits, I. Salazkin, L. Yahia, W. M. Sokolowski, and J. Raymond. Cold hibernated elastic memory foams for endovascular interventions. *Biomaterials* 24:491–497, 2003.

[74] Molyneux, A. J., R. S. C. Kerr, L.-M. Yu, M. Clarke, M. Sneade, J. A. Yarnold, and P. Sandercock. International subarachnoid aneurysm trial (ISAT) of neurosurgical clipping versus endovascular coiling in 2143 patients with ruptured intracranial aneurysms: a randomised comparison of effects on survival, dependency, seizures, rebleeding, subgroups, and aneurysm occlusion. *Lancet* 366:809–817, 2005.

[75] Monkovi, D. D. and P. B. Tracy. Functional characterization of human platelet-released factor V and its activation by factor Xa and thrombin. *Journal of Biological Chemistry* 265:17132–17140, 1990.

[76] Monkovic, D. D. and P. B. Tracy. Activation of human factor V by factor Xa and thrombin. *Biochemistry* 29:1118–1128, 1990.

[77] Morales, H. G., I. Larrabide, A. J. Geers, D. Dai, D. F. Kallmes, and A. F. Frangi. Analysis and quantification of endovascular coil distribution inside saccular aneurysms using histological images. *Journal of NeuroInterventional Surgery* 5:iii33–7, 2013.

[78] Murayama, Y., F. Viñuela, S. Tateshima, N. R. Gonzalez, J. K. Song, H. Mahdavieh, and L. Iruela-Arispe. Cellular responses of bioabsorbable polymeric material and Guglielmi detachable coil in experimental aneurysms. *Stroke* 33:1120–1128, 2002.

[79] Murayama, Y., F. Viñuela, S. Tateshima, J. K. Song, N. R. Gonzalez, and M. P. Wallace. Bioabsorbable polymeric material coils for embolization of intracranial aneurysms: a preliminary experimental study. *Journal of Neurosurgery* 94:454–463, 2001.

[80] Narracott, A., S. Smith, P. Lawford, H. Liu, R. Himeno, I. Wilkinson, P. Griffiths, and R. Hose. Development and validation of models for the investigation of blood clotting in idealized stenoses and cerebral aneurysms. *Journal of Artificial Organs* 8:56–62, 2005.

[81] Nelb, G. W., C. Gerth, J. D. Ferry, and L. Lorand. Rheology of fibrin clots. III. Shear creep and creep recovery of fine ligated and coarse unligated clots. *Biophysical Chemistry* 5:377–387, 1976.

[82] Nesheim, M. E., R. P. Tracy, and K. G. Mann. "Clotspeed," a mathematical simulation of the functional properties of prothrombinase. *Journal of Biological Chemistry* 259:1447–1453, 1984.

[83] Neuenschwander, P. and J. Jesty. A comparison of phospholipid and platelets in the activation of human factor VIII by thrombin and factor Xa, and in the activation of factor X. *Blood* 72:1761–1770, 1988.

[84] Neuenschwander, P. F. and J. Jesty. Thrombin-activated and factor Xa-activated human factor VIII: Differences in cofactor activity and decay rate. *Archives of Biochemistry and Biophysics* 296:426–434, 1992.

[85] Ortega, J. M. A porous media model for blood flow within reticulated foam. *Chemical Engineering Science* 99:59–66, 2013.

[86] Ortega, J. M., J. Hartman, J. N. Rodriguez, and D. J. Maitland. Virtual treatment of basilar aneurysms using shape memory polymer foam. *Annals of Biomedical Engineering* 41:725–743, 2013.

[87] Ouared, R., B. Chopard, B. Stahl, D. A. Rüfenacht, H. Yilmaz, and G. Courbebaisse. Thrombosis modeling in intracranial aneurysms: a lattice Boltzmann numerical algorithm. *Computer Physics Communications* 179:128–131, 2008.

[88] Ovanesov, M. V., J. V. Krasotkina, L. I. Ul'yanova, K. V. Abushinova, O. P. Plyushch, S. P. Domogatskii, A. I. Vorob'ev, and F. I. Ataullakhanov. Hemophilia A and B are associated with abnormal spatial dynamics of clot growth. *Biochimica et Biophysica Acta* 1572:45–57, 2002.

[89] Panteleev, M. A., M. V. Ovanesov, D. A. Kireev, A. M. Shibeko, E. I. Sinauridze, N. M. Ananyeva, A. A. Butylin, E. L. Saenko, and F. I. Ataullakhanov. Spatial propagation and localization of blood coagulation are regulated by intrinsic and protein C pathways, respectively. *Biophysical Journal* 90:1489–1500, 2006.

[90] Parlea, L., R. Fahrig, D. W. Holdsworth, and S. P. Lownie. An analysis of the geometry of saccular intracranial aneurysms. *American Journal of Neuroradiology* 20:1079–1089, 1999.

[91] Phatouros, C. C., N. S. McConachie, and T. Jaspan. Post-procedure migration of Guglielmi detachable coils and Mechanical detachable spirals. *Neuroradiology* 41:324–327, 1999.

[92] Pixley, R. A., M. Schapira, and R. W. Colman. Effect of heparin on the inactivation rate of human activated factor XII by antithrombin III. *Blood* 66:198–203, 1985.

[93] Pixley, R. A., M. Schapira, and R. W. Colman. The regulation of human factor XIIa by plasma proteinase inhibitors. *Journal of Biological Chemistry* 260:1723–1729, 1985.

[94] Raftopoulos, C., P. Mathurin, D. Boscherini, R. F. Billa, M. Van Boven, and P. Hantson. Prospective analysis of aneurysm treatment in a series of 103 consecutive patients when endovascular embolization is considered the first option. *Journal of Neurosurgery* 93:175–182, 2000.

[95] Rawala-Sheikh, R., S. S. Ahmad, B. Ashby, and P. N. Walsh. Kinetics of coagulation factor X activation by platelet-bound factor IXa. *Biochemistry* 29:2606–2611, 1990.

[96] Raymond, J., F. Guilbert, A. Weill, S. A. Georganos, L. Juravsky, A. Lambert, J. Lamoureux, M. Chagnon, and D. Roy. Long-term angiographic recurrences after selective endovascular treatment of aneurysms with detachable coils. *Stroke* 34:1398–1403, 2003.

[97] Rayz, V. L., L. Boussel, L. Ge, J. R. Leach, A. J. Martin, M. T. Lawton, C. McCulloch, and D. Saloner. Flow residence time and regions of intraluminal thrombus deposition in intracranial aneurysms. *Annals of Biomedical Engineering* 38:3058–3069, 2010.

[98] Reinges, M. H. T., T. Krings, A. Y. Drexler, A. Ludolph, B. Sellhaus, M. Bovi, S. Geibprasert, R. Agid, K. Scherer, and F. J. Hans. Bare, bio-active and hydrogel-coated coils for endovascular treatment of experimentally induced aneurysms. Long-term histological and scanning electron microscopy results. *Interventional Neuroradiology* 16:139–150, 2010.

[99] Reul, J., J. Weis, U. Spetzger, T. Konert, C. Fricke, and A. Thron. Long-term angiographic and histopathologic findings in experimental aneurysms of the carotid bifurcation embolized with platinum and tungsten coils. *American Journal of Neuroradiology* 18:35–42, 1997.

[100] Rodriguez, J. N., F. J. Clubb, T. S. Wilson, M. W. Miller, T. W. Fossum, J. Hartman, E. Tuzun, P. Singhal, and D. J. Maitland. *In vivo* response to an implanted shape memory polyurethane foam in a porcine aneurysm model. *Journal of Biomedical Materials Research, Part A* 102:1231–42, 2014.

[101] Rodriguez, J. N., M. W. Miller, A. Boyle, J. Horn, C. K. Yang, T. S. Wilson, J. M. Ortega, W. Small, L. Nash, H. Skoog, and D. J. Maitland. Reticulation of low density shape memory polymer foam with an in vivo demonstration of vascular occlusion. *Journal of the Mechanical Behavior of Biomedical Materials* 40:102–114, 2014.

[102] Rodriguez, J. N., Y.-J. Yu, M. W. Miller, T. S. Wilson, J. Hartman, F. J. Clubb, B. Gentry, and D. J. Maitland. Opacification of shape memory polymer foam designed for treatment of intracranial aneurysms. *Annals of Biomedical Engineering* 40:883–897, 2012.

[103] Roy, D., G. Milot, and J. Raymond. Endovascular treatment of unruptured aneurysms. *Stroke* 32:1998–2004, 2001.

[104] Sakariassen, K. S., P. A. Holme, U. Ørvim, R. Marius Barstad, N. O. Solum, and F. R. Brosstad. Shear-induced platelet activation and platelet microparticle formation in native human blood. *Thrombosis Research* 92:S33–S41, 1998.

[105] Schousboe, I., K. Feddersen, and R. Røjkjaer. Factor XIIa is a kinetically favorable plasminogen activator. *Thrombosis and Haemostasis* 82:1041–1046, 1999.

[106] Schwartz, M. L., S. V. Pizzo, R. L. Hill, and P. A. McKee. The subunit structures of human plasma and platelet factor XIII (fibrin-stabilizing factor). *Journal of Biological Chemistry* 246:5851–5854, 1971.

[107] Scott, C. F., M. Schapira, H. L. James, A. B. Cohen, and R. W. Colman. Inactivation of factor XIa by plasma protease inhibitors. Predominant role of α_1-protease inhibitor and protective effect of high molecular weight kininogen. *Journal of Clinical Investigation* 69:844–852, 1982.

[108] Sherif, C., H. Plenk, K. Grossschmidt, F. Kanz, and G. Bavinzski. Computer-assisted quantification of occlusion and coil densities on angiographic and histological images of experimental aneurysms. *Neurosurgery* 58:559–566, 2006.

[109] Silverberg, M. and A. P. Kaplan. Enzymatic activities of activated and zymogen forms of human Hageman factor (factor XII). *Blood* 60:64–70, 1982.

[110] Singhal, P., J. N. Rodriguez, W. Small, S. Eagleston, J. Van de Water, D. J. Maitland, and T. S. Wilson. Ultra low density and highly crosslinked biocompatible shape memory polyurethane foams. *Journal of Polymer Science Part B: Polymer Physics* 50:724–737, 2012.

[111] Slob, M. J., W. J. van Rooij, and M. Sluzewski. Influence of coil thickness on packing, re-opening and retreatment of intracranial aneurysms: a comparative study between two types of coils. *Neurological Research* 27:116–119, 2005.

[112] Sluzewski, M., W. J. van Rooij, M. J. Slob, J. O. Bescós, C. H. Slump, and D. Wijnalda. Relation between aneurysm volume, packing, and compaction in 145 cerebral aneurysms treated with coils. *Radiology* 231:653–658, 2004.

[113] Small IV, W., E. Gjersing, J. L. Herberg, T. S. Wilson, and D. J. Maitland. Magnetic resonance flow velocity and temperature mapping of a shape memory polymer foam device. *BioMedical Engineering OnLine* 8:42, 2009.

[114] Solymoss, S., M. M. Tucker, and P. B. Tracy. Kinetics of inactivation of membrane-bound factor Va by activated protein C. Protein S modulates factor Xa protection. *Journal of Biological Chemistry* 263:14884–14890, 1988.

[115] Soons, H., T. Janssen-Claessen, G. Tans, and H. C. Hemker. Inhibition of factor XI_a by antithrombin III. *Biochemistry* 26:4624–4629, 1987.

[116] Spetzger, U., J. Reul, J. Weis, H. Bertalanffy, A. Thron, and J. M. Gilsbach. Microsurgically produced bifurcation aneurysms in a rabbit model for endovascular coil embolization. *Journal of Neurosurgery* 85:488–495, 1996.

[117] Starling, R. C., N. Moazami, S. C. Silvestry, G. Ewald, J. G. Rogers, C. A. Milano, J. E. Rame, M. A. Acker, E. H. Blackstone, J. Ehrlinger, L. Thuita, M. M. Mountis, E. G.

Soltesz, B. W. Lytle, and N. G. Smedira. Unexpected abrupt increase in left ventricular assist device thrombosis. *New England Journal of Medicine* 370:33–40, 2014.

[118] Stehbens, W. E. Pathology and pathogenesis of intracranial berry aneurysms. *Neurological Research* 12:29–34, 1990.

[119] Sun, Y. and D. Gailani. Identification of a factor IX binding site on the third apple domain of activated factor XI. *Journal of Biological Chemistry* 271:29023–29028, 1996.

[120] Szikora, I., P. Seifert, Z. Hanzely, Z. Kulcsar, Z. Berentei, M. Marosfoi, S. Czirjak, J. Vajda, and I. Nyary. Histopathologic evaluation of aneurysms treated with Guglielmi detachable coils or Matrix detachable microcoils. *American Journal of Neuroradiology* 27:283–288, 2006.

[121] Takeyama, M., J. M. Wintermute, C. Manithody, A. R. Rezaie, and P. J. Fay. Variable contributions of basic residues forming an APC exosite in the binding and inactivation of factor VIIIa. *Biochemistry* 52:2228–2235, 2013.

[122] Tankersley, D. L. and J. S. Finlayson. Kinetics of activation and autoactivation of human factor XII. *Biochemistry* 23:273–279, 1984.

[123] Tsiang, M., L. R. Paborsky, W. X. Li, A. K. Jain, C. T. Mao, K. E. Dunn, D. W. Lee, S. Y. Matsumura, M. D. Matteucci, S. E. Coutré, L. L. K. Leung, and C. S. Gibbs. Protein engineering thrombin for optimal specificity and potency of anticoagulant activity *in vivo*. *Biochemistry* 35:16449–16457, 1996.

[124] Turk, A. S., C. M. Luty, V. Carr-Brendel, I. Polyakov, D. Consigny, J. Grinde, R. Mukherjee, and C. M. Strother. Angiographic and histological comparison of canine bifurcation aneurysms treated with first generation matrix and standard GDC coils. *Neuroradiology* 50:57–65, 2008.

[125] Van der Graaf, F., J. A. Koedam, and B. N. Bouma. Inactivation of kallikrein in human plasma. *Journal of Clinical Investigation* 71:149–158, 1983.

[126] Vanzin, J. R., D. G. Abud, M. T. S. Rezende, and J. Moret. Number of coils necessary to treat cerebral aneurysms according to each size group: a study based on a series of 952 embolized aneurysms. *Arquivos de Neuro-Psiquiatria* 70:520–523, 2012.

[127] Vogler, E. A. and C. A. Siedlecki. Contact activation of blood-plasma coagulation. *Biomaterials* 30:1857–1869, 2009.

[128] Wakhloo, A. K., M. J. Gounis, J. S. Sandhu, N. Akkawi, A. E. Schenck, and I. Linfante. Complex-shaped platinum coils for brain aneurysms: Higher packing density, improved biomechanical stability, and midterm angiographic outcome. *American Journal of Neuroradiology* 28:1395–1400, 2007.

[129] Wang, C. and X. Xie. Treatment of an unraveled intracerebral coil. *Catheterization and Cardiovascular Interventions* 76:746–750, 2010.

[130] Wiebe, E. M., A. R. Stafford, J. C. Fredenburgh, and J. I. Weitz. Mechanism of catalysis of inhibition of factor IXa by antithrombin in the presence of heparin or pentasaccharide. *Journal of Biological Chemistry* 278:35767–35774, 2003.

[131] Wierzbicki, M. A., J. Bryant, M. W. Miller, B. Keller, and D. J. Maitland. Mechanical and *in vitro* evaluation of an experimental canine patent ductus arteriosus occlusion device. *Journal of the Mechanical Behavior of Biomedical Materials* 59:156–167, 2016.

[132] Wu, W.-T., M. A. Jamiolkowski, W. R. Wagner, N. Aubry, M. Massoudi, and J. F. Antaki. Multi-constituent simulation of thrombus deposition. *Scientific Reports* 7:42720, 2017.

[133] Xu, Z., N. Chen, M. M. Kamocka, E. D. Rosen, and M. Alber. A multiscale model of thrombus development. *Journal of The Royal Society, Interface* 5:705–722, 2008.

[134] Xu, Z., J. Lioi, J. Mu, M. M. Kamocka, X. Liu, D. Z. Chen, E. D. Rosen, and M. Alber. A multiscale model of venous thrombus formation with surface-mediated control of blood coagulation cascade. *Biophysical Journal* 98:1723–1732, 2010.

[135] Zarnitsina, V. I., A. V. Pokhilko, and F. I. Ataullakhanov. A mathematical model for the spatio-temporal dynamics of intrinsic pathway of blood coagulation. I. The model description. *Thrombosis Research* 84:225–236, 1996.

[136] Zhuo, R., C. A. Siedlecki, and E. A. Vogler. Autoactivation of blood factor XII at hydrophilic and hydrophobic surfaces. *Biomaterials* 27:4325–4332, 2006.

APPENDIX A

MESH AND TIME STEP CONVERGENCE

A.1 Mesh Convergence

A mesh convergence study was conducted for the foam-filled aneurysm simulation described in Chapter 3. Three meshes were considered with increasing mesh density, denoted as coarse mesh, medium mesh, and fine mesh. The general mesh parameters are listed for each mesh in Table A.1. Within the parent and branching vessels, the meshes have identical parameters as the clotting cascades are not expected to be relevant since the high velocity (relative to inside the aneurysm) in the vessels quickly flushes the biochemicals through the system. Each of the three meshes is refined within the aneurysm sac (see Figure A.1). Figures A.2 and A.3 show the mesh refinement for each mesh within a representative foam pore and along a typical foam strut boundary. Clot generation simulations were conducted within each mesh, using the medium-fidelity model discussed in Chapter 2. To compare the simulation results, percent occlusion as a function of time is plotted for each mesh in Figure A.4. Qualitatively, the differences between the three curves are minimal. To quantify the differences between the percent occlusions predicted using the three meshes, the following parameters were calculated: the final aneurysm occlusion taken as the mean percent occlusion during the final 10 seconds of simulation (315 to 325 s); and the time when the percent occlusion equals 50%. The values for these parameters are listed in Table A.2. Additionally, the root-mean-square deviation (RMSD),

$$RMSD = \sqrt{\sum_{i=1}^{n} \frac{\left(CV_{1,i} - CV_{2,i}\right)^2}{n}} \tag{A.1}$$

between the percent occlusion curves for the coarse and medium meshes and between the curves for the medium and fine meshes were calculated (see Table A.2). Based on these parameters, the differences in the percent occlusions as a function of time generated using the three meshes are quantitatively minimal and the differences between the meshes are smaller between the medium and fine mesh than between the coarse and medium meshes. Thus, the medium mesh was determined to be sufficient for mesh independence and was used for the simulations presented in Chapter 3 and similar parameters were used for the simulations in Chapter 4.

Mesh Parameter	Coarse Mesh	Medium Mesh	Fine Mesh
Base Size – Vessel	80	80	80
# Prism Layer – Vessel Walls	6	6	6
Near-Wall Prism Layer Thickness – Vessel Walls	8	8	8
Base Size - Aneurysm	40	20	10
# Prism Layer – Vessel Walls	5	11	11
Near-Wall Prism Layer Thickness – Aneurysm Walls	4	2	1
# Prism Layer – Strut Walls	5	9	12
Near-Wall Prism Layer Thickness – Strut Walls	2	1	0.5

Table A.1: Mesh parameters, listed in microns, for the three meshes considered during mesh convergence testing within the foam-filled aneurysm geometry described in Chapter 3.

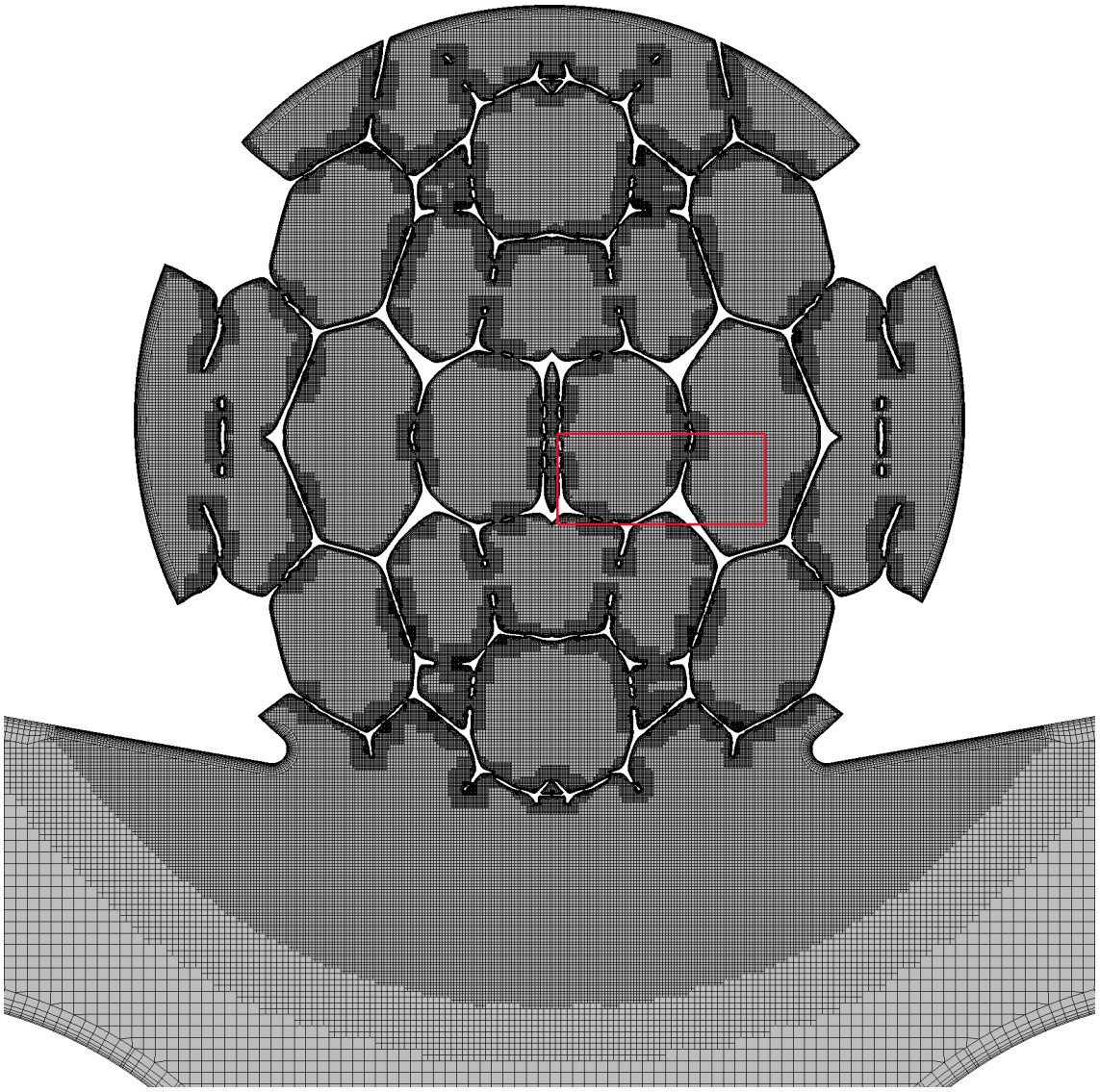

Figure A.1: Medium mesh applied to the foam-filled aneurysm in Chapter 3. The area within the red box is displayed in Figure A.2 for the three meshes considered during mesh convergence testing.

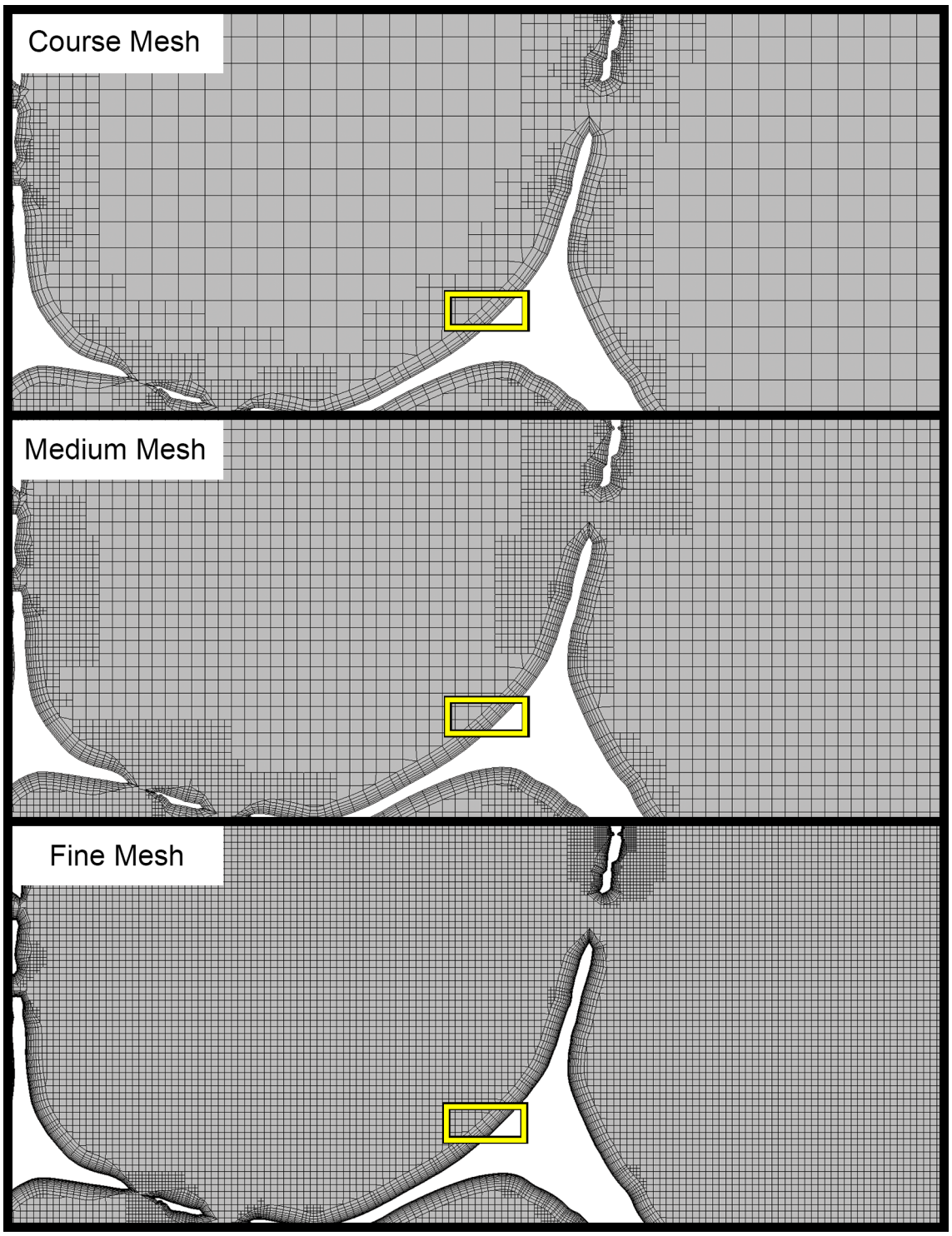

Figure A.2: Coarse, medium, and fine meshes within the region denoted by the red box in Figure A.1. The areas within the yellow boxes are displayed for each mesh in Figure A.3.

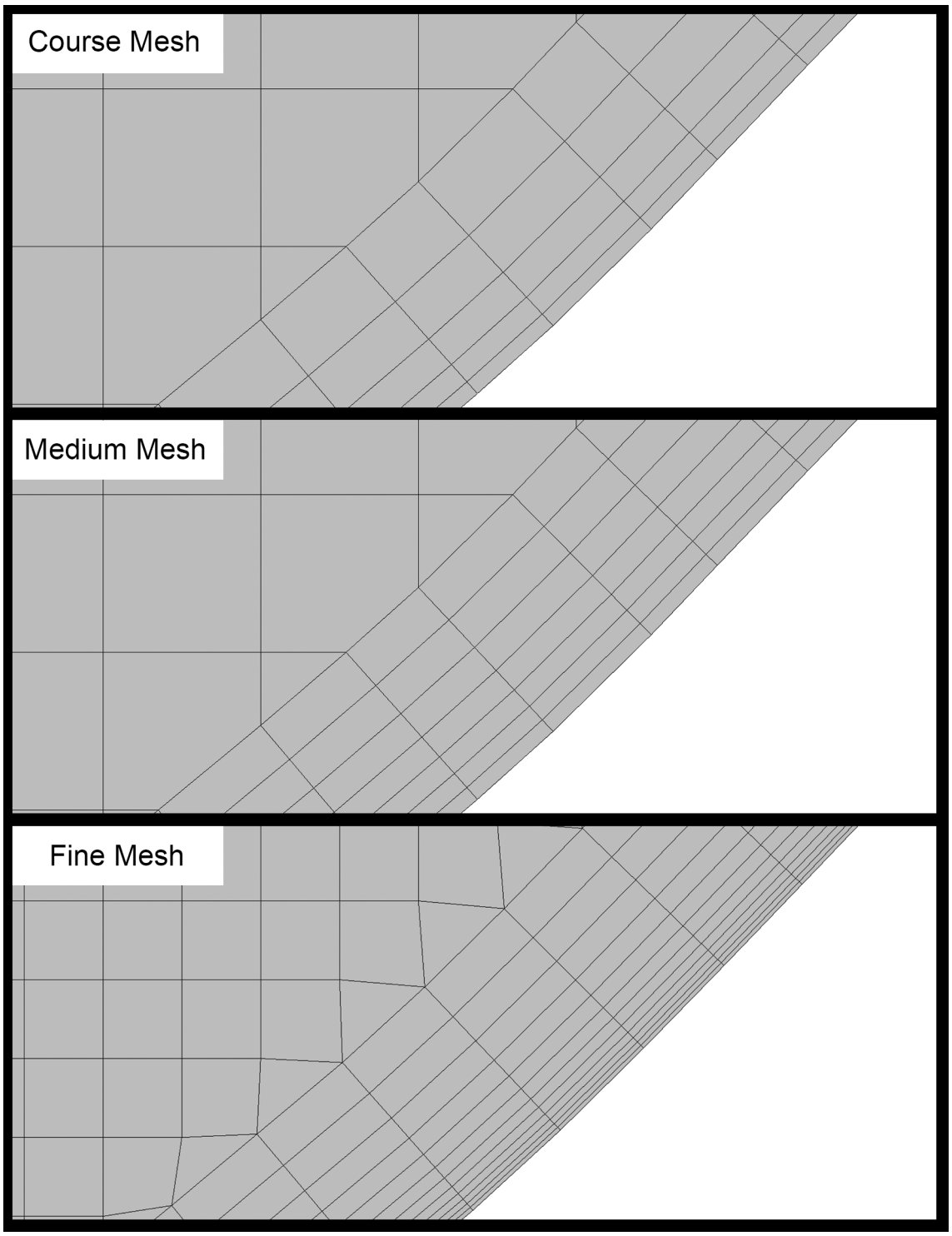

Figure A.3: Zoomed-in view of the coarse, medium, and fine meshes within a representative region along a strut wall boundary as indicated by the yellow boxes in Figure A.2.

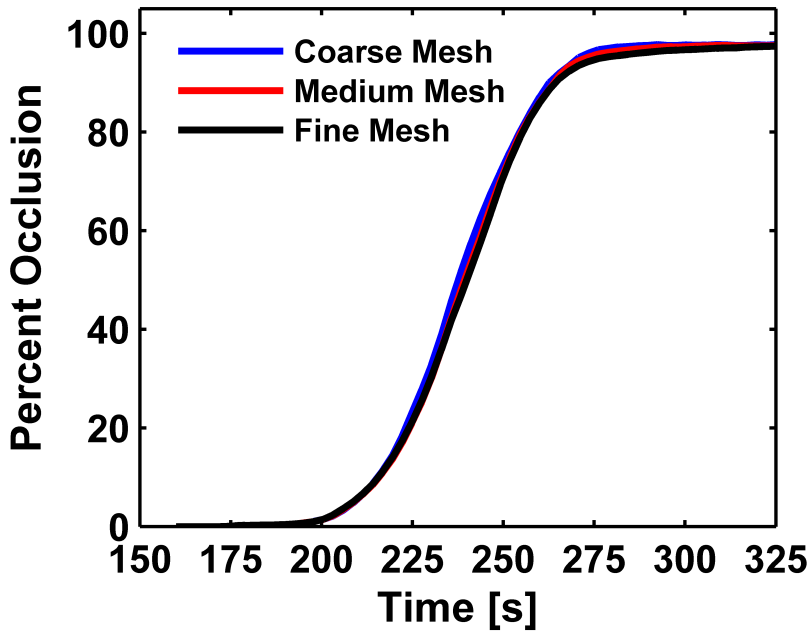

Figure A.4: Mesh convergence study results. Percent occlusion as a function of time in the foam-filled aneurysm using each mesh and a timestep of 0.002 s.

	Coarse Mesh	Medium Mesh	Fine Mesh
Final aneurysm occlusion	97.66 %	96.46 %	97.27 %
(percent difference)		-0.204 %	-0.195 %
Time to 50% occlusion	237.61 s	239.56 s	239.96 s
(percent difference)		0.737 %	0.251 %
RMSD		1.31 %	0.56 %

Table A.2: Parameters for the mesh convergence study. The percent differences are calculated as: (medium - coarse)/ coarse * 100% and (fine - medium)/ medium * 100%.

A.2 Time Step Independence

In addition to mesh convergence, time step independence was also evaluated. The simulation discussed in Chapter 3 was repeated with time steps ranging from 0.001 seconds to 0.004 seconds using the medium mesh. Percent occlusion as a function of time in each of the simulations is plotted in Figure A.5. Also, the differences in the results were quantified using the parameters described above for the mesh convergence test (see Table A.3). All time steps produced comparable results and a time step of 0.002 s was considered sufficiently converged. Simulation results reported in Chapter 3 and Chapter 4 were obtained using this time step.

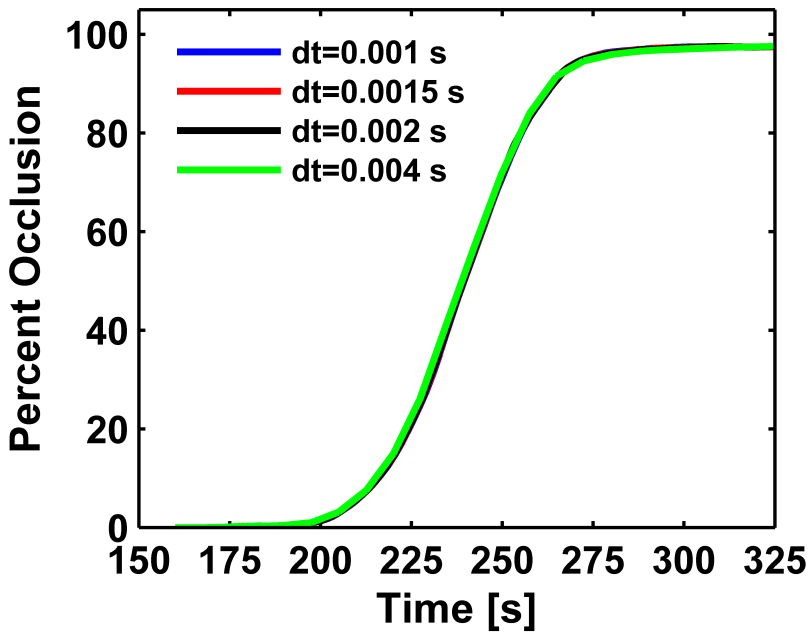

Figure A.5: Time step independence study results. Percent occlusion as a function of time in the foam-filled aneurysm using each time step and the medium mesh.

	dt=0.004 s	dt=0.002 s	dt=0.0015 s	dt=0.001 s
Final aneurysm occlusion	97.47 %	97.45 %	97.46 %	97.45 %
(percent difference)		-0.020 %	0.002 %	-0.010 %
Time to 50% occlusion	238.94 s	239.32 s	239.36 s	239.45 s
(percent difference)		0.156 %	0.017 %	0.040 %
RMSD		0.49 %	0.09 %	0.14 %

Table A.3: Parameters for the time step convergence study. Percent differences are computed as (smaller dt - larger dt)/ larger dt * 100%. To compute RMSD, linear interpolation was used to define each curve at the same time points.

APPENDIX B

TRANSIENT CLOT PROGRESSION IN EACH FOAM- AND COIL-TREATED ANEURYSM

The figures in this appendix show the clot growth over time, predicted by the medium-fidelity thrombus model, within each aneurysm simulated in Chapter 4. In all images, clotted blood is indicated in black.

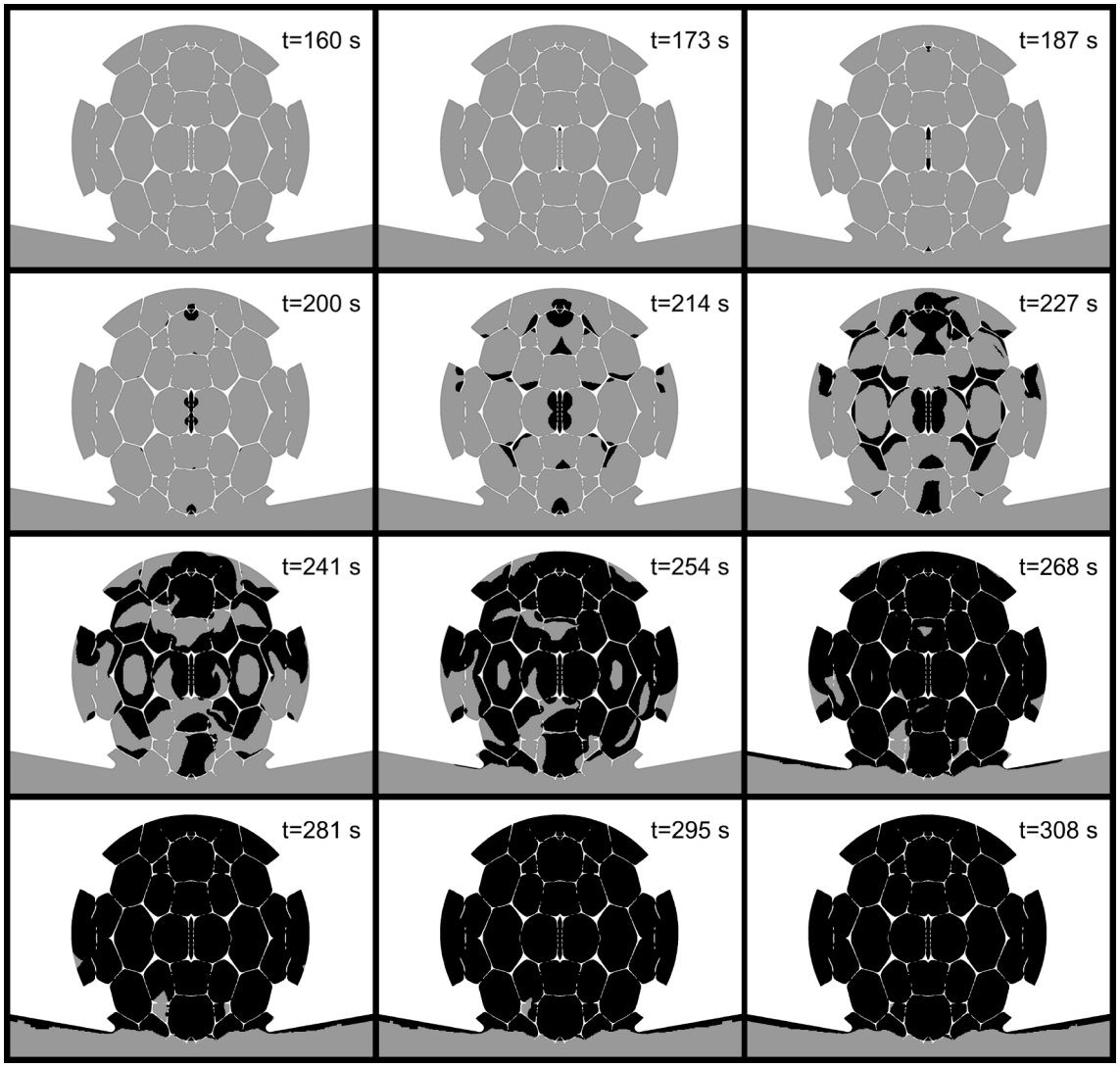

Figure B.1: Clot distribution over time in the foam-filled aneurysm predicted by medium-fidelity thrombus model. Unscaled foam with 0-degree rotation.

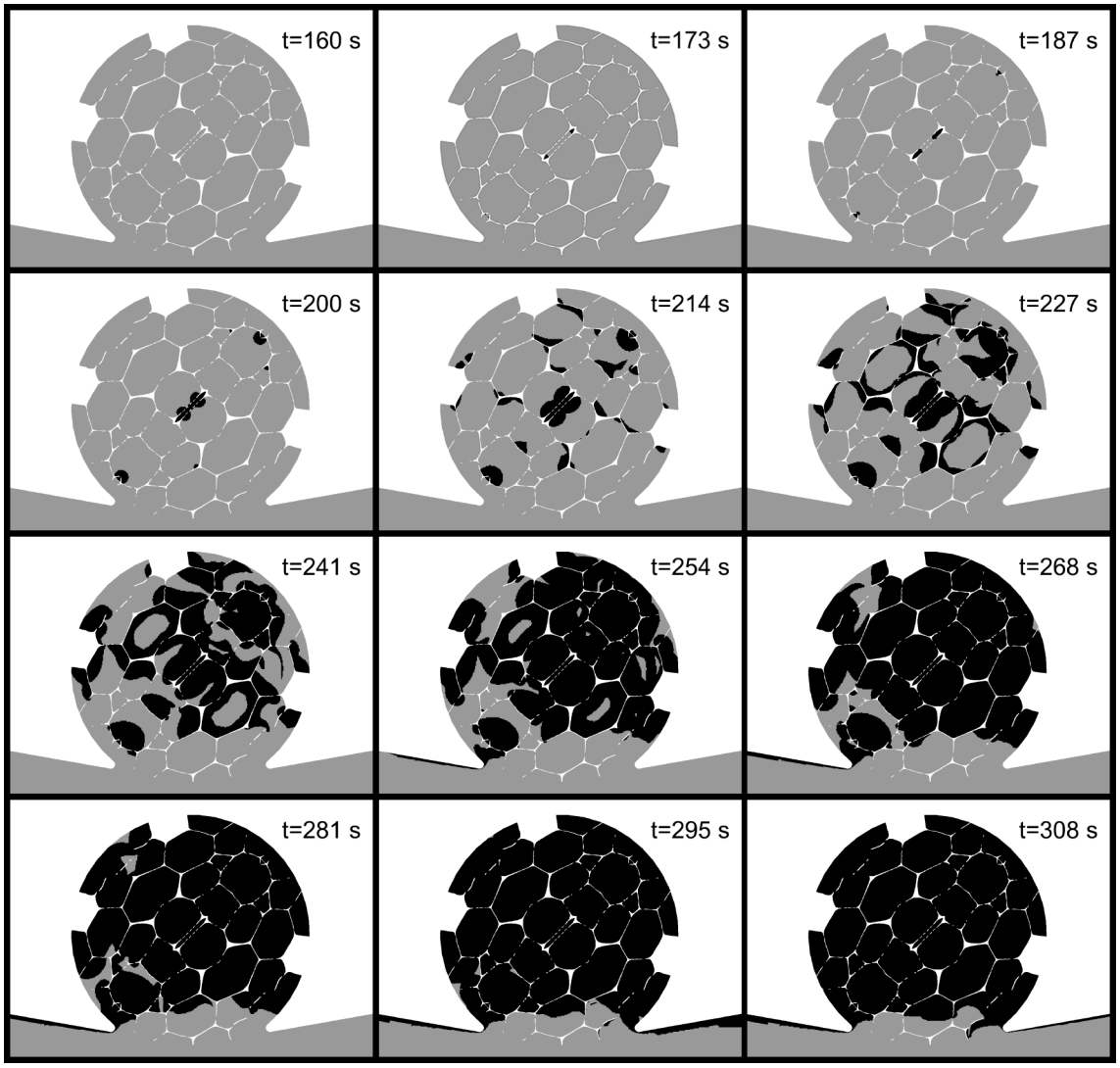

Figure B.2: Clot distribution over time in the foam-filled aneurysm predicted by medium-fidelity thrombus model. Unscaled foam with 45-degree rotation.

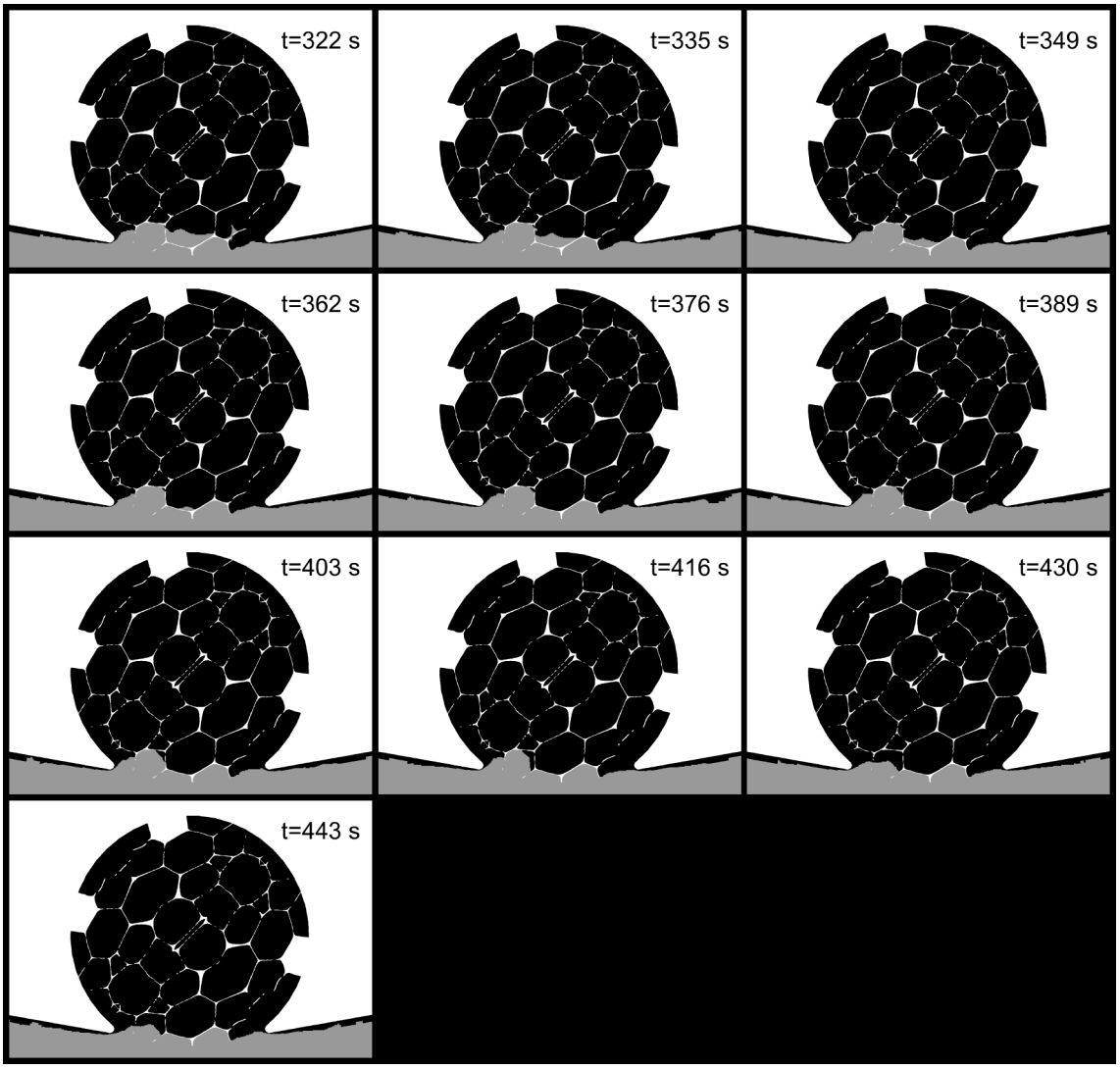

Figure B.2: Continued.

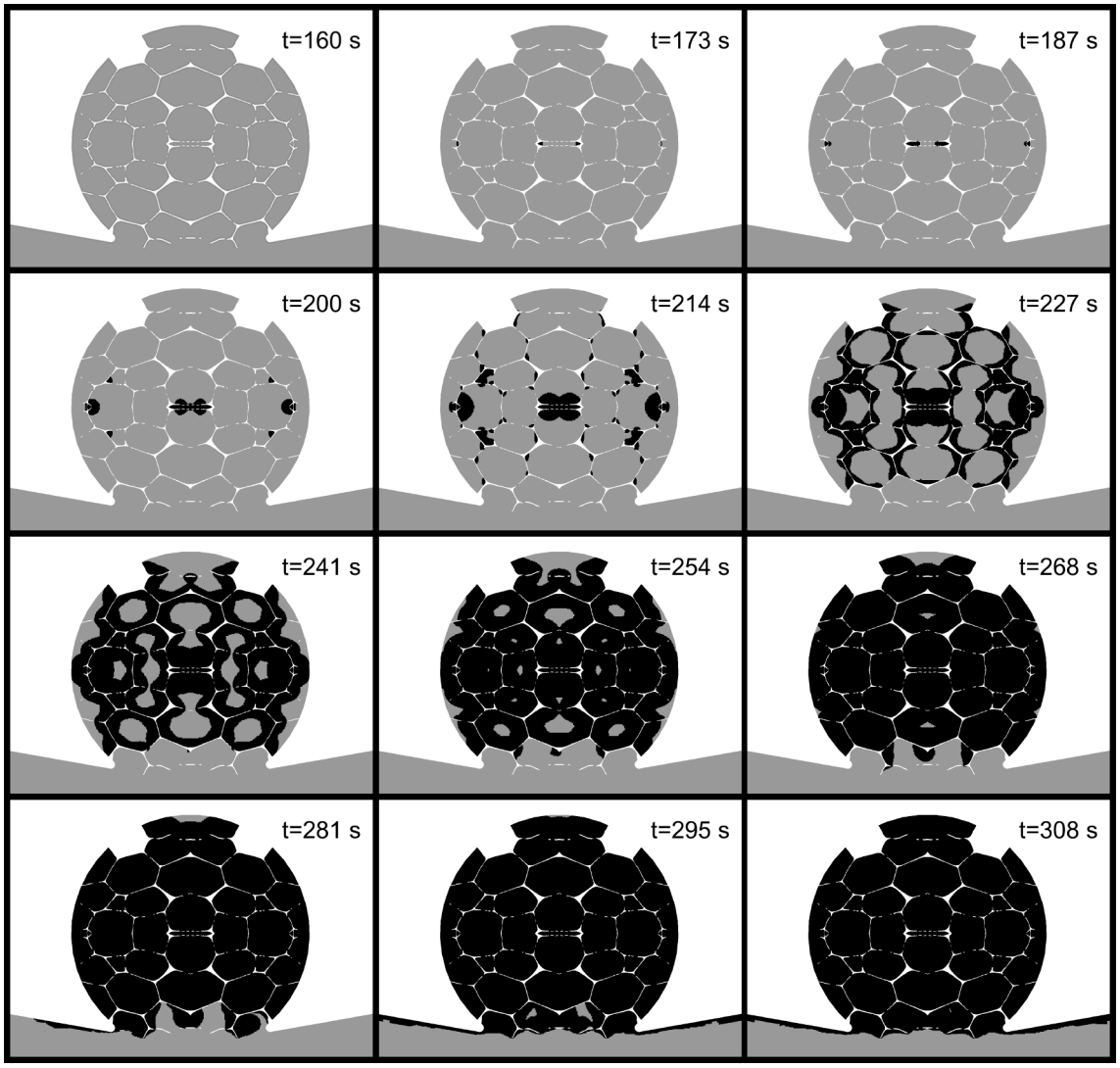

Figure B.3: Clot distribution over time in the foam-filled aneurysm predicted by medium-fidelity thrombus model. Unscaled foam with 90-degree rotation.

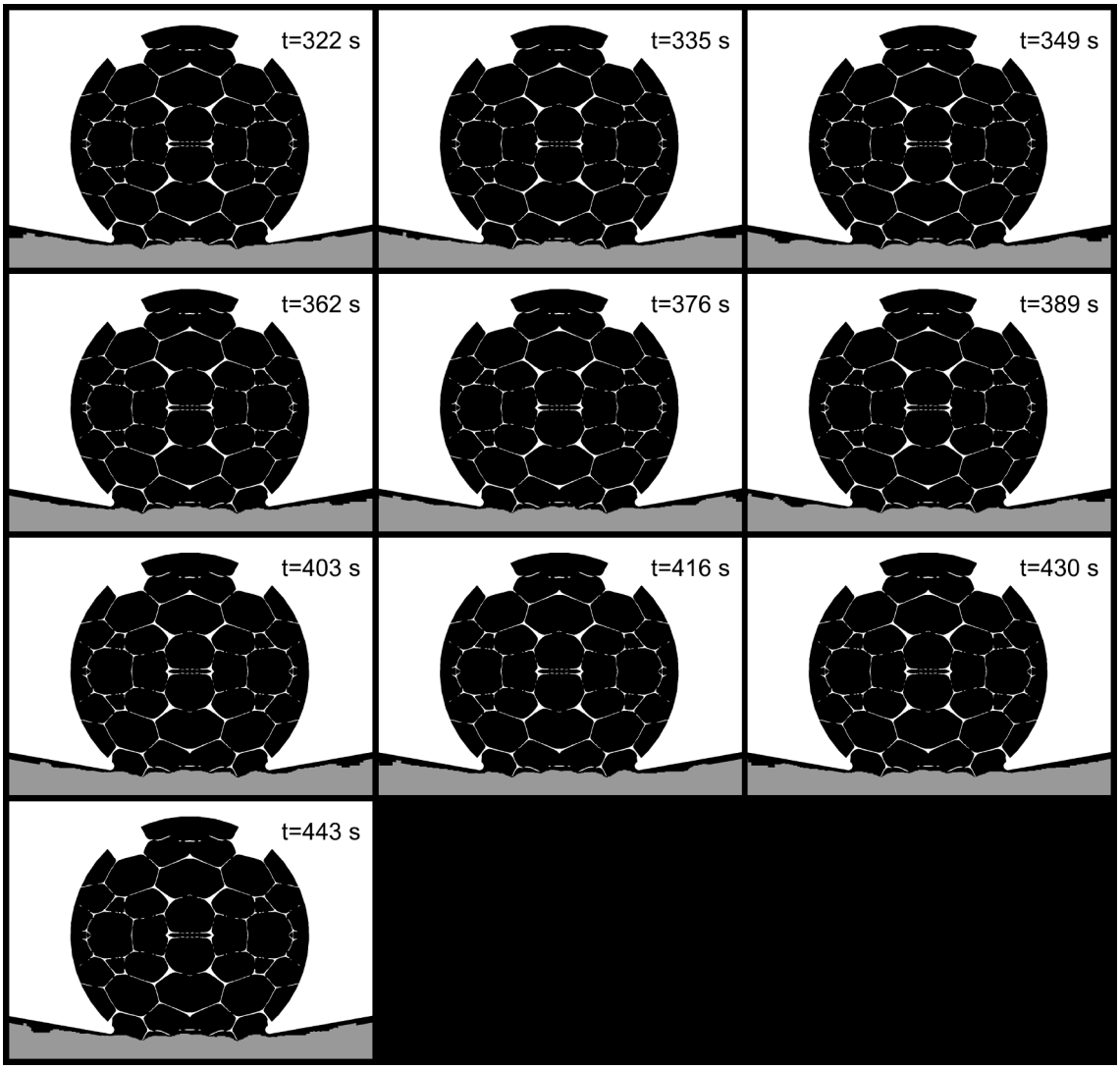

Figure B.3: Continued.

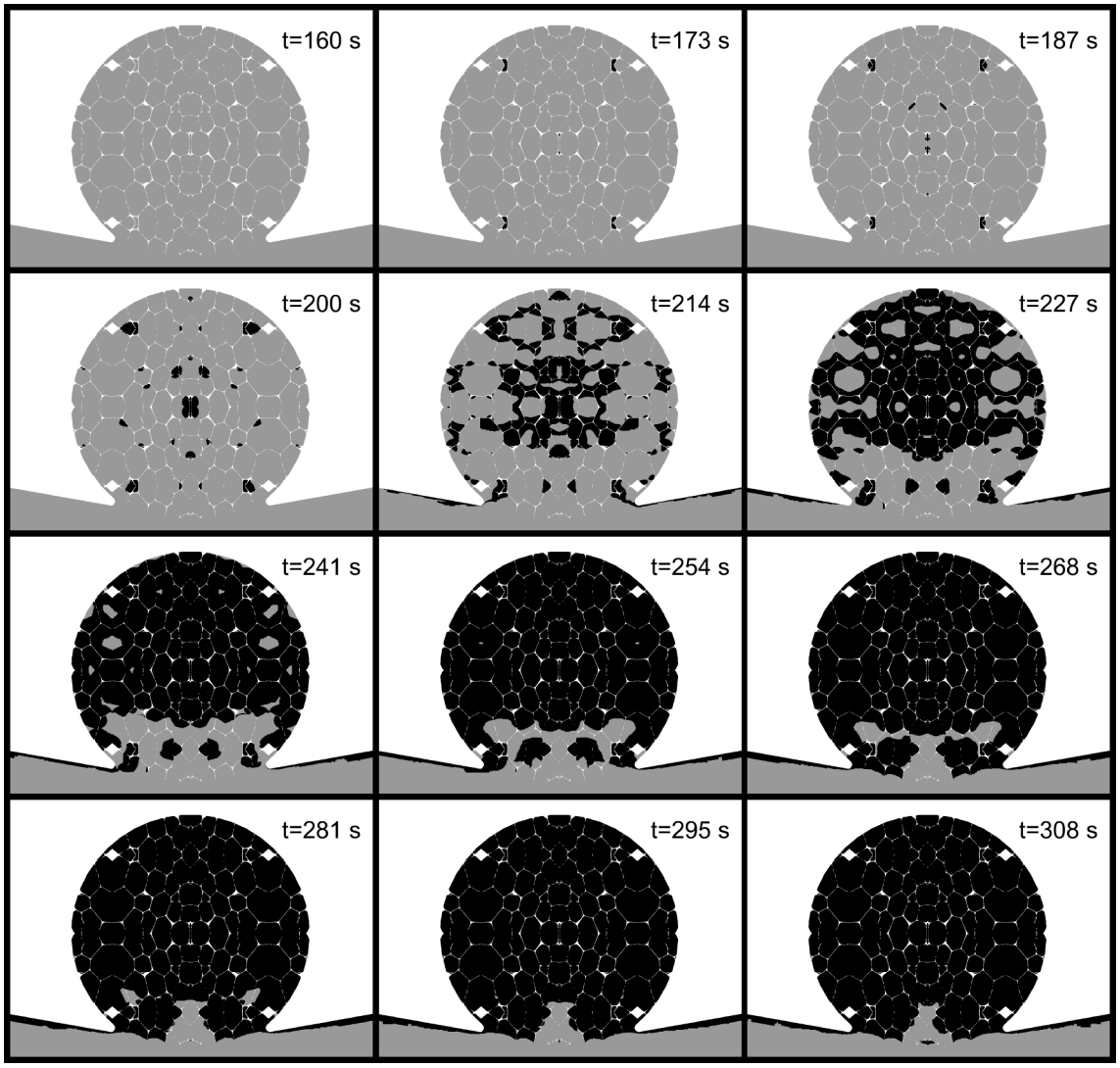

Figure B.4: Clot distribution over time in the foam-filled aneurysm predicted by medium-fidelity thrombus model. 1/2x-scaled foam with 0-degree rotation.

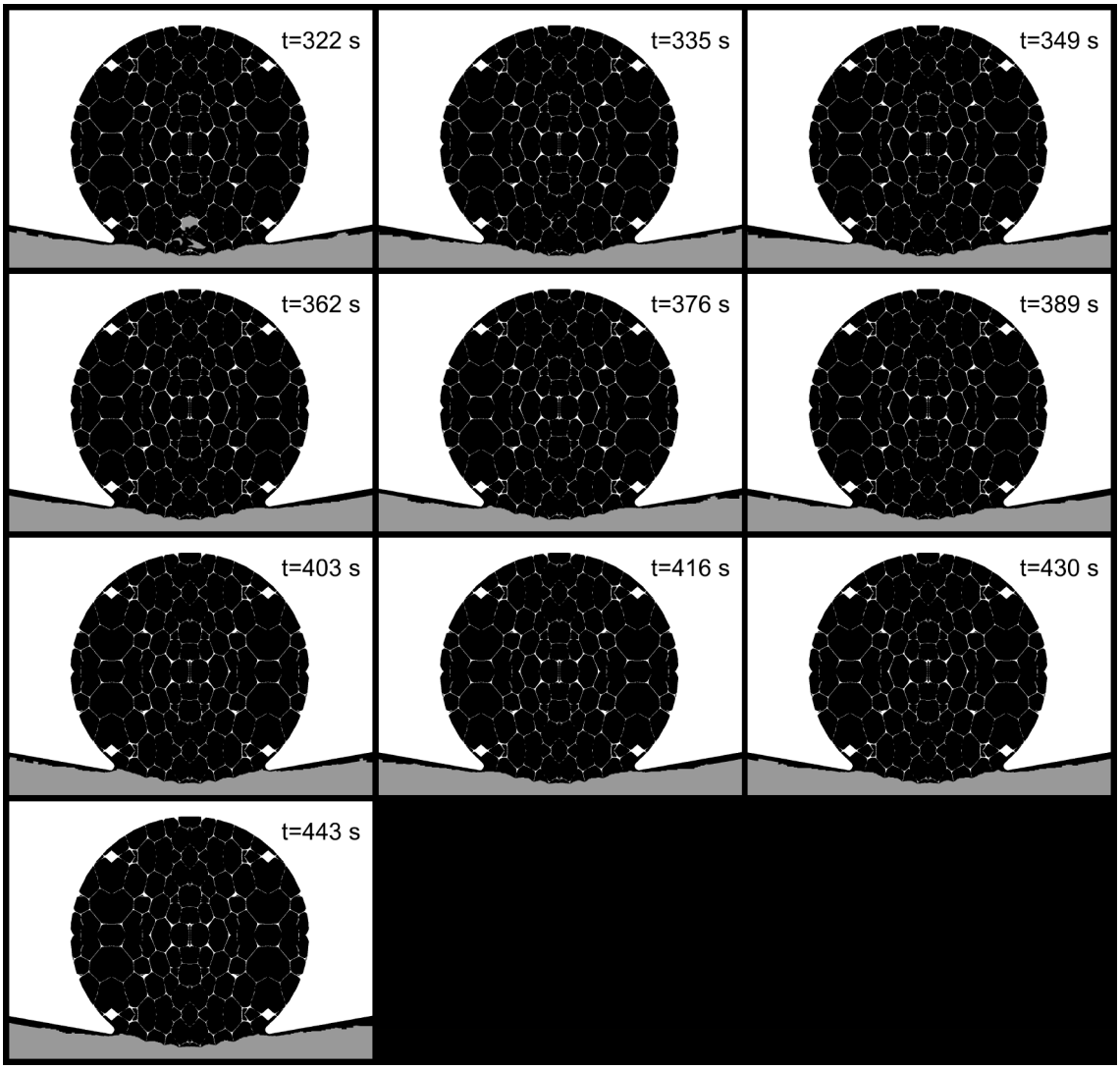

Figure B.4: Continued.

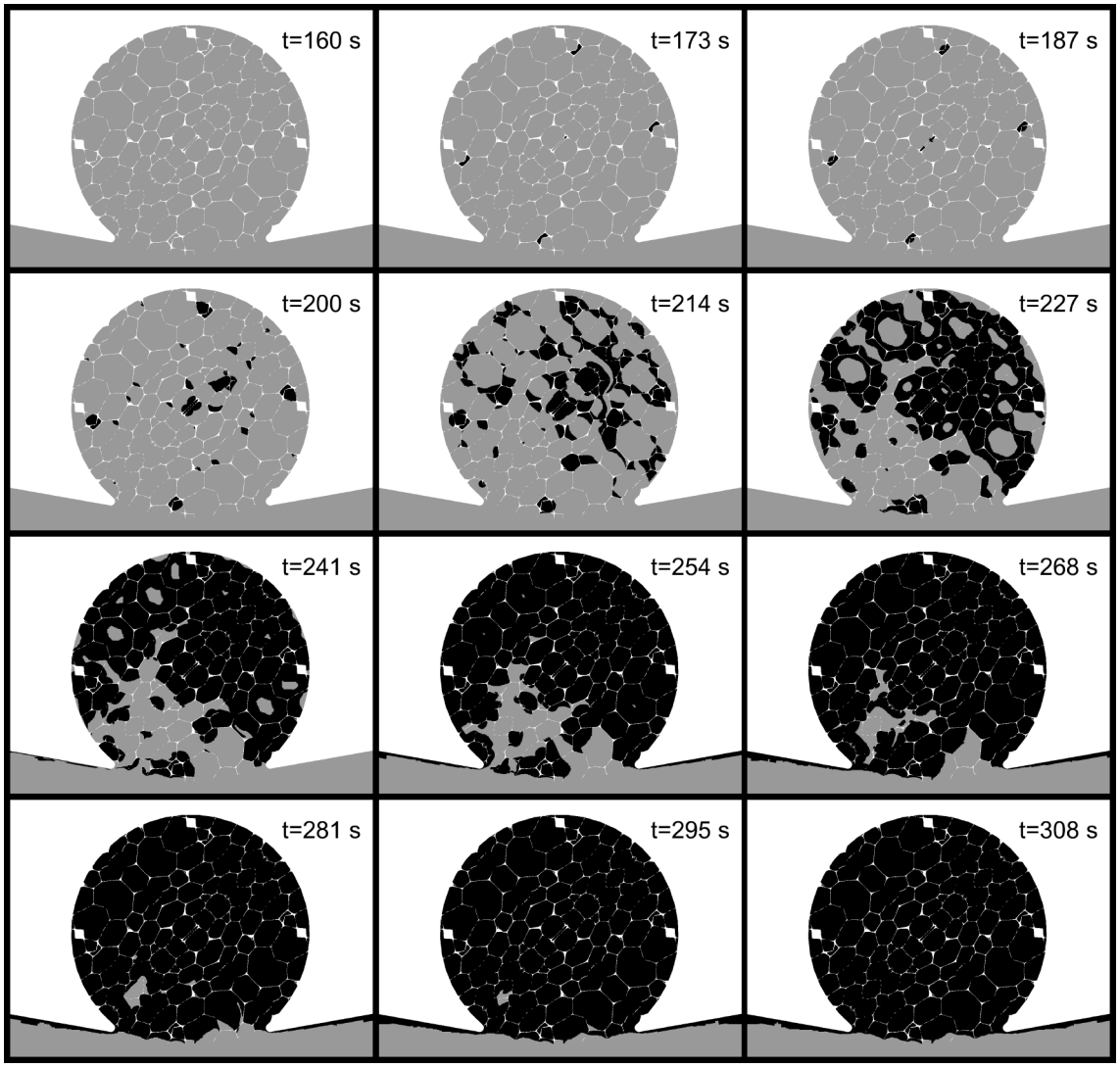

Figure B.5: Clot distribution over time in the foam-filled aneurysm predicted by medium-fidelity thrombus model. 1/2x-scaled foam with 45-degree rotation.

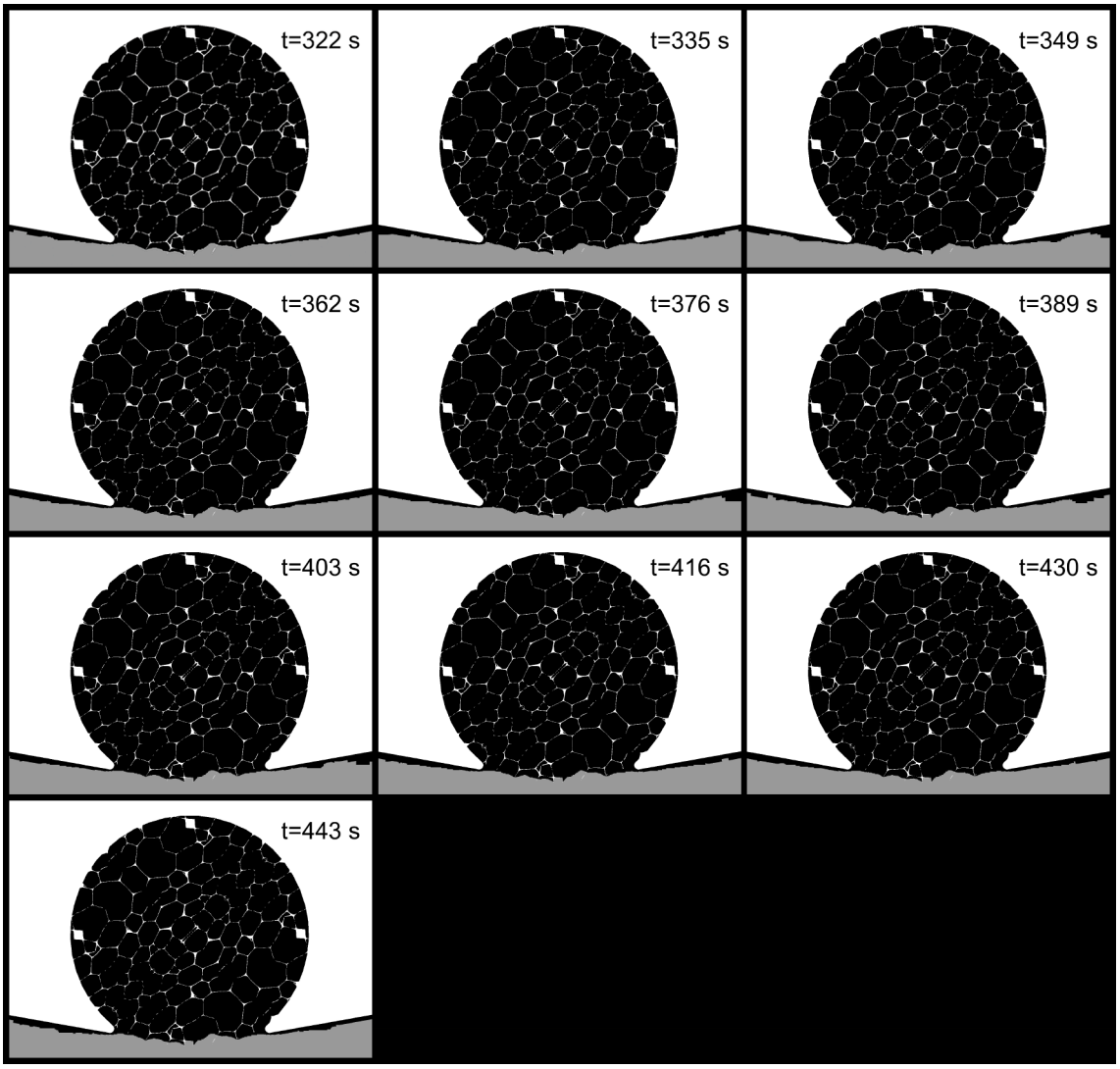

Figure B.5: Continued.

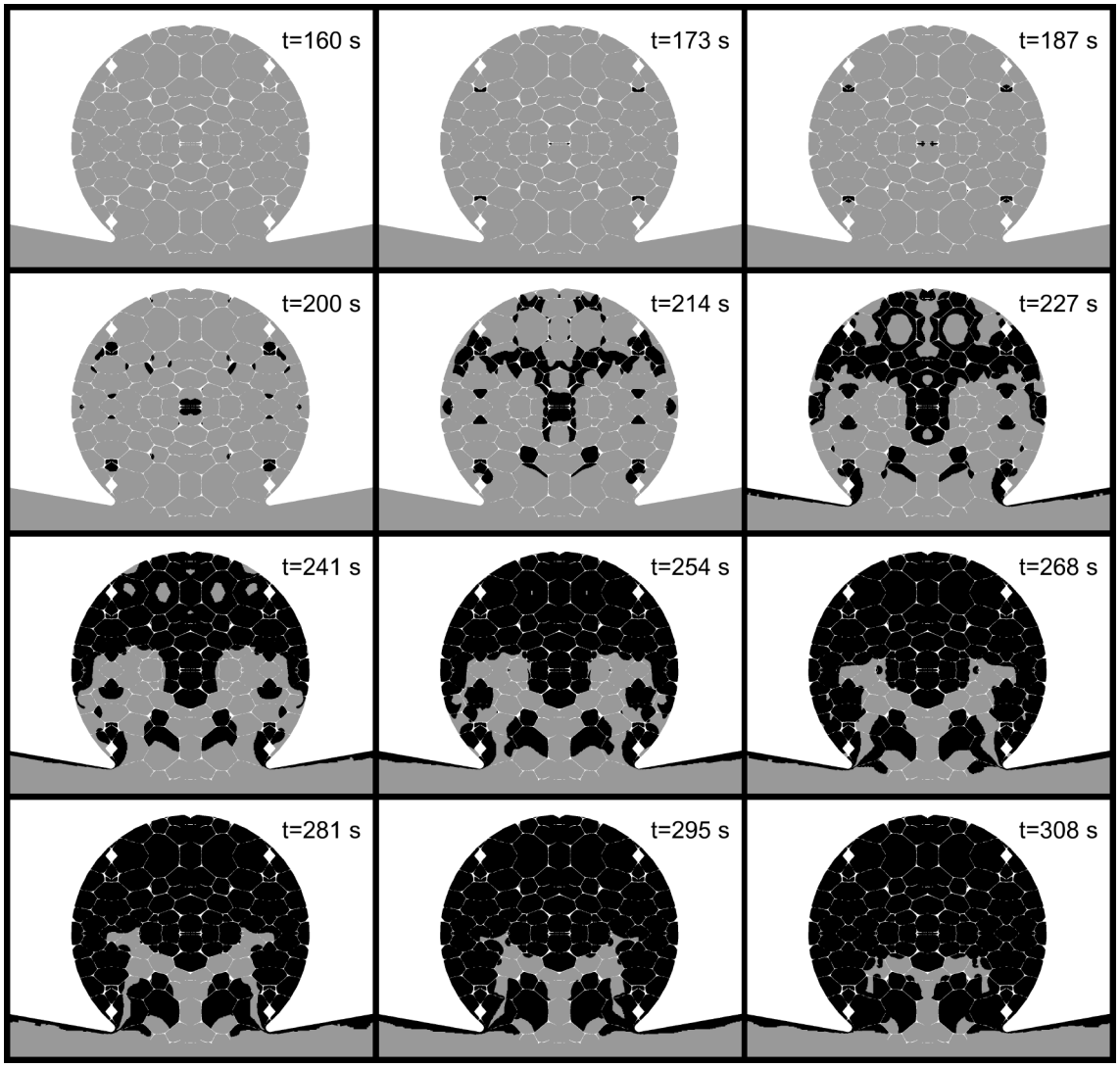

Figure B.6: Clot distribution over time in the foam-filled aneurysm predicted by medium-fidelity thrombus model. 1/2x-scaled foam with 90-degree rotation.

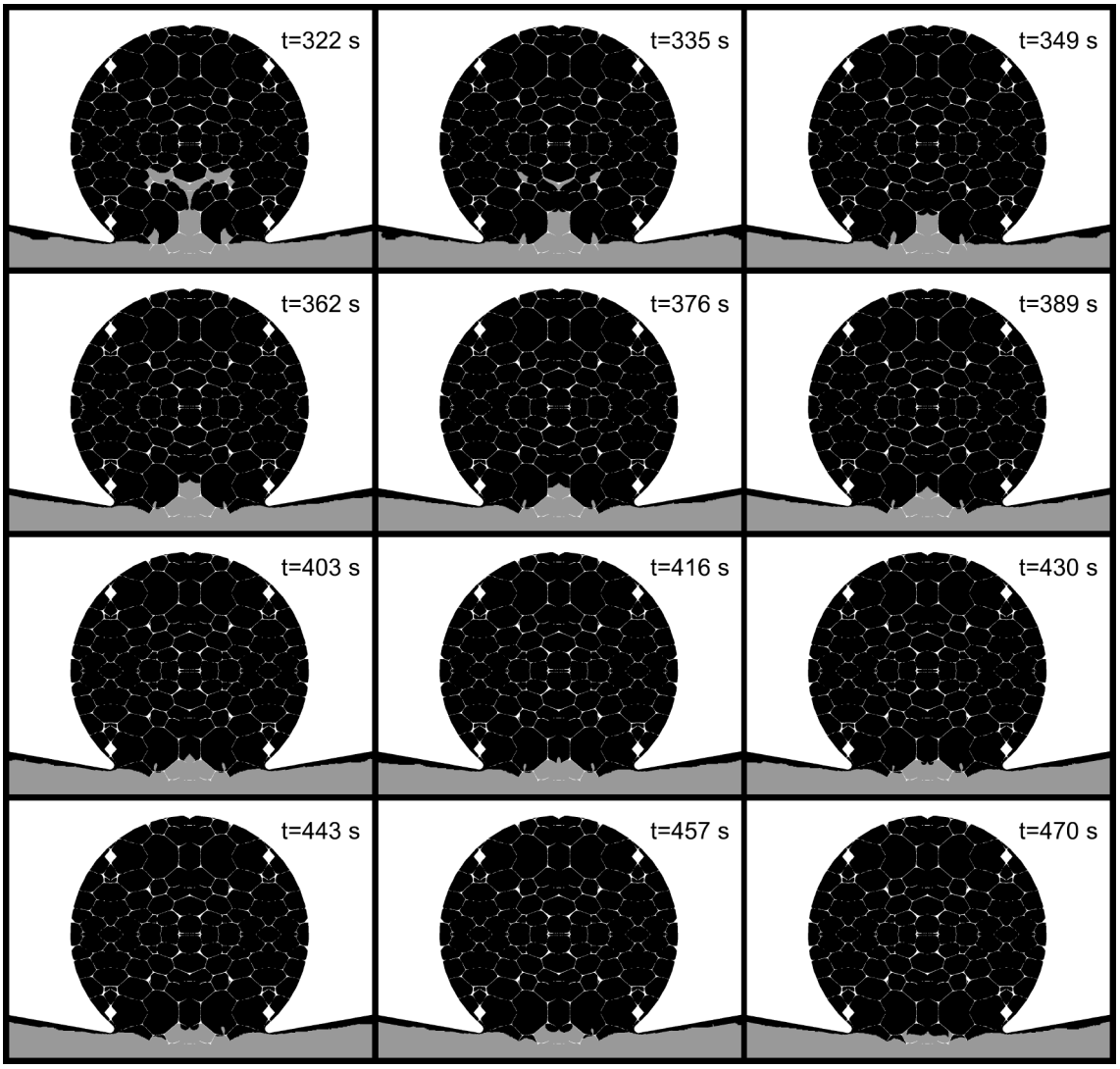

Figure B.6: Continued.

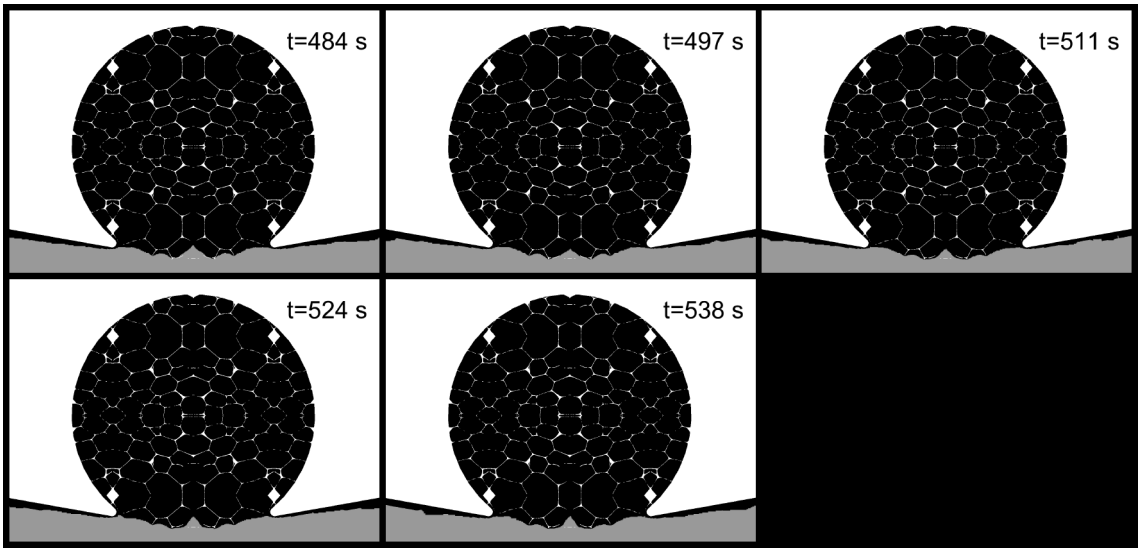

Figure B.6: Continued.

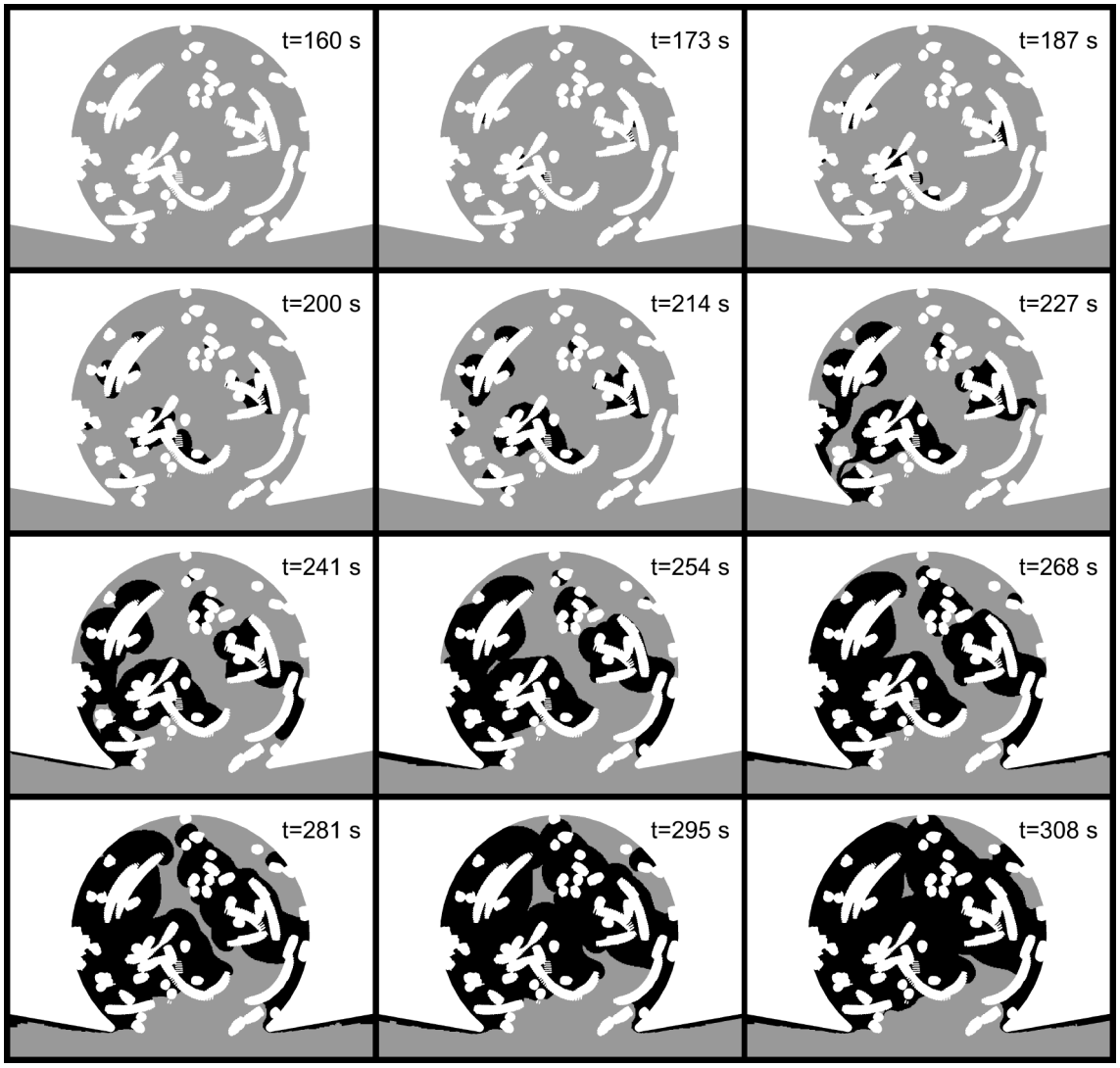

Figure B.7: Clot distribution over time in the coil-filled aneurysm predicted by the medium-fidelity thrombus model. Coil case #1.

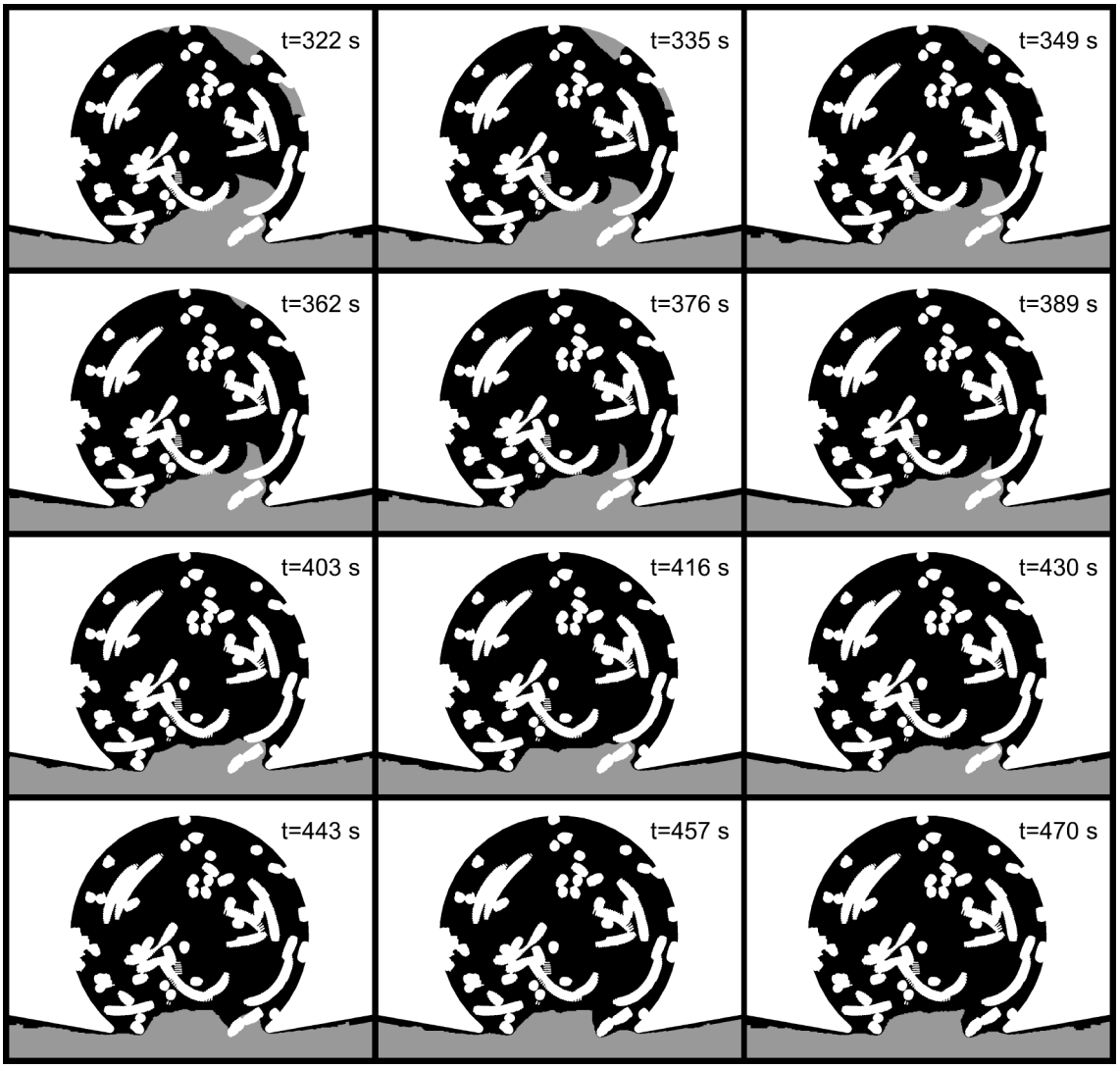

Figure B.7: Continued.

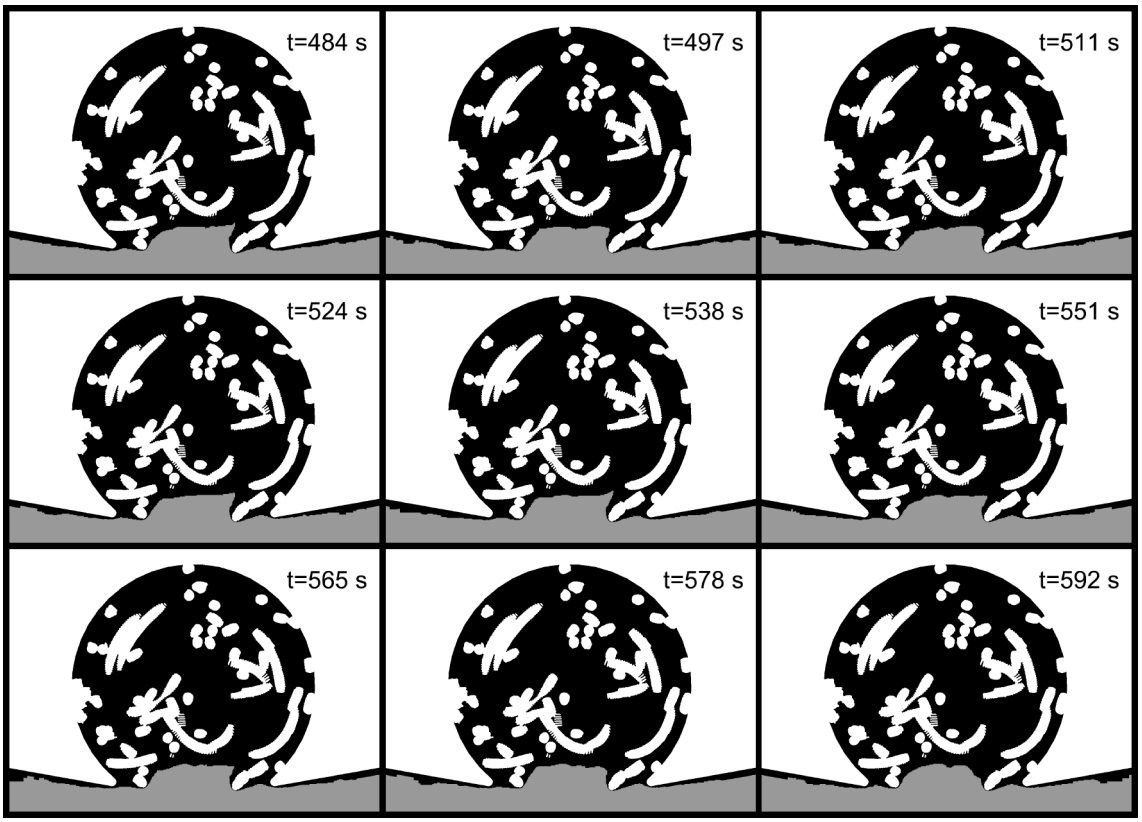

Figure B.7: Continued.

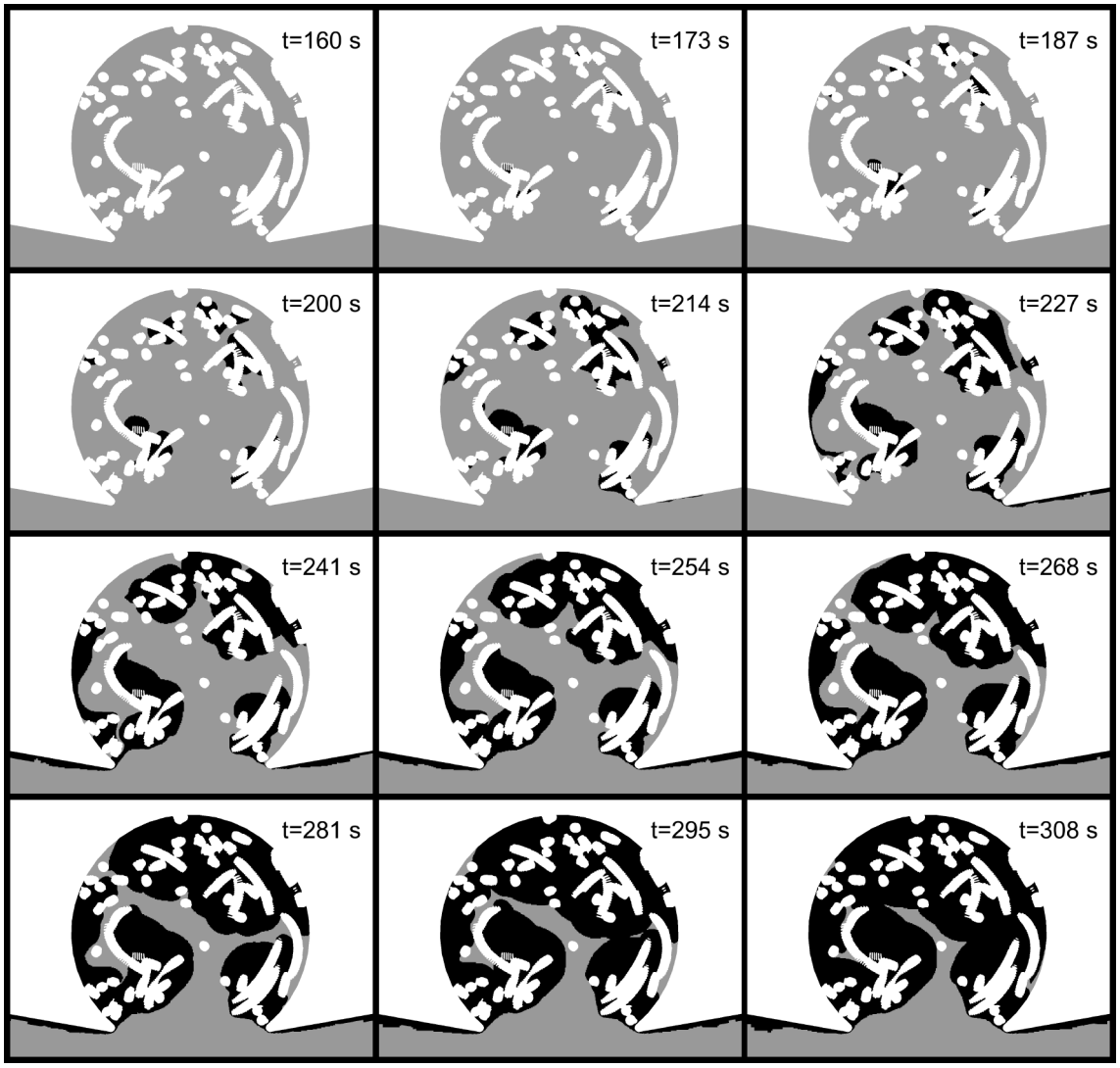

Figure B.8: Clot distribution over time in the coil-filled aneurysm predicted by the medium-fidelity thrombus model. Coil case #2.

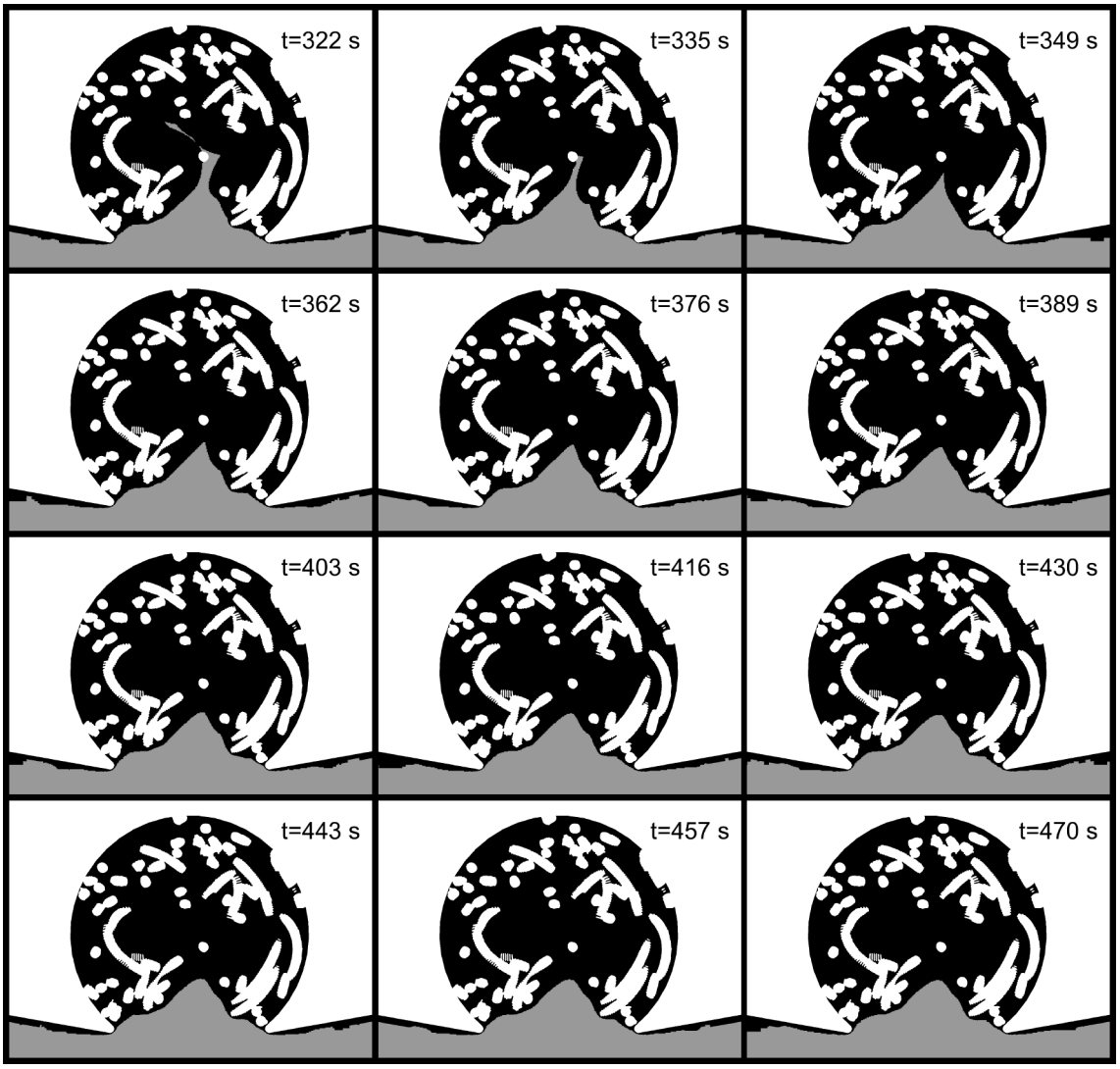

Figure B.8: Continued.

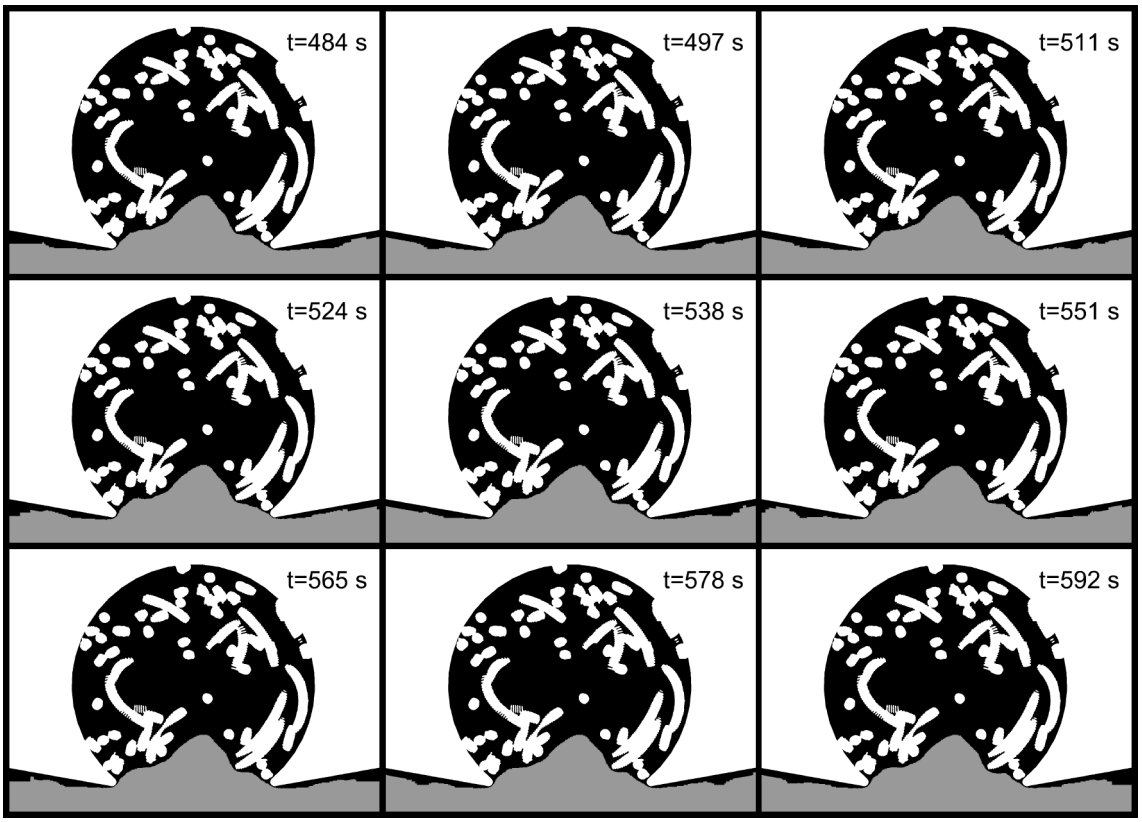

Figure B.8: Continued.

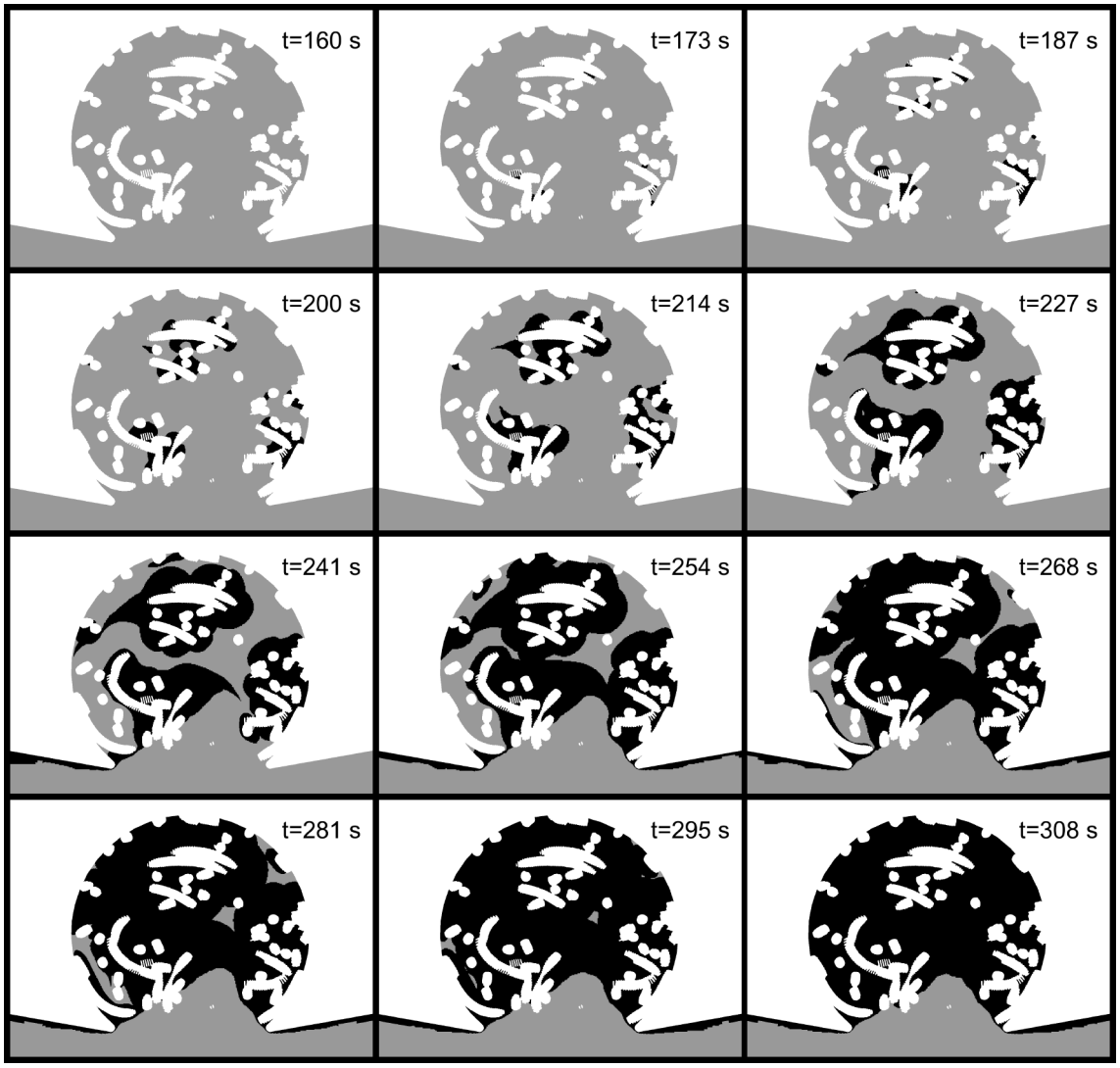

Figure B.9: Clot distribution over time in the coil-filled aneurysm predicted by the medium-fidelity thrombus model. Coil case #3.

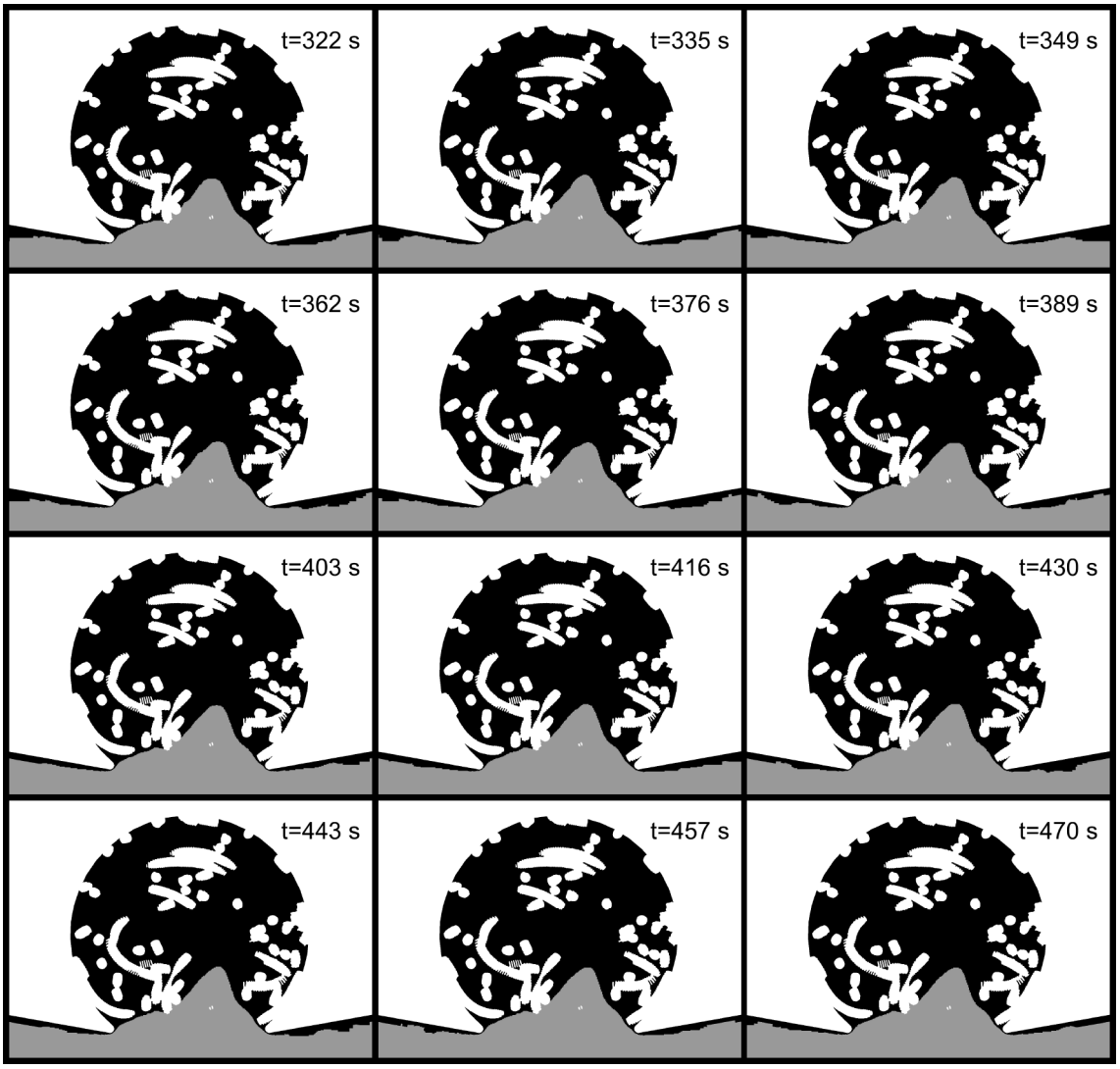

Figure B.9: Continued.

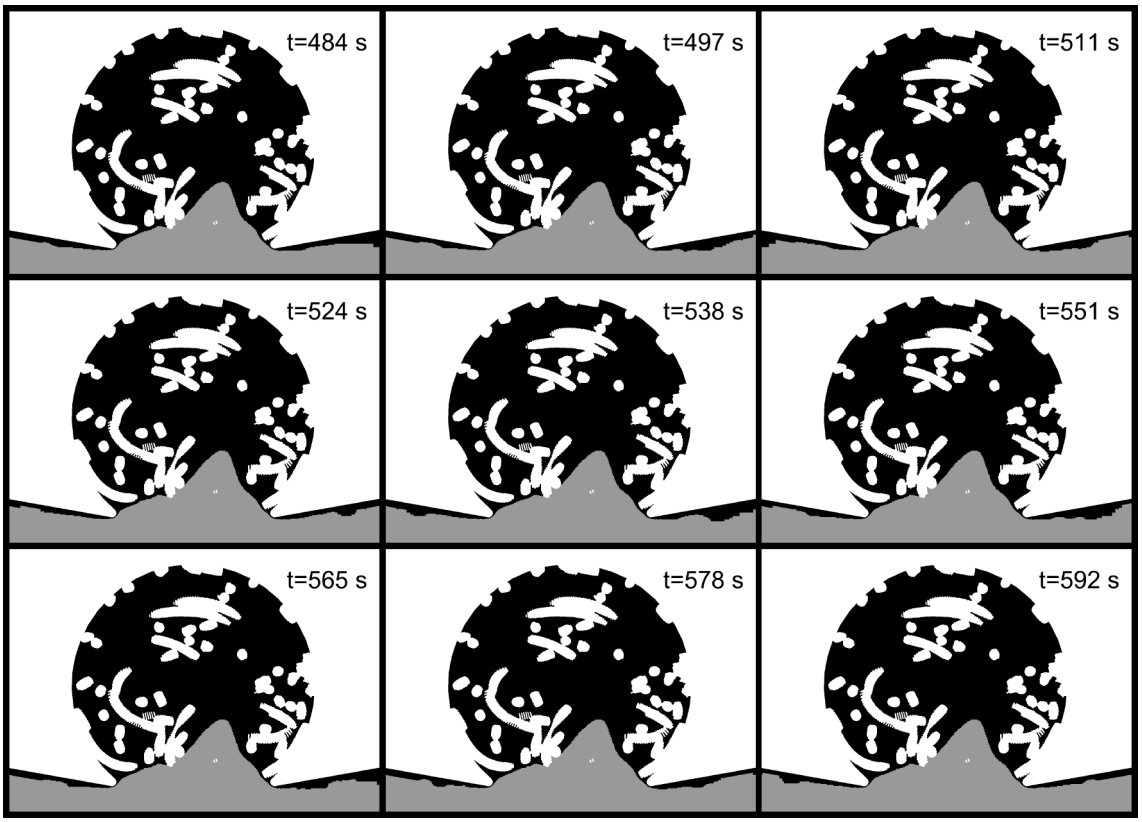

Figure B.9: Continued.

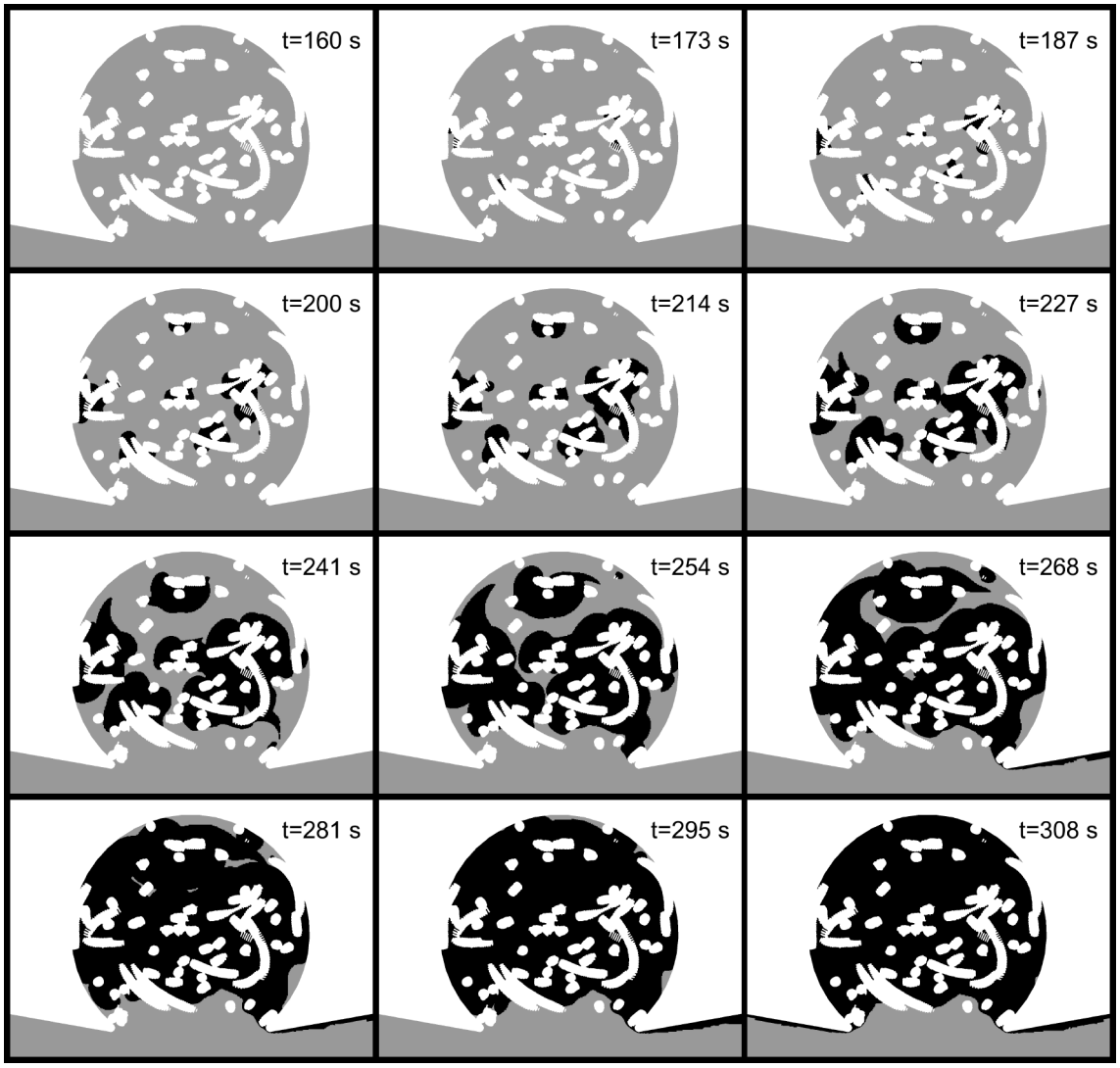

Figure B.10: Clot distribution over time in the coil-filled aneurysm predicted by the medium-fidelity thrombus model. Coil case #4.

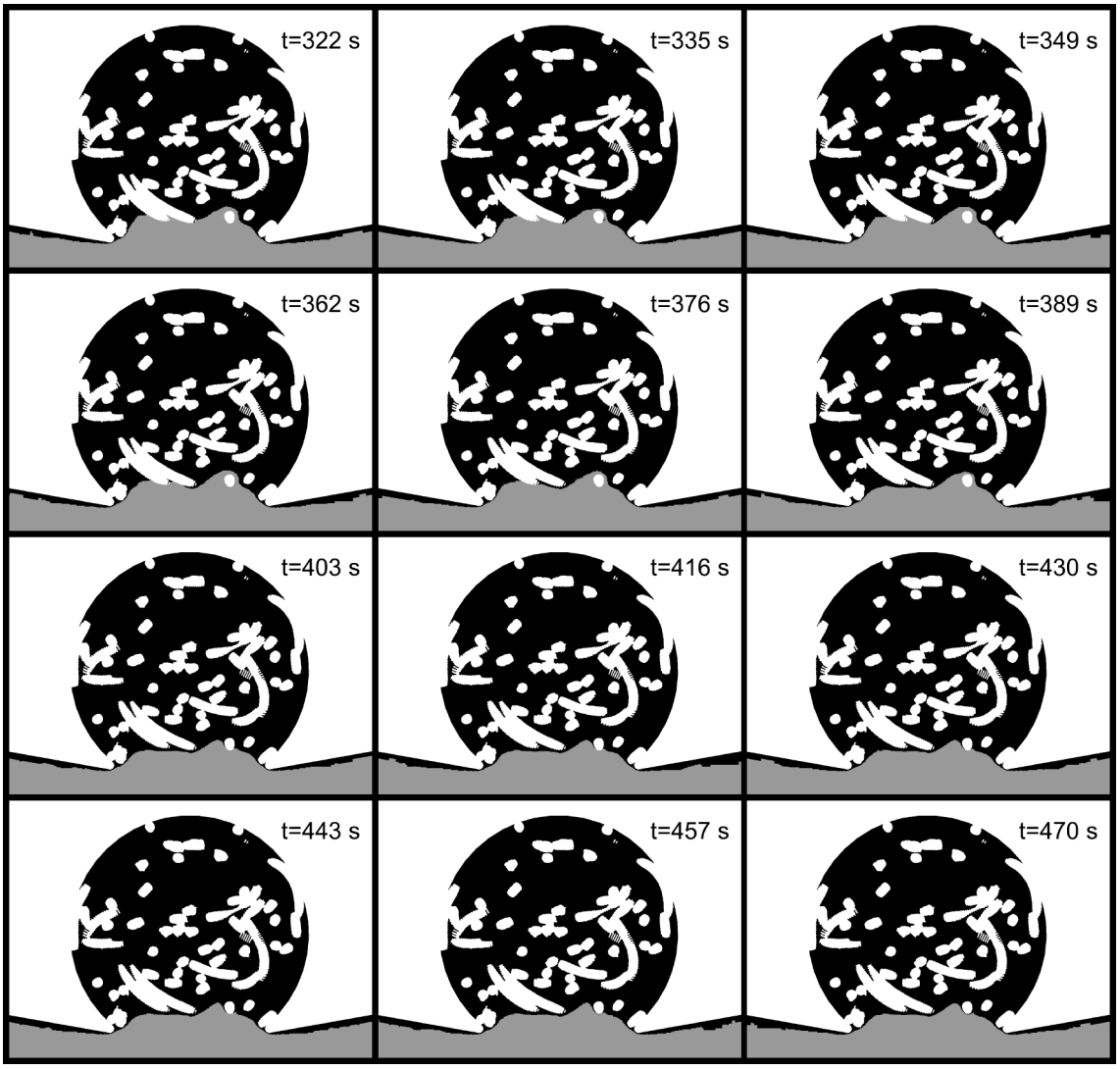

Figure B.10: Continued.

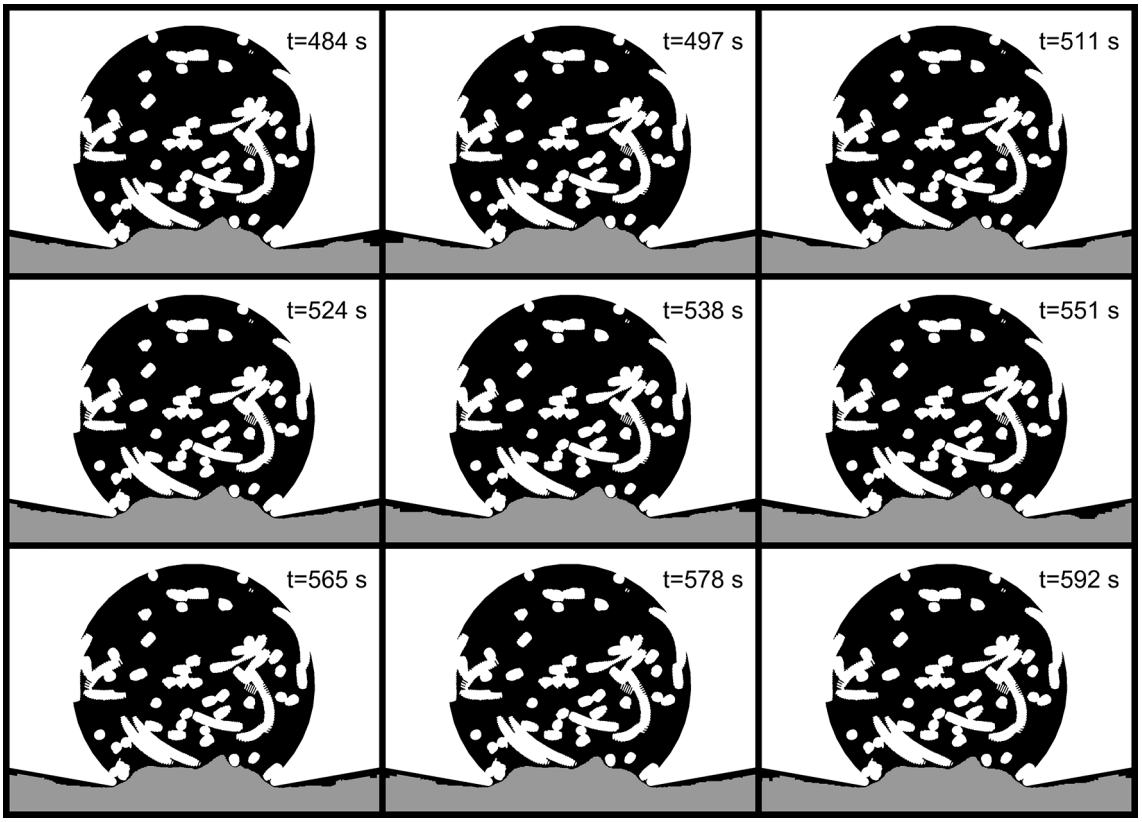

Figure B.10: Continued.

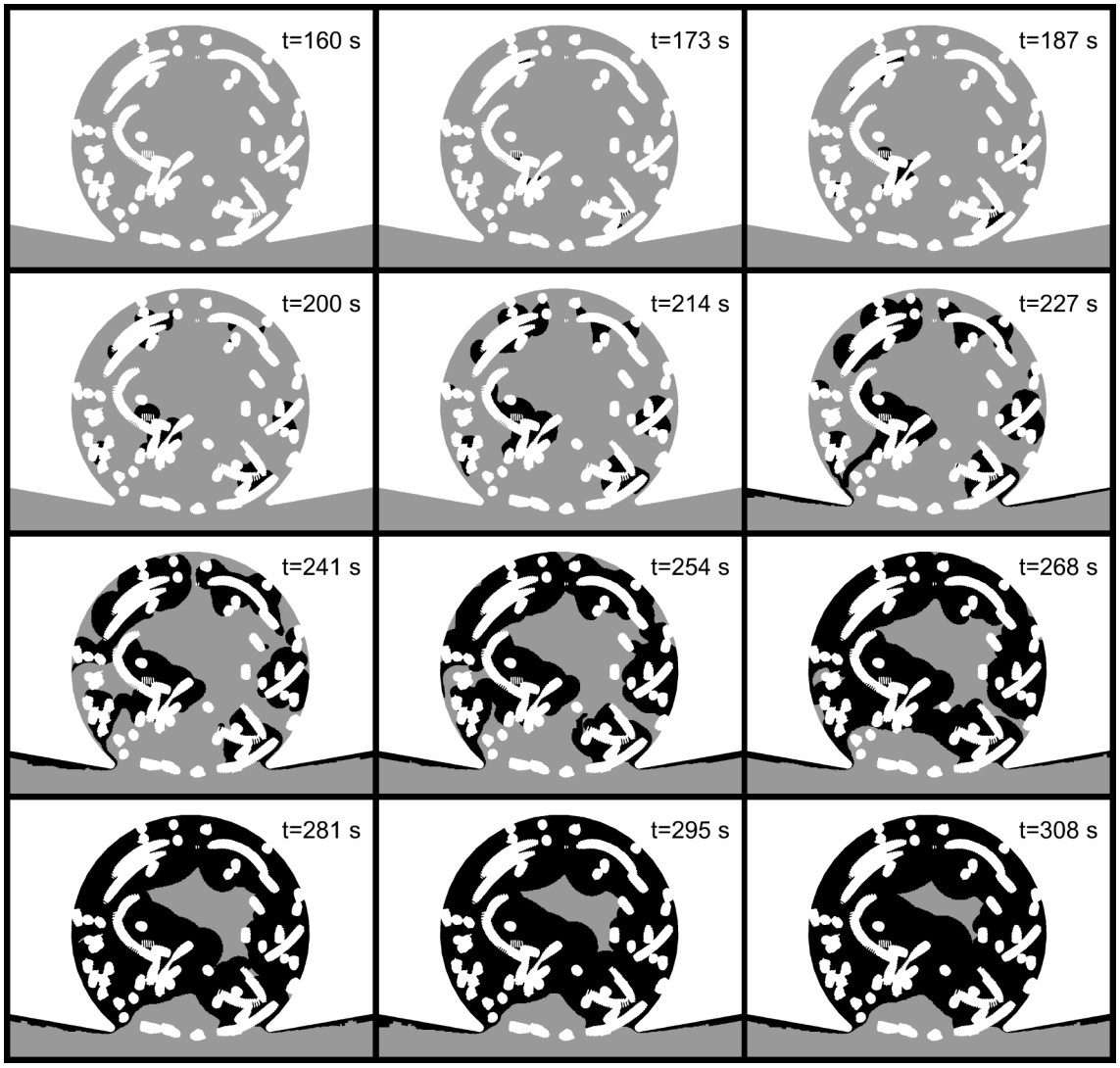

Figure B.11: Clot distribution over time in the coil-filled aneurysm predicted by the medium-fidelity thrombus model. Coil case #5.

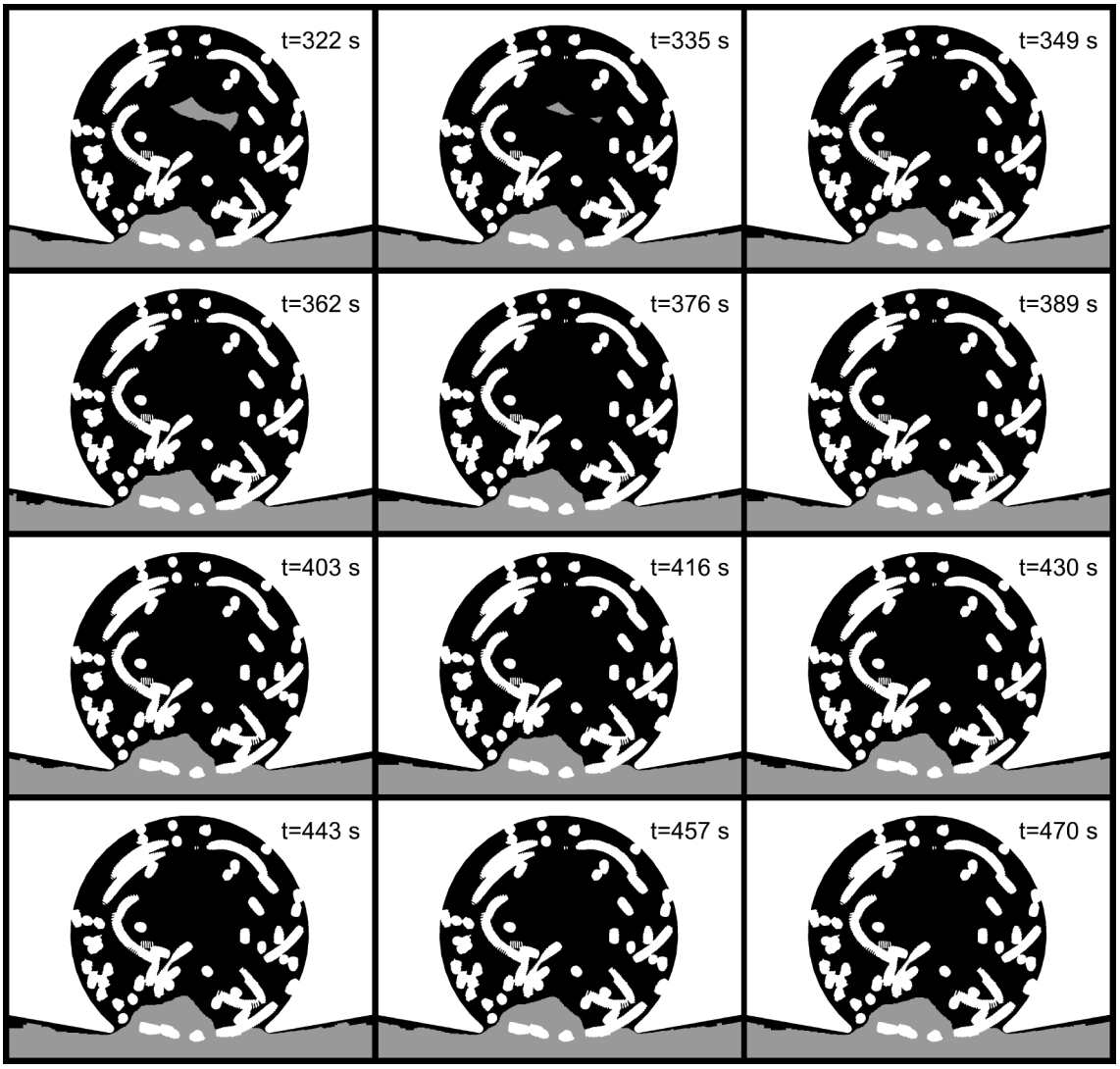

Figure B.11: Continued.

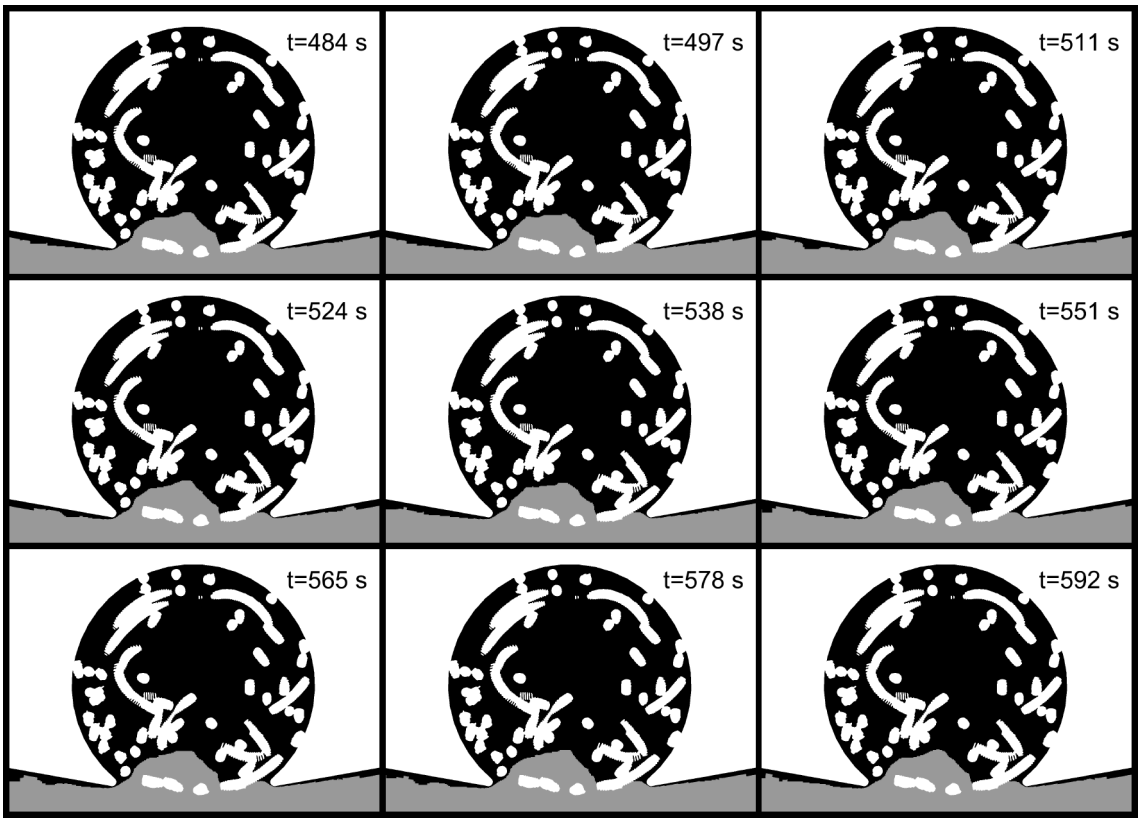

Figure B.11: Continued.

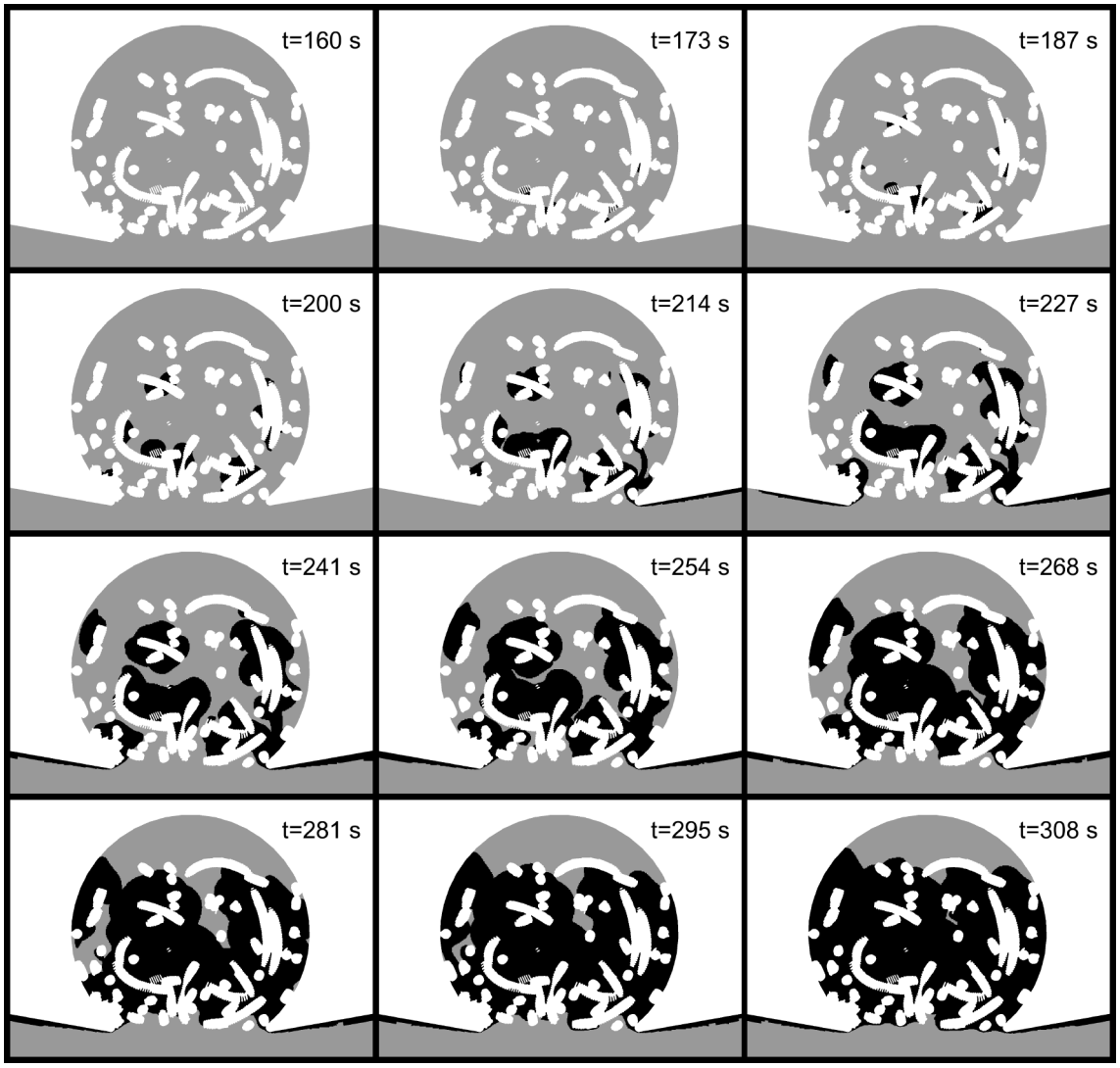

Figure B.12: Clot distribution over time in the coil-filled aneurysm predicted by the medium-fidelity thrombus model. Coil case #6.

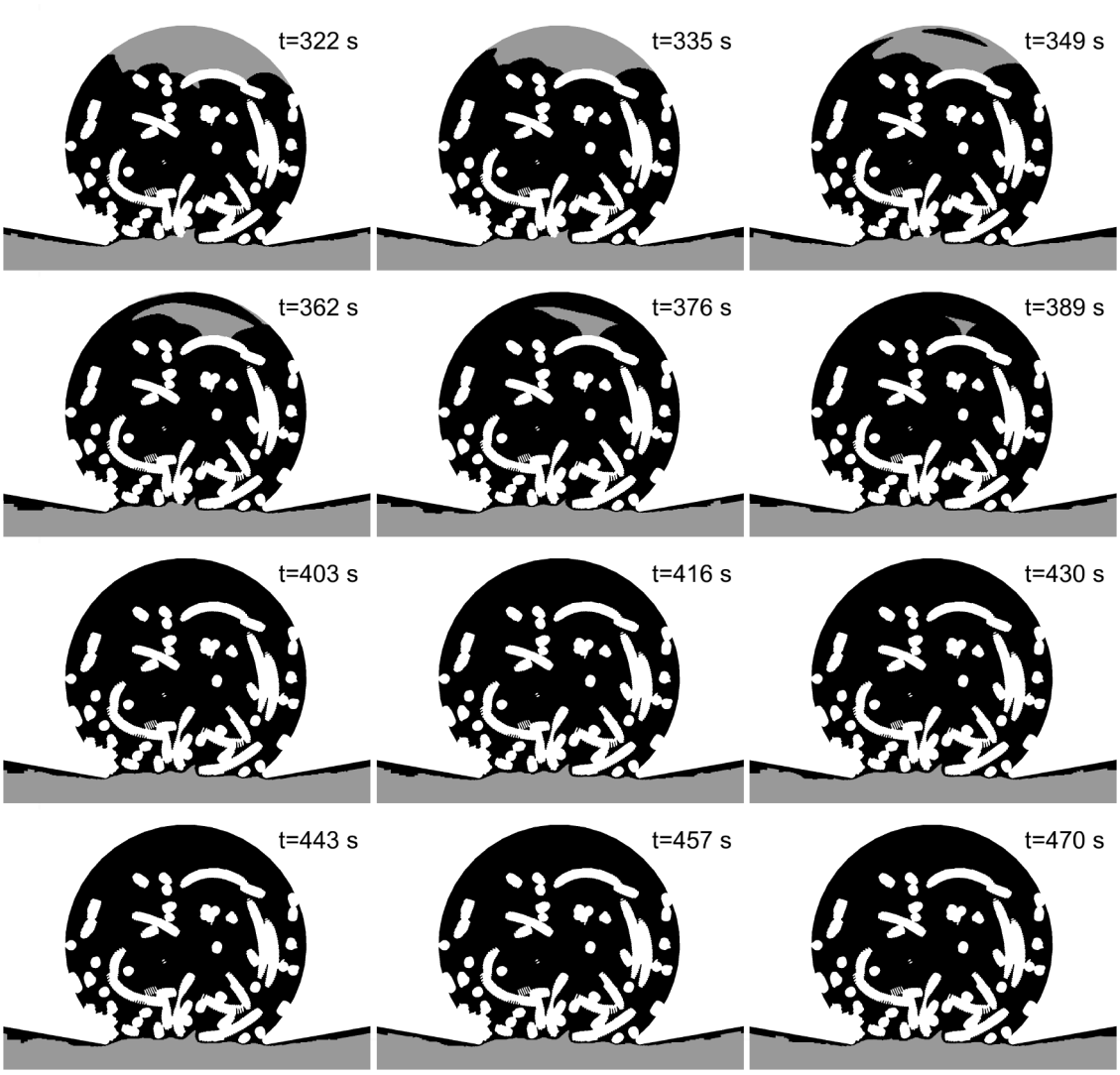

Figure B.12: Continued.

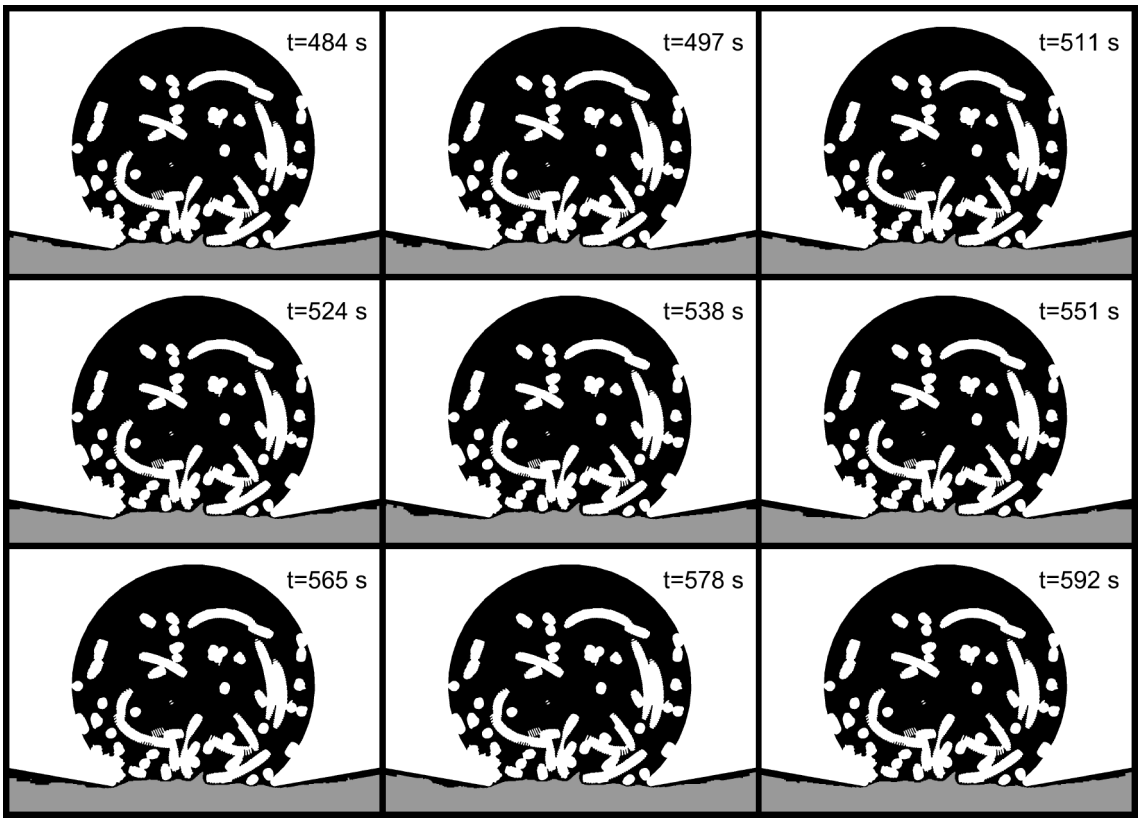

Figure B.12: Continued.